M.Sc. Thesis Technical medicine

Object-oriented navigation using augmented reality: a new way of image-guided surgery!

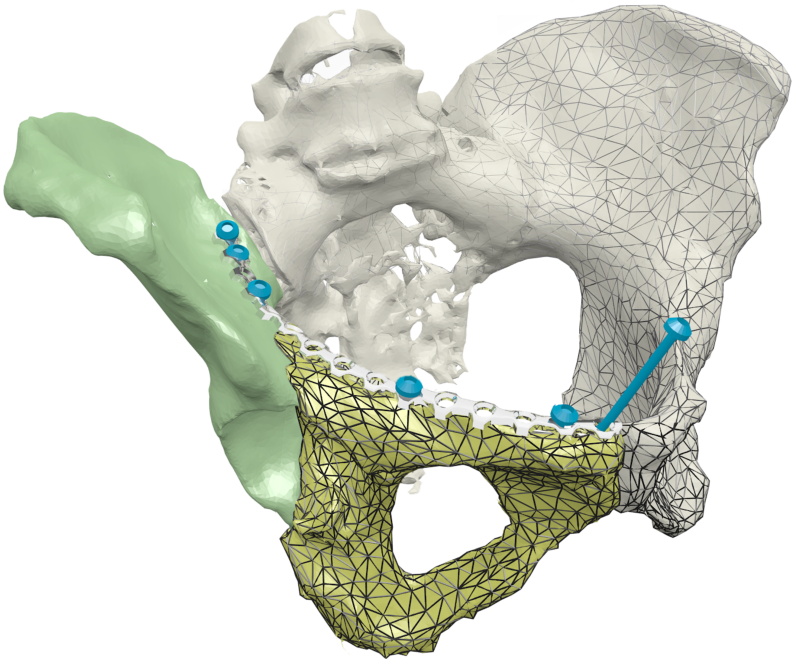

Author:
J. Nijsink

Technical Supervisor UT:	Dr. Ir. F. Van der Heijden
Medical Supervisor UMC:	Dr. J. Biert
Daily medical Supervisor UMC:	Drs. J.H. Peters
Technical Supervisor UMC:	Ir. Ing. L.M. Verhamme
Project Supervisor:	Drs. B.J.C.C. Hessink-Sweep

UNIVERSITY OF TWENTE.

Radboudumc
university medical center

17th August 2017

Foreword

The masters's thesis at hand is my final piece of work delivered as a Technical Medicine student. In this work, I present the study conducted at the 3D Lab and the department of surgery at Radboudumc in Nijmegen. This thesis completes my master's Medical Imaging & Intervention at the University of Twente.

During my internship at Radboudumc, I dived into the world of augmented reality. Combining this novel display modality with the upcoming techniques of image-guided surgery was a very educational journey. At the 3D Lab and the department of surgery, I had the possibility to further enhance my skills as a Technical Medicine professional. I improved my clinical, communication, research and development skills in a pleasant environment. Due to the open atmosphere at the 3D Lab, I was able to explore my talents in different areas besides the studies presented in this thesis. The additional work and projects I have been part of are further elaborated in Appendix A. I hope the delivered work will be continued and may have a direct impact on patient healthcare.

I would like to thank several persons who contributed in different ways to this thesis. First of all, I would like to thank the members of the trauma surgery team. Especially, Jan Biert, my medical supervisor and expert at the treatment of pelvic fractures. Furthermore, I would like to thank Joost Peters and Bas van Wageningen for the pleasant collaboration and medical supervision during the year.

I also thank the members of the 3D Lab. First off, Thomas Maal, head of the department who provided me with the opportunity to join the 3D Lab and made me feel welcome from the start. I also like to thank Luc Verhamme and Jene Meulstee, for supervision and daily support. Besides the substantive discussions, recommendations and advices, there was room for personal conversations making me feel part of the team. Furthermore, I would like the thank other members of the 3D Lab, who were always eager to assist and shared a lot of nice moments.

I would also like to thank Ferdi van der Heijden for the technical support and advices. I also thank Bregje Hessink-Sweep, who greatly fulfilled the difficult job to replace Laurens Veltman as process supervisor. Together with the intervison group, she learned me to look at my personal development in a different way.

Lastly, I would like to thank my parents, brothers, family and especially my girlfriend who have always been there for me. They showed interest, made me feel comfortable and always wanted the best for me. With their support, the past 6 years passed by very quickly. Thanks!

Han Nijsink,

17th August 2017

Abstract

Aim: The aim of this thesis was to develop and evaluate a new method to improve image-guided surgery (IGS) for treatment of complex pelvic fractures. Using IGS, minimal invasive treatment is possible and can improve patient outcome. However, conventional IGS can not treat unstable displaced fractures. Therefore, a system was developed that enabled tracking of separate objects using an optical tracker and visualized the tracked objects in 3D. This object-oriented navigation (OON) system was optimized by determining an optimal dynamic reference frame (DRF) and by investigating the influence of different conditions on accuracy. Furthermore, the system was combined with the HoloLens to merge objects at the surgical site with th output of the navigation system. The accuracy of the system with and without the implementation of augmented reality (AR) and the performance of the guidance was evaluated under optimal conditions. Furthermore, a possible clinical implementation for pelvic fracture treatment was proposed.

Materials and Methods: A virtual model of an optical tracker was created and used to determine an optimal marker configuration for the DRF by applying a Monte Carlo analysis. Using the most optimal DRF, the performance of the PST Base optical tracker was tested in different conditions by comparing it to reference coordinates of an accurate milling machine.

The accuracy of the OON system was evaluated by bringing 3D objects to pre-planned positions and calculating the deviation from the planned position using the OON system with and without AR. By placing objects at planned positions displayed by the OON system and calculating the deviation, the usability of the guidance in both settings was evaluated.

Results: Simulations showed that the configuration of the markers in a DRF influences the performance of the optical tracker. Performance increased with decreasing linearity, increasing amount of markers and increasing distance between markers.

The error introduced by the tracker was largest in the direction away from the tracker (mean error = 5.3 mm) and was influenced by warming up of the tracker and different filter settings.

The mean deviation of the OON system with and without the use of AR was 0.60 mm (sd = 0.16) and 0.71 mm (sd = 0.24), respectively. Object placement using the OON system as guidance showed mean deviations of 0.70 mm (sd = 0.44) and 1.81 mm (sd = 0.68), respectively.

Conclusion: Different aspects influencing the performance of an optical tracker were evaluated and must be considered when implemented in clinical practice. The developed OON system performed with an accuracy that meets the clinical relevant accuracy of 2 mm in an optimal situation. Using the guidance of the system, objects can be placed according to the planning. Combining OON with AR reduced the accuracy of the guidance and should be improved.

Contents

List of Figures

List of Tables

List of Abbreviations

HET ..... High energy trauma
3D ..... Three-dimensional
(CB)CT ..... (Cone-beam) computed tomography
OR ..... Operation room
2D ..... Two-dimensional
OON ..... Object-oriented navigation
EM ..... Electromagnetic
IR ..... Infrared
DRF ..... Dynamic reference frame
AR ..... Augmented reality
MR ..... Mixed reality
IGS ..... Image-guided surgery
HMD ..... Head-mounted display
RMS ..... Root mean square
FLE ..... Fiducial localization error
FRE ..... Fiducial registration error
TRE ..... Target registration error
MCA ..... Monte Carlo analysis
MMSE ..... Minimum mean square estimator
WCS ..... World coordinate system
API ..... Application programming interface
LTA ..... Linear testing apparatus
CMM ..... Coordinate measurement machine
FOV ..... Field of view
SD ..... Standard deviation
UCS ..... Unity coordinate system
HRP ..... HoloLens Remoting Player
ICP ..... Iterative closest point

Chapter 1

General introduction

The pelvic ring is formed by the sacrum and the left and right coxal bone (Figure 1.1a). Until puberty, the coxal bones are made up of three bones, the iliac, ischial and pubic bone, separated by hyaline cartilage [1]. During aging, the three separate bones fuse and ossify to form one large coxal bone (Figure 1.1b) [2]. Anteriorly, both coxal bones are linked with the cartilage of the pubic symphysis [3]. Posteriorly, the sacrum is connected to both coxal bones by several strong ligaments [4, 5].

The pelvic ring is a rigid, low deformable and mechanically strong structure [6]. The specific anatomy makes it possible to fulfill its main goal; transferring the weight of the trunk via the acetabula to both lower extremities. It is shaped to withstand omnidirectional forces and the structure is capable of weight-bearing and child bearing [6]. Furthermore, it contains and protects the pelvic organs and provides muscle attachments [2].

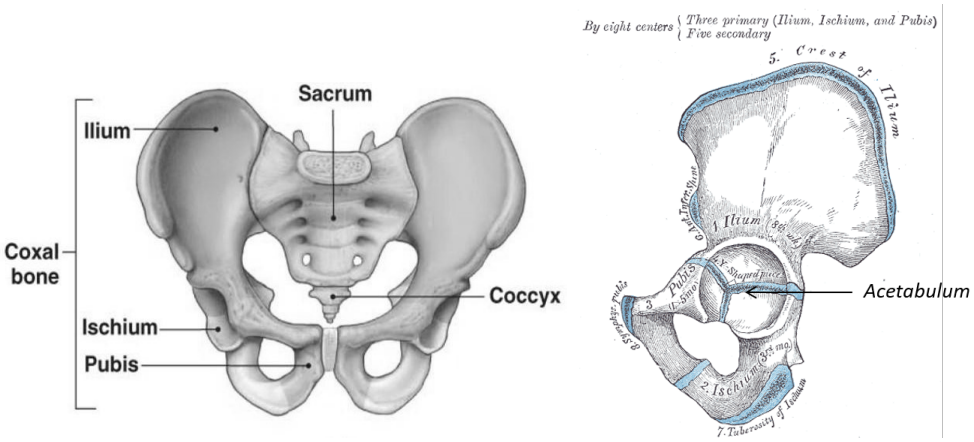

(a) (b)

Figure 1.1: Anatomy of the pelvic bones a) Bones making up the pelvic ring. In the adult situation, the ring is formed by the sacrum and coxal bones. b) The three separate bones of the coxal bone (os ilium, os ischium and os pubis), as seen in children. The cartilage ossifies during aging to form one coxal bone [1].

1.1 Pelvic fractures

Fractures of the pelvic complex disrupts the integrity of the mechanical properties of the ring. Pelvic ring fractures are seen in 3 - 10% of all trauma patients [7–9].

Approximately 50% of these fractures are caused by high energy trauma (HET) [10]. In these situations, catastrophic hemorrhage and death are often reported [9–11]. In elderly patients, even low energy trauma can induce pelvic fractures [12]. Due to the demographic change in age, more pelvic fractures are expected in the elderly in the near future [13].

The Young-Burgess classification is a commonly used classification method to determine fracture type and corresponding trauma mechanism in pelvic ring fractures (Figure 1.2) [14]. Other fractures in the pelvic area are sacral and acetabular fractures. Pelvic and acetabular fractures are relatively rare, preoperative diagnostics and surgical planning are complex and the actual surgery requires highly skilled specialists [7, 15].

Active treatment, however, is desired as research showed that an active surgical approach in pelvic fractures resulted in better functional outcomes compared to a conservative approach [11, 16]. The main goal of surgery is achieving an optimal reposition and stabilization of the displaced fragments. Fixation of the pelvic ring reduces the residual deformation between fractured fragments, relieves pain and improves functional outcome [8, 17, 18]. Furthermore, surgery is intended to prevent early total hip implantation [19]. Surgery in elderly or traumatic patients is often limited or postponed due to the severity of the trauma or the age of the patient [20].

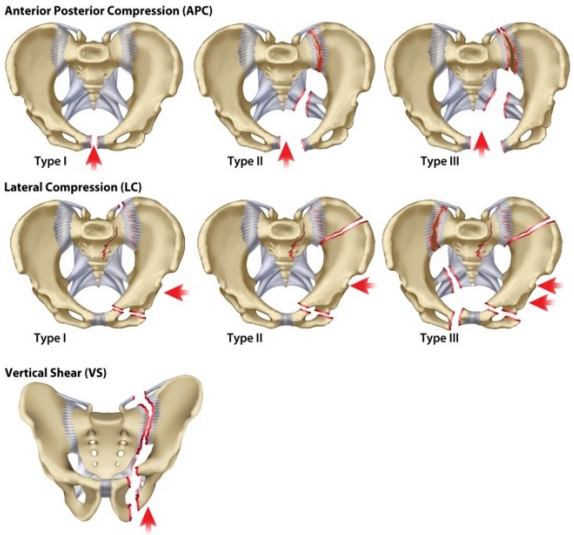

Figure 1.2: Pelvic ring fractures classification according to Young-Burgess [14].

1.2 Treatment of pelvic fractures

Currently, unstable pelvic fractures can be fixated in three different ways;

1. *External fixation* is often used to stabilize the patient in the acute situation, mainly to reduce the hemorrhage. External fixation showed a lower quality of reduction and larger malunion rates compared to internal fixation (Figure 1.3a) [18].

2. *Open reduction and internal fixation* is routinely applied after a few days of recovery in HET patients, reducing the risks for disturbing the pelvic hematoma or inducing new hemorrhage [21, 22]. The fixation is realized using reconstruction plates, spring plates and positioning screws (Figure 1.3b) [23].

3. *Closed reduction and internal fixation* is gaining popularity, since it reduces soft tissue damage and blood loss, and enables early intervention (Figure 1.3c) [20, 22, 24]. To minimize the incision length, a submuscular sliding plate technique has been proposed. This technique demands two small incisions to place the reconstruction plate under the soft structures [23]. In other situations, fixation screws alone are sufficient to reinforce the pelvic ring and facilitate callus formation and bone repair. Gary et al. reported an adequate reduction of acetabular fractures in the elderly with a minimal invasive approach [19].

The quality of reduction of acetabular fractures is often classified using the classification described by Matta [25]. An anatomic reduction is achieved when displacement is within 1 mm. A displacement in the range of 1-3 mm is considered satisfactory. Larger displacements are classified as unsatisfactory. For pelvic ring fractures, the Lindahl classification for displacement is often used with grades; excellent (0 - 5 mm), good (6 - 10 mm), fair (11 - 15 mm) and poor, (more than 15 mm) [26, 27].

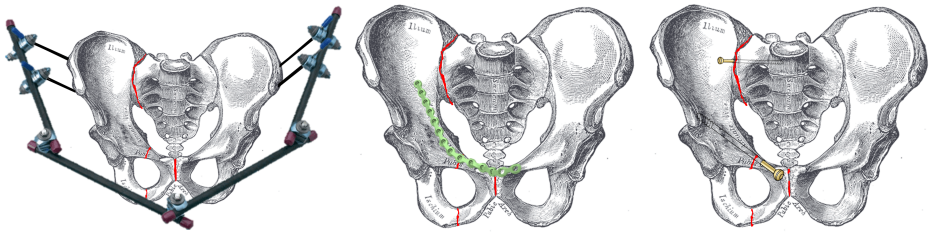

(a) (b) (c)

Figure 1.3: Three approaches for active treatment in pelvic fractures. a) Closed reduction and external fixation using an external fixation device (minimal invasive). b) Open reduction and internal fixation using an osteosynthesis plate and screws (maximal invasive). c) Closed reduction and internal fixation using percutaneous screws (minimal invasive) [1].

1.3 3D Computed Tomography and surgical planning

To improve the treatment of complex pelvic fractures, three-dimensional (3D) technology became important in preoperative decision making [28]. 3D imaging complements the conventional pelvic radiographs (Figure 1.4a). With the introduction of the computed tomography (CT) scan, detailed information of the volume of interest became available for improving the diagnosis of subtle abnormalities and surgical planning (Figure 1.4b-d) [29–31]. Specialists advocate 3D images for surgical planning as it supports in determining the surgical approach, plate positioning and screw trajectories beforehand [29, 32, 33]. 3D reconstructions of CT scans give insight in the extent and severeness of the pathological situation (Figure 1.5a). Currently, 3D printing of the pelvis is gaining popularity in healthcare [34]. It can aid the specialist in determining the surgical approach, prebending of osteosynthesis plates and informing patients [34].

(a) Conventional anteroposterior (AP) pelvic radiograph

(b) Axial cross-section of a CT scan

(c) Coronal cross-section of a CT scan

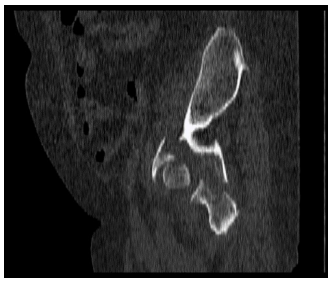

(d) Sagittal cross-section of a CT scan

Figure 1.4: Commonly used image modalities in pelvic fractures in a patient with combined pelvic ring and acetabular fracture. The CT scan provides additional information compared to the pelvic radiographs and is used for 3D reconstructions (Figure 1.5).

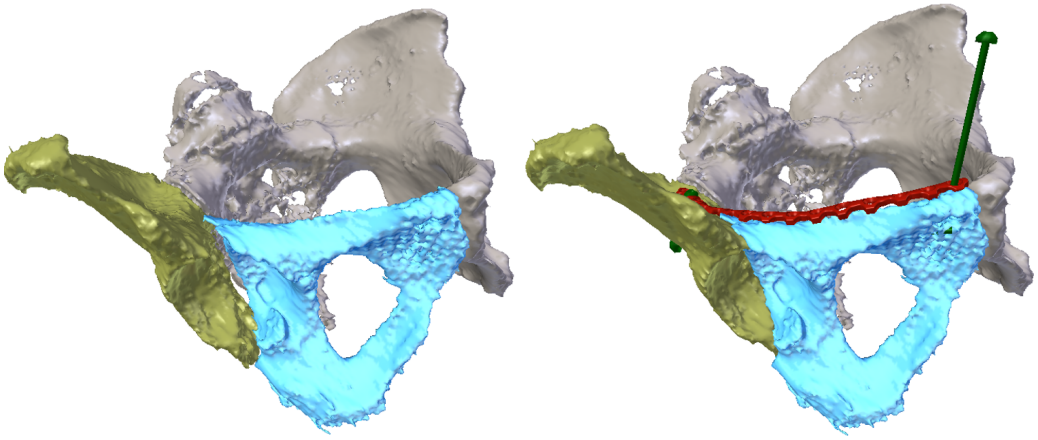

(a) (b)

Figure 1.5: a) 3D reconstruction of the pelvic ring using the diagnostic CT scan. Displacement is present at the left sacroiliac joint and in the acetabulum. b) The surgical plan after virtual reduction was realized. The plate is positioned over the fracture and screws are planned with the correct length and direction.

1.3.1 Prebending of osteosynthesis plates

Several studies have shown the advantages of using 3D prints of patient-specific anatomy as a guide to bend the fixation plates preoperatively (Figure 1.6) [34–38]. First, the view is not impaired by soft tissue which makes it easier to derive the desired shape. Second, the use of precontoured plates reduces operation time and blood loss [35]. Lastly, the plates have to be inserted into the wound only once, reducing the risk of infection and iatrogenic damage [34].

Different techniques for the creation of bending templates are available. First, the anatomy of the pathological side can serve as template in nondisplaced fractures since no reduction is required [34]. Second, the contralateral, nonimpaired side can be mirrored to imitate the prepathological situation of the ipsilateral side [36, 39]. Lastly, fractured fragments can be virtually repositioned such that they mimic the normal anatomy. These techniques are also applied in the virtual reduction of fractures to obtain a surgical plan.

1.3.2 Virtual reduction

In the past years, virtual 3D models of pelvic fractures are used to preplan the surgery by means of virtual reduction (Figure 1.5b). Several methods to preoperatively plan the reduction have been proposed, relying on the above mentioned techniques [15, 40–42]. It enables the specialist to practice the surgical procedure without time pressure, making it possible to adjust the surgical plan according to his demands [36].

Virtual fracture reduction improves the specialists' surgical preparation and 3D perception of the fracture before actually advancing the fracture. This is a major advantage in pelvic fractures, since they are complex and vary from patient to patient [36]. It can even result in reduced surgery time and improved patient outcome [34]. Furthermore, osteosynthesis plates can be digitally designed using patient-specific anatomy and length. Also, entry position, direction and number of fixation screws can be determined. A helpful tool in the virtual reduction is the haptic feedback device, which enables users to interact with the virtual fracture fragments in a more natural way [15].

1.4 Object-oriented navigation

However, until now no method that adequately translates the virtual reduction to the patient in the operation room (OR) is available. Furthermore, the only method to assess fracture reduction and screw position intraoperatively is the use of fluoroscopic imaging [43]. This method, however, is time-consuming and suboptimal since the complex anatomy of the pelvic ring is difficult to assess on two-dimensional (2D) fluoroscopic images [36].

A potential solution for this problem is object-oriented navigation (OON). OON makes it possible to track the location and orientation of 3D models of separate anatomical structures [44]. Using real-time information about the spatial relation of the separate fragments, reconstructed 3D models of the physical fragments are displayed on the monitor. In this way, the relation of the fragments with respect to each other can be monitored, making it easier to reposition fragments according to a preoperative surgical plan. The difference with conventional surgical navigation is

Figure 1.6: 3D print of the mirrored partial contralateral hemipelvis with the prebended plate. The plate is contoured along the pubic bone and iliopectineal line.

the transition from the 2D cross-sectional images of a CT scan to the 3D visualization of the fractured bones.

The main advantage of OON is the possibility to minimize the impact of the surgical intervention to the patient. Especially in displaced, unstable fractures, this technique can replace the maximal invasive open reduction and internal fixation procedure. The translation of the preoperative virtual plan to the patient is presumably having a positive impact on the outcome after surgery [45].

For the development of an OON system, the tracking methods of conventional surgical navigation can be used. Conventional navigation is mainly realized by using optical or electromagnetic (EM) tracking systems. The main advantage of optical navigation is its high accuracy compared to EM systems [46]. Therefore, optical tracking systems are widely used in clinical applications [47]. The line-of-sight requirement, however, is a limiting factor in the clinical setting [46]. This problem is not seen in EM tracking systems [46]. These systems are, however, susceptible to distortion of metal sources. EM systems with passive markers can be profitable in minimal invasive surgery, but are currently not widely available. Furthermore, the performance of those systems should be further investigated before application in OON is possible [48, 49].

Because of the higher accuracy, optical trackers are the preferred choice in OON systems. Optical trackers use infrared (IR) light to detect retroreflective markers. When IR light illuminates the markers, the light is reflected and the cameras in the optical tracker detect the markers. Using stereo vision, the device combines information of both cameras to calculate the position of the markers in the 3D space in an accurate way [50].

1.5 Accuracy of navigation systems

The accuracy of a navigation system is an important parameter in conventional, but also in object-oriented navigation. Accuracy of a system is often described by a

combination of precision and trueness (Figure 1.7). Whereas trueness is often defined as the mean difference between a measured and a reference position after many experiments, precision is the standard deviation (sd) within these experiments [51]. In pelvic fracture treatment, an accuracy of less than 2 mm is required [25–27, 40].

Overall accuracy of a navigation system is dependent on all steps in the workflow, and small errors at the start of the navigation chain can result into large clinical relevant positioning errors. Therefore, it is important to consider the sources of error in developing and using navigation systems.

For systems using optical trackers, several errors influence the performance (Table 1.1). First, the error introduced by the hard- and software and the calibration of the optical tracker will directly influence the accuracy [52]. Second, errors come along with the registration between patient and image data. This error varies with the available registrations methods [53, 54]. Correlations between accuracy, slice thickness and voxel size are well known [55–63]. Third, in fiducial-based registration, markers fixed on a patient must be detected by the navigation system as well as in the image data resulting in additional errors [64, 65]. Fourth, to realize registration, markers can be mounted on the patient using a frame, the dynamic reference frame (DRF). The marker configuration defined by the DRF is said to influence the overall accuracy, which makes the design of a good performing DRF important [60, 62, 66].

Table 1.1: Error sources in surgical navigation and expected magnitude of the error, propagation effect and importance for the accuracy in the application.

Type of error	Magnitude	Propagation effect	Importance
Optical tracker errors			
Tracker hardware, lenses and design	++	++	+++
Warming up of tracker [59]	+	- -	-
Camera calibration	- -	++	+
Marker detection	- -	+	-
Object detection / registration [61]	-	+	+
Motion filtering	++	+	++
Image acquisition & processing			
Quality / resolution of scan [58]	+	-	+
Patient motion during scanning [59]	+	+	+
Marker detection	-	+	+
Other errors			
Registration of patient and scan [59, 61]	+	++	++
Distance between DRF and target [62]	++	+	++
Distance between tracker and DRF [63]	+	+	+
Human interpretation errors [59]	+	-	+
DRF design, fixation and stability	++	+	++
Passive vs. active markers [63]	-	+	+
Spherical vs. circular markers	-	+	+

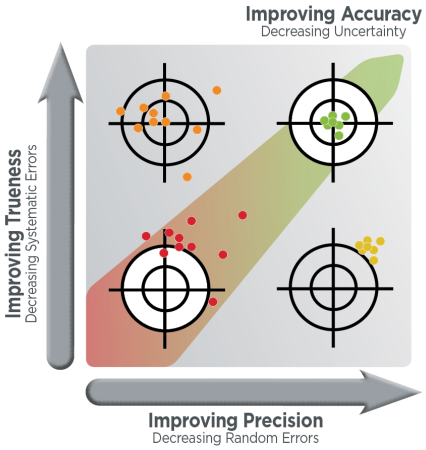

Figure 1.7: Accuracy defined by precision and trueness. Both high trueness and high precision are necessary to achieve high accuracy.

1.6 Augmented reality

Augmented reality (AR) is an upcoming technology used to improve visualization of 3D objects by means of holograms. The technique makes it possible to merge virtual objects with objects in the real world, creating a mixed reality (MR) setting (Figure 1.8). In the recent years, extensive research on the implementation of AR in the medical field has been performed. Examples are: evaluation of patient-specific pathology, pain relief, anatomical education and telemedicine [67–70]. The combination of AR with image-guided surgery (IGS) has a large potential [71–74].

The main reason for the request of AR in surgical navigation is that until recently, information from the navigation system was projected on a monitor [75–77]. This obliged the specialist to keep eyes on both the surgical field and the computer display, impeding the continuity of surgery [78]. With the implementation of AR in surgical navigation, 3D models of the patient-specific (tracked) structures can be merged with the surgical scene. This feature enables the specialist to keep focus on the surgical field. Several studies investigated the use of augmented reality in combination with surgical navigation using a head-mounted display (HMD), with positive feedback of users and promising results on surgical accuracy [78–82].

The Microsoft HoloLens (Microsoft, Redmond, US) (Figure 1.9b) is one of the first stand-alone optical see-through HMDs. The device is able to render high quality holographic 3D models and has the potential to generate a realistic mixed reality setting. Using voice commands and gestures, the user is able to interact with the device. This makes it possible to control the device in a sterile manner. 3D reconstructions of patient-specific anatomy can be uploaded and visualized in 3D [83,84]. The HoloLens, in combination with a tracking system can be used to develop an OON environment in an AR setting.

1.7 Situation at Radboudumc

The aim of Radboudumc is to have a significant impact on healthcare. At the department of traumatology, a close collaboration is established with the 3D lab. At this expertise center, 3D techniques are implemented in several clinical departments, improving diagnosis and creating surgical plans using surgical guides or surgical

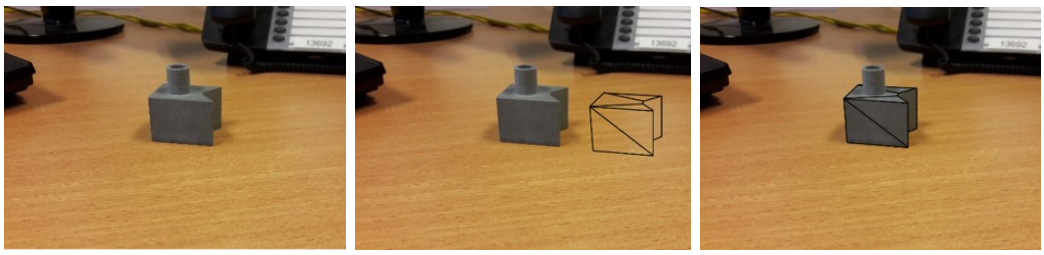

(a) (b) (c)

Figure 1.8: Enhancement of reality. a) Reality: A real world object. b) Augmented reality: A real world object with a virtual object projected alongside. c) Mixed reality: A virtual object is projected over the world object.

navigation. Members of the department work on the latest technologies to improve and simplify healthcare.

One aim of the 3D lab is developing an object-oriented navigation system for different applications in amongst others traumatology, orthopedics and maxillofacial surgery. The tracker used for OON is the PST Base system (PS-Tech, Amsterdam, Netherlands) (Figure 1.9a). In this thesis, this device will be denoted as tracker or optical tracker. The manufacturer of this infrared-based optical dual camera tracker states that the system has a root mean square (RMS) error of < 0.5 mm within 2.5 meters from the tracker. This accuracy is likely to satisfy the clinical demands. Furthermore, the output data is accessible, making it possible for using it in application development.

The Microsoft HoloLens is available for integration with the OON software. These two devices will form the basis to achieve the ultimate goal; projection of patient-specific anatomical 3D holograms on the patient as guidance for the specialists to achieve results comparative to the preoperative surgical plan.

(a) (b)

Figure 1.9: Hardware used for OON in an augmented reality setting. a) The PST base, an optical navigation system. b) Microsoft HoloLens, a standalone HMD used to project virtual 3D models on real objects.

1.8 Aim and objectives

With the translation of the surgical plan to the patient using OON, improvement of surgical results is expected as it minimizes the surgical impact and reduces hospital stay. Trauma patients with pelvic fractures and comorbidity is a patient group that will highly benefit from a transition of maximal invasive open surgery to minimal invasive interventions [13]. The ultimate goal with the implementation of OON leads to having a significant impact on healthcare.

The aim of this thesis is to develop a basic functional implementation for object-oriented navigation and to use it in combination with augmented reality. The performance of the developed system is investigated and a proposed clinical workflow for pelvic fracture repair is discussed. In the present thesis, the main question to be answered is:

What is the performance of the object-oriented surgical navigation system using an optical tracker?

The main question will be answered by the use of four sub-questions. First off, the influence of the marker configuration in a DRF on the performance of the optical tracker will be assessed. A Monte Carlo analysis is performed to find an optimal marker configuration. This research is conducted to answer the first sub-question:
(i) What is the optimal marker configuration for object-tracking using the optical tracker?

Using the found optimal DRF configuration, the performance of the tracker in different conditions is tested. The distance from DRF to tracker, different filter settings and tracker warming-up time (italic elements in Table 1.1) are evaluated to answer the second sub-question:
(ii) What is the influence of different conditions on the accuracy of the tracker?

A system for object-oriented navigation is developed and its performance is tested by placing objects at preplanned positions. Differences between the planned and measured position of the objects are used to evaluate the accuracy. This study is conducted to answer the third sub-question:
(iii) What is the accuracy of object-oriented navigation?

Linking the OON system with the HoloLens can influence the accuracy of object tracking. Hence, the performance of the system connected to the augmented reality device will be determined. Furthermore, the overlay of virtual and real objects is analyzed in order to answer the fourth sub-question:
(iv) What is the accuracy of object-oriented navigation in an augmented reality setting and what is the error in merging virtual and real objects?

1.9 Thesis layout

In the thesis at hand, the development and performance of an OON system is investigated. In Chapter 2, a method is described to determine the optimal configuration of a dynamic reference frame for the tracker used in the developed OON system (sub-question i). In Chapter 3, the performance of the optical tracker is tested under different conditions to determine the optimal circumstances (sub-question ii). In Chapter 4, the link between optical tracker and the HoloLens is described and the performance is tested (sub-question iii). In Chapter 5, the translation to augmented reality is established and the accuracy is evaluated (sub-question iv). The content of this chapter will be used for writing a scientific article that will be submitted to Natures' Scientific Reports. In Chapter 6, a clinical workflow is described to evaluate whether implementation of OON in clinical practice is technically possible. Conclusions and future prospects are described in the final chapter, Chapter 7.

Chapter 2

Marker configurations and accuracy

In surgical navigation or image-guided surgery (IGS), it is necessary to relate patient data with the navigation system. Patient data might consist of computed tomography (CT) or magnetic resonance images. Both the patient data and the optical tracker have their own coordinate system, the patient coordinate system and the camera coordinate system, respectively. A transformation from one coordinate system to the other, also called registration, is required to enable IGS. Although many registration methods and algorithms are available, the goal is the same: finding an optimal transformation that merges both coordinate systems. The transformation is often calculated by minimizing a cost function describing the error between the location of marker pairs in both coordinate systems [54, 60]. Many different methods for point-based registration exist, varying from placement of fiducial markers on skin, to pointing anatomical landmarks. Bone-anchored dynamic reference frames (DRF) appears to be the most accurate registration method [54, 85, 86].

A DRF makes it possible to mount markers in a specific configuration on the patient. The markers must be detected in the image data and by the optical tracker to enable the registration. During tracking, the position of each individual marker is located by the optical tracker. The recognition of a set of markers in a specific configuration makes it possible to define the position and orientation of this set of markers. The DRF requires at least three locations to place markers, since this is the minimal number to describe the movement of a rigid body with six degrees of freedom [59].

It is reported that the design of the DRF has a relation with the accuracy in optical navigation [60, 66, 87]. West et al. claim that the error for markers in a 2D planar configuration is about 22% to 41% larger than for markers in an optimal 3D configuration [60]. Furthermore, they state that accuracy improves when a DRF has the least linearity.

To evaluate accuracy, Maurer et al. suggested a method describing the accuracy of a navigation system using three different types of errors [54, 62, 88]. These types are:

- **Fiducial localization error (FLE)** is the difference in the located/pointed position of the fiducial and the actual location of the fiducial on the patient. Inaccuracy in detection markers in patient data increases the FLE.

- **Fiducial registration error (FRE)** is the distance between a pair of fiducials after registration.

- **Target registration error (TRE)** is the difference between a pair of targets other than the fiducials.

These errors can be used to define the relationship between number of markers and accuracy. Literature states that accuracy improves when a DRF consists of more markers [54]. Maurer et al. found a relationship between mean TRE, fiducial configuration constant k, FLE and the square root of the number of fiducials N [54]:

$$TRE = 1.64k\frac{FLE}{\sqrt{N}} \tag{2.1}$$

Fitzpatrick et al. and West et al. reported the same $\frac{1}{\sqrt{N}}$ relationship between number of fiducials and accuracy [60,66,87]. It is stated that registration using four fiducials is approximately 15% more accurate than registration using three markers [54]. West et al. report that the number of fiducials in a setting using bone-anchored DRFs is typically three to five [62].

As the configuration influences the performance of the navigation system, the current chapter describes a method to find an optimal marker configuration. The optimal configuration is defined as the the distribution of a certain number of markers yielding the lowest error. As optimal reference frames may differ amongst different type trackers, a simulation was used to find the optimal configuration using the trackers' specific properties. This simulation answered the first sub-question: *What is the optimal marker configuration for object-tracking using the optical tracker?*

2.1 Methods and Materials

A Monte Carlo analysis (MCA) was performed to determine the optimal marker configuration. In a MCA, an artificial world is created, resembling the real world in all relevant aspects. The behavior of this artificial world is evaluated by randomly adjusting one or more variables for several times and assessing the outcome [89].

In the present study, the virtual world was described by a virtual optical tracker tracking randomly designed DRFs. In the analysis, coordinates of markers in different configurations in the 3D space were projected n times on two camera images of a virtual tracker (2D) and noise was added to these 2D coordinates. Next, the coordinates were projected back to 3D using a minimum mean square error (MMSE) estimator [90]. A tooltip position was defined in a repeatable way for every configuration and tooltip positions of marker sets with and without noise were compared. An overview of the method is shown in Figure 2.1 and a detailed explanation follows below.

2.1.1 Virtual model of the optical tracker

A virtual camera model was created in Matlab (Mathworks, Natick, MA, USA), using the stereo camera calibrator application described by Zhang et al. [91]. Twelve images of a checker board with squares of 2 cm were captured by both cameras of the PST base optical tracker and the cameras' calibration parameters were calculated. To create the virtual model of the optical tracker, the intrinsic parameters of camera 1 and 2 were used in the form of calibration matrices, ${}^{1}\mathbf{K}$ and ${}^{2}\mathbf{K}$. In the MCA, the world coordinate system (WCS) was assumed to be equal to the first cameras' coordinate system (C_1CS). This results in a rotation matrix, ${}^{1}\mathbf{R}_{WCS} = \mathbf{I}_3$ and a

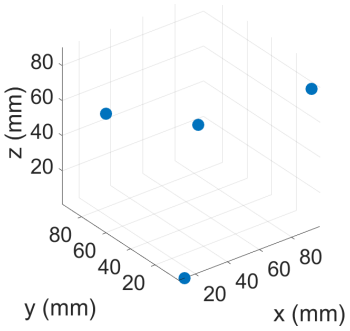

(a) Initial marker configuration in the 3D space. For every marker configuration in the MCA, markers were randomly placed in a box of 100 x 100 x 100 mm.

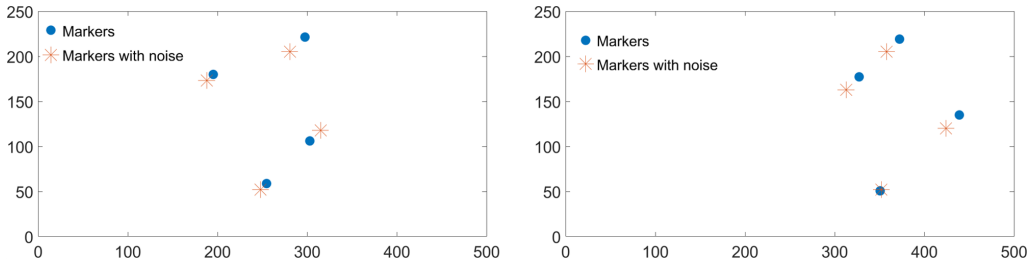

(b) Projection of markers from the marker configuration defined in Figure 2.1a on 2D camera images. The images represent the left and right camera image. The blue and red markers are projected with and without noise, respectively.

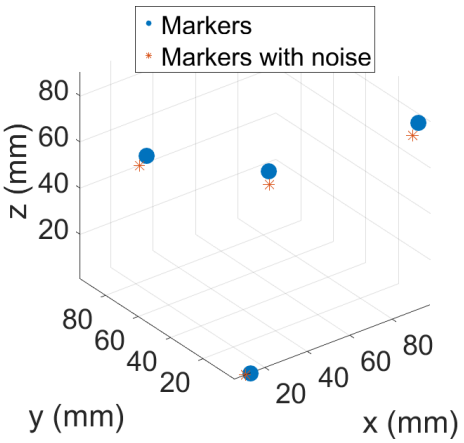

(c) Projection of marker locations from the 2D image back to 3D space. The blue markers are the projected markers from Figure 2.1a, the red markers (asterisk) are the projected markers after addition of noise.

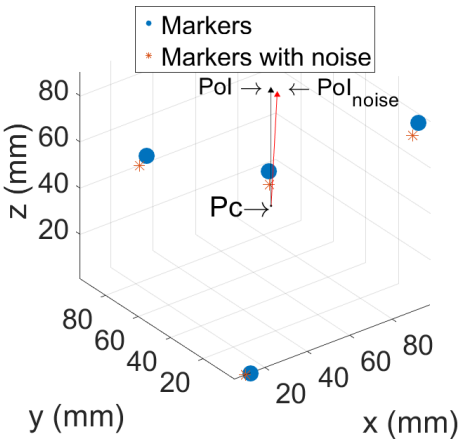

(d) Calculation of tooltip using the center of the configuration, $\mathbf{p}_c$. A vector between $\mathbf{p}_c$ and $\mathbf{p}_c + \begin{bmatrix} 0 & 0 & 50 \end{bmatrix}^T$ is defined and transformed to $\mathbf{p}_{oInoise}$ using a transformation that optimally transforms blue markers to red markers. Difference between the tip of both vectors is calculated as the error.

Figure 2.1: Overview of the projection to 2D, addition of noise, back-projection to 3D and calculation of the tooltip.

translation vector ${}^{1}\mathbf{t}_{WCS} = \mathbf{0}_{3,1}$. The transformation between camera 2 and WCS was equal to the transformation between both cameras. Therefore, ${}^{2}\mathbf{R}_{WCS} = {}^{2}\mathbf{R}_{1}$ and ${}^{2}\mathbf{t}_{WCS} = {}^{2}\mathbf{t}_{1}$, where ${}^{2}\mathbf{R}_{1}$ and ${}^{2}\mathbf{t}_{1}$ describe the transformation between camera 1 and camera 2. These variables were extracted from the extrinsic parameters obtained by the stereo camera calibration.

2.1.2 Projection of 3D marker to 2D camera image

Using the virtual camera model and epipolar geometry, a 3D point $\mathbf{P} = \begin{bmatrix} X & Y & Z \end{bmatrix}^T$ can be projected as a point $\mathbf{p} = \begin{bmatrix} u & v \end{bmatrix}^T$ on the 2D planes of the virtual cameras with the following equations [92]:

$$\begin{aligned} {}^{1}\mathbf{p}_h &= {}^{1}\mathbf{K} \begin{bmatrix} \mathbf{I}_3 \mathbf{0}_{3,1} \end{bmatrix} \mathbf{P}_h \\ {}^{2}\mathbf{p}_h &= {}^{2}\mathbf{K} \begin{bmatrix} {}^{2}\mathbf{R}_1 \, {}^{2}\mathbf{t}_1 \end{bmatrix} \mathbf{P}_h \end{aligned} \tag{2.2}$$

In these equations, point $\mathbf{p}_h = \begin{bmatrix} u & v & w \end{bmatrix}^T$ and $\mathbf{P}_h = \begin{bmatrix} X & Y & Z & W \end{bmatrix}^T$ are the homogeneous coordinates of $\mathbf{p}$ and $\mathbf{P}$, with w and W being scale factors of size 1. ${}^{1}\mathbf{p}_h$ is the projection of the marker on camera 1, whereas ${}^{2}\mathbf{p}_h$ is the projection on camera 2. The actual 2D-coordinates can be calculated by:

$$\mathbf{p} = \begin{bmatrix} \frac{u}{w} & \frac{v}{w} \end{bmatrix} \tag{2.3}$$

Before applying a projecting of the 2D points back to the 3D space, noise was added to ${}^{1}\mathbf{p}$ and ${}^{2}\mathbf{p}$, resulting in ${}^{1}\hat{\mathbf{p}}$ and ${}^{2}\hat{\mathbf{p}}$. This noise simulated the error that is introduced by the detection algorithm in the navigation system. Noise was simulated with a standard deviation, σ, of 1 pixel (Figure 2.1b).

2.1.3 Projection from 2D camera image back to 3D space

Back-projection of the 2D coordinates of the markers to the 3D space was realized with a MMSE estimator algorithm. The MMSE estimator algorithm made use of the Kalman update, based on a linear model, disturbed by measurement noise [93]:

$$\mathbf{z} = \mathbf{H}\mathbf{P} + \mathbf{n}, \tag{2.4}$$

with $\mathbf{z}$ being the observation vector, $\mathbf{H}$ the measurement matrix / model, $\mathbf{P}$ the point in the 3D space and $\mathbf{n}$ the noise as introduced by the measurement system. The noise had a Gaussian distribution with zero mean and covariance matrix $\mathbf{C}_n$. The Kalman update calculates a weighted average between a measurement and prior knowledge. More weight is given to the variable with higher certainty, which is deduced from the covariance matrices.

To derive a linear equation in the form of the functional structure of Equation 2.4, the calibration matrices ${}^{1}\mathbf{K}$, and ${}^{2}\mathbf{K}$ were divided in three rows, such that $\mathbf{K} = \begin{bmatrix} \mathbf{k}_1^T & \mathbf{k}_2^T & \mathbf{k}_3^T \end{bmatrix}$, with $\mathbf{k}_n^T$ being the n$^{\text{th}}$ row of the calibration matrix. Formulas in Equation 2.2 were combined and simplified to obtain the following equations for $\mathbf{z}$ and $\mathbf{H}$:

$$\mathbf{z} \overset{\text{def}}{=} \begin{bmatrix} ({}^{1}\hat{p}_1 \, {}^{1}\mathbf{k}_3^T - {}^{1}\mathbf{k}_1^T) {}^{1}\mathbf{t}_{WCS} \\ ({}^{1}\hat{p}_2 \, {}^{1}\mathbf{k}_3^T - {}^{1}\mathbf{k}_2^T) {}^{1}\mathbf{t}_{WCS} \\ ({}^{2}\hat{p}_1 \, {}^{2}\mathbf{k}_3^T - {}^{2}\mathbf{k}_1^T) {}^{2}\mathbf{t}_{WCS} \\ ({}^{2}\hat{p}_2 \, {}^{2}\mathbf{k}_3^T - {}^{2}\mathbf{k}_2^T) {}^{2}\mathbf{t}_{WCS} \end{bmatrix} = \begin{bmatrix} ({}^{1}\hat{p}_1 \, {}^{1}\mathbf{k}_3^T - {}^{1}\mathbf{k}_1^T) \mathbf{0}_{3,1} \\ ({}^{1}\hat{p}_2 \, {}^{1}\mathbf{k}_3^T - {}^{1}\mathbf{k}_2^T) \mathbf{0}_{3,1} \\ ({}^{2}\hat{p}_1 \, {}^{2}\mathbf{k}_3^T - {}^{2}\mathbf{k}_1^T) {}^{2}\mathbf{t}_{WCS} \\ ({}^{2}\hat{p}_2 \, {}^{2}\mathbf{k}_3^T - {}^{2}\mathbf{k}_2^T) {}^{2}\mathbf{t}_{WCS} \end{bmatrix} = \begin{bmatrix} 0 \\ 0 \\ ({}^{2}\hat{p}_1 \, {}^{2}\mathbf{k}_3^T - {}^{2}\mathbf{k}_1^T) {}^{2}\mathbf{t}_{WCS} \\ ({}^{2}\hat{p}_2 \, {}^{2}\mathbf{k}_3^T - {}^{2}\mathbf{k}_2^T) {}^{2}\mathbf{t}_{WCS} \end{bmatrix} \tag{2.5}$$

$$\mathbf{H} \stackrel{\text{def}}{=} \begin{bmatrix} ({}^{1}\mathbf{k}_{1}^{T} - {}^{1}\hat{p}_{1}\,{}^{1}\mathbf{k}_{3}^{T})\mathbf{I}_{3} \\ ({}^{1}\mathbf{k}_{2}^{T} - {}^{1}\hat{p}_{2}\,{}^{1}\mathbf{k}_{3}^{T})\mathbf{I}_{3} \\ ({}^{2}\mathbf{k}_{1}^{T} - {}^{2}\hat{p}_{1}\,{}^{2}\mathbf{k}_{3}^{T})^{2}\mathbf{R}_{1} \\ ({}^{2}\mathbf{k}_{2}^{T} - {}^{2}\hat{p}_{2}\,{}^{2}\mathbf{k}_{3}^{T})^{2}\mathbf{R}_{1} \end{bmatrix} \tag{2.6}$$

For a detailed explanation on the derivation of the measurement matrix $\mathbf{H}$ and observation vector $\mathbf{z}$, see [94]. The noise $\mathbf{n}$ was modeled in ${}^{1}\hat{\mathbf{p}}$ and ${}^{2}\hat{\mathbf{p}}$, completing Equation 2.4. The input for the Kalman update was ${}^{1}\mathbf{K}$, ${}^{2}\mathbf{K}$, ${}^{2}\mathbf{R}_{1}$, ${}^{2}\mathbf{t}_{1}$, ${}^{1}\hat{\mathbf{p}}$, ${}^{2}\hat{\mathbf{p}}$, $\hat{\mathbf{P}}_{prior}$, $\mathbf{C}_{prior}$ and $\mathbf{C}_{n}$. The variable $\hat{\mathbf{P}}_{prior}$, also named prior knowledge, was an unfounded guess of the marker location $\mathbf{P}$ and can therefore be every value as long as it is large and accompanied by a covariance matrix with large uncertainty, $\mathbf{C}_{prior}$. The noise covariance matrix $\mathbf{C}_{n}$ was calculated by:

$$\mathbf{C}_{n} = \hat{\mathbf{P}}_{prior}^{2}\,\sigma\mathbf{I} \tag{2.7}$$

With these variables, the Kalman update was applied, with:

Innovation matrix:	$\mathbf{S} = \mathbf{H}\mathbf{C}_{prior}\mathbf{H}^{T} + \mathbf{C}_{n}$
Kalman gain matrix:	$\mathbf{K} = \mathbf{C}_{prior}\mathbf{H}^{T}\mathbf{S}^{-1}$
Estimation:	$\hat{\mathbf{P}}_{estimate} + \mathbf{K}(\mathbf{z} - \mathbf{H}\hat{\mathbf{P}}_{prior})$
Covariance matrix of estimate:	$\mathbf{C}_{estimate} - \mathbf{K}\mathbf{S}\mathbf{K}^{T}$

A two stage approach was followed, first an initial estimation of $\mathbf{P}$ was calculated. This initial estimation was updated in the second stage. In the first stage, the Kalman update was used to estimate $\mathbf{P}$ by using $\hat{\mathbf{P}}_{prior}$ as prior knowledge, resulting in a weighted average of $\hat{\mathbf{P}}_{estimate\ 1}$ with the associated $\mathbf{C}_{estimate\ 1}$. The uncertainty of $\hat{\mathbf{P}}_{estimate\ 1}$ was lower than the uncertainty of $\hat{\mathbf{P}}_{prior}$. In the second stage, the algorithm used this $\hat{\mathbf{P}}_{estimate\ 1}$ and the corresponding covariance matrix as prior knowledge to update the estimation and derive $\hat{\mathbf{P}}_{estimate\ 2}$. Since the uncertainty of $\hat{\mathbf{P}}_{estimate\ 1}$ was smaller than the uncertainty of $\hat{\mathbf{P}}_{prior}$, $\hat{\mathbf{P}}_{estimate\ 2}$ converged to $\mathbf{P}$.

2.1.4 Error calculation

The projection and back-projection algorithm was implemented in Matlab to simulate the marker detection with and without simulated noise for different marker configurations. For each configuration, two sets of markers were reprojected; one without addition of noise, $\mathbf{M}_{real}$, being the gold standard, and one with the addition of noise, $\mathbf{M}_{noise}$ (Figure 2.1c). To evaluate performance, a point of interest, $\mathbf{p}_{oIreal}$, was calculated in a reproducible way. In the configuration without noise, a center point, $\mathbf{p}_{c}$, was calculated by averaging all marker coordinates in $\mathbf{M}_{real}$. $\mathbf{p}_{oIreal}$ was defined as:

$$\mathbf{p}_{oIreal} = \mathbf{p}_{c} + \begin{bmatrix} 0 & 0 & 50 \end{bmatrix}^{T} \tag{2.8}$$

This point of interest can be regarded as a vector linked to the DRF, starting from its center point to a point 50 mm away in the z-direction. To calculate $\mathbf{p}_{oInoise}$, the point of interest for $\mathbf{M}_{noise}$, $\mathbf{M}_{real}$ was transformed to $\mathbf{M}_{noise}$ by applying the Procrustes algorithm (Appendix B) [95, 96]. In this algorithm, coordinates of markers in both configurations were used as input. The algorithm determined the transformation of $\mathbf{M}_{real}$ to $\mathbf{M}_{noise}$ by finding the optimal alignment between the markers in both configurations. The same transformation was used to transform $\mathbf{p}_{oIreal}$ to $\mathbf{p}_{oInoise}$

(Figure 2.1d). The error ϵ of the configuration in a certain iteration was defined as the Euclidean distance calculated by:

$$\epsilon = \sqrt{\sum_{i=1}^{3} (\mathbf{p}_{oIreal_i} - \mathbf{p}_{oInoise_i})^2} \tag{2.9}$$

2.1.5 Monte Carlo Analysis

The aim of the simulation was to assess the performance of different marker configurations to be used for a DRF. Therefore, 10000 different configurations were randomly created by placing three markers in a box of 100 x 100 x 100 mm. These configurations were placed at $i = 100$ different orientations and positions in the trackers' field of view. At these different positions, noise was added $j = 100$ times and the error ϵ was calculated. The localization error for addition of noise in one position, ϵ_{noise}, is the sum of all individual errors:

$$\epsilon_{noise} = \frac{\sum_{j=1}^{100} \epsilon_j}{j} \tag{2.10}$$

The overall mean localization error for one configuration, ϵ_{total}, is the summation of ϵ_{noise} for all positions:

$$\epsilon_{total} = \frac{\sum_{i=1}^{100} \epsilon_{noise_i}}{i} \tag{2.11}$$

This ϵ_{total} gave an indication about how well the different DRFs did perform. To improve the selection procedure for finding the optimal DRF, the total localization errors for all 10000 marker configurations were sorted and the 500 configurations with the lowest ϵ_{total} were selected. The MCA was repeated for these 500 sorted configurations, however, with more iterations to improve the results. Noise was added for $j = 500$ iterations and the markers were positioned at $i = 500$ different locations. Again, ϵ_{total} was sorted to find the most optimal marker configuration.

To evaluate the influence of the number of markers, the method was repeated for DRFs with three, four and five markers. The influence of the size of the DRF was evaluated by taking the optimal marker configuration, and consequently scaling the DRF with factors from 0.05 to 5 times the original shape, with steps of 0.05. These scaled versions were used as input in the MCA with iterations of $i = j = 500$.

2.2 Results

Using the stereo calibration application, the camera parameters that were used to create the virtual optical tracker were obtained. The extrinsic calibration parameters were:

$${}^{2}\mathbf{R}_{1} = \begin{bmatrix} 0.965 & -0.010 & -2.64 \\ 0.011 & 0.999 & 0.047 \\ 0.263 & -0.008 & 0.965 \end{bmatrix} \text{ and } {}^{2}\mathbf{t}_{1} = \begin{bmatrix} 220.02 & 1.75 & 31.28 \end{bmatrix}^{T}$$

The intrinsic parameters of the camera calibration together with the specifications of the manufacturer are reported in Table 2.1. The results from the MCA for 10000 random marker configurations with three, four or five markers per DRF were

analyzed. The results are summarized in Table 2.2 and Appendix C (Figure C.1). The results show that the DRFs with three markers had a large error deviation, which was reduced in the case of four and five markers. Mean ϵ_{total} for three, four and five markers were 2.1472 mm (sd = 1.9390), 1.3023 mm (sd = 0.3638) and 1.0298 mm (sd = 0.155) and lowest errors were 1.0187, 0.8848 and 0.7622 mm, respectively.

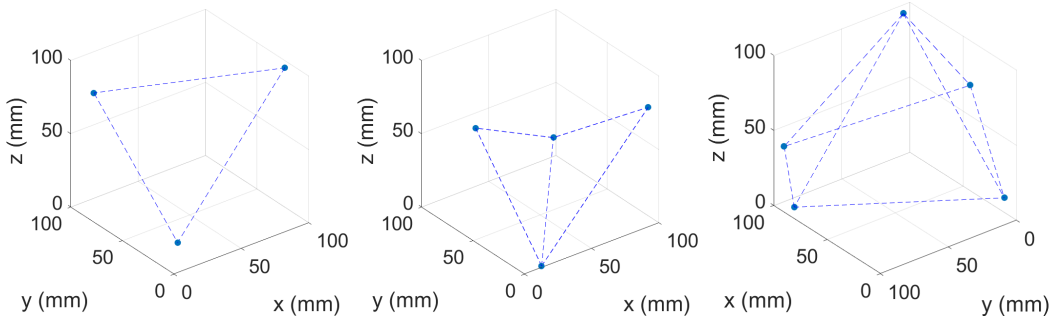

Figure 2.2: Optimal DRF configurations determined using the MCA for three, four and five markers. Note the high nonlinearity in the DRFs. a) Three markers b) Four markers c) Five markers.

Table 2.1: Intrinsic calibration parameters.

	K (Matlab)	**K** (manufacturer)
Camera 1	$\begin{bmatrix} 571.74 & 0 & 315.27 \\ 0 & 588.31 & 235.58 \\ 0 & 0 & 1 \end{bmatrix}$	$\begin{bmatrix} 605.62 & 0 & 319.83 \\ 0 & 605.99 & 242.25 \\ 0 & 0 & 1 \end{bmatrix}$
Camera 2	$\begin{bmatrix} 570.74 & 0 & 303.62 \\ 0 & 587.65 & 235.56 \\ 0 & 0 & 1 \end{bmatrix}$	$\begin{bmatrix} 608.30 & 0 & 302.20 \\ 0 & 608.96 & 241.85 \\ 0 & 0 & 1 \end{bmatrix}$

The result of the MCA using the 500 most optimal DRFs selected from the 10000 random DRFs is visualized in Table 2.3 and Appendix C (Figure C.2). Mean ϵ_{total} for the DRFs were 1.1014 mm (sd = 0.0365), 0.9403 mm (sd = 0.0246) and 0.8336 mm (sd = 0.0169), respectively for DRFs with three, four or five markers. The most optimal configurations with three, four and five markers had an ϵ_{total} 0.9804, 0.8536 and 0.7620 mm, respectively.

The most optimal marker configurations for three, four and five markers are shown in Figure 2.2. Results showed that the markers were distributed in such a way that the total volume of 100 x 100 x 100 mm was used. Furthermore, the configurations were highly nonlinear.

The four-marker model with the lowest error was selected as the most optimal configuration for a DRF. To assess the influence of the scale on the performance, scaled versions of this model were used as input for another MCA. The results are shown in Figure 2.3. A minimum ϵ_{total} was seen when the scale factor was 2 (0.7339 mm). This factor, however, resulted in DRFs having a size of around 20 cm, which

Table 2.2: Absolute errors calculated by MCA for 10000 random configurations.

	Three markers	**Four markers**	**Five markers**
Mean ϵ_{total} (mm)	2.1472	1.3023	1.0298
Standard deviation (mm)	1.9390	0.3638	0.1555
5^{th} percentile (mm)	1.1902	1.0019	0.8538
95^{th} percentile (mm)	4.3236	1.8597	1.3230
Highest ϵ_{total} (mm)	43.2063	16.4821	2.9461
Lowest ϵ_{total} (mm)	1.0187	0.8848	0.7622

Table 2.3: Absolute errors calculated by MCA for 500 optimal configurations.

	Three markers	**Four markers**	**Five markers**
Mean ϵ_{total} (mm)	1.1014	0.9403	0.8336
Standard deviation (mm)	0.0365	0.0246	0.0169
5^{th} percentile (mm)	1.0339	0.8920	0.8000
95^{th} percentile (mm)	1.1558	0.9743	0.8531
Highest ϵ_{total} (mm)	1.1793	0.9980	0.8580
Lowest ϵ_{total} (mm)	0.9804	0.8536	0.7620

is unwanted in a clinical situation. Hence, it was opted to use a scale of 0.75 as the optimal size. For a scale factor of 0.75, ϵ_{total} was 0.9892 mm.

To consider the design of the DRFs with different errors, three models with 4 markers were selected; an 'optimal' DRF (ϵ_{total} = 0.8536 mm), a 'moderate' DRF (ϵ_{total} = 0.9870 mm) and a 'worst' DRF (ϵ_{total} = 16.4821 mm), visualized in Figure 2.4a-c. Using these selected marker configurations, DRFs were designed in SolidWorks (Dassault Systèmes, Waltham, MA, USA) (Figure 2.4d-f). The frames were manufactured using SLS 3D-printing (Oceanz, Ede, Netherlands) at a scale of 75%. The 'optimal' configuration was decently distributed in the cubic volume, whereas the other two had a collinear shape.

2.3 Discussion

In this study, several aspects on determining the optimal marker configuration were addressed. A virtual optical tracker was generated using the intrinsic parameters of the tracker used in the coming chapters. The obtained results after performing a Monte Carlo analysis using this virtual model gave insight in determining the optimal marker configuration in terms of error reduction. The findings must be taken into consideration when designing reference frames for clinical applications.

Number of markers

A positive relation between the number of markers and the accuracy on the tracking system was found. ϵ_{total} decreased with 13% from 0.9804 to 0.8536 mm when the

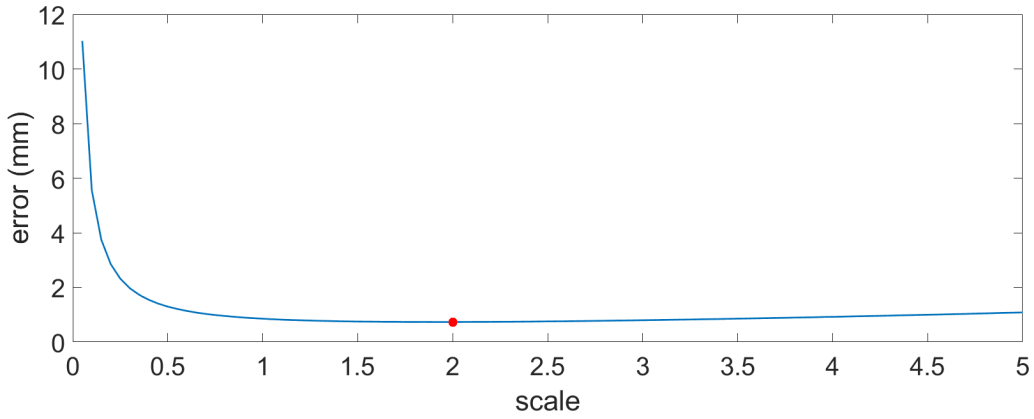

Figure 2.3: Influence of scaling of the 'optimal' DRF on accuracy. The 'optimal' DRF was scaled with factors of 0.05 to 5 and the error for the scaled DRF was calculated using Equation 2.11. Optimal scale factor was 2 (red dot).

'optimal' DRF of four markers was used, instead of the DRF with three markers. Using five markers compared to four, the performance increased with 11% from 0.8536 to 0.7620 mm. These results are in accordance with the 15% increase when adding one marker to a DRF with three markers, as reported by Maurer et al. [54].

Distribution of the markers

The simulation showed that the configuration with the largest error was a linear DRF. On the contrary, the DRFs with low errors had a wide distribution of the markers. These findings strengthen the claim that a nonlinear DRF will perform better in terms of accuracy. Results of the current study showed that the markers should be placed with the largest possible distance between each other. If this rule is applied, a regular polyhedron will be formed. This corresponds with the findings of West et al., stating that the distribution of a DRF should be isotropic, like a tetrahedron in the case of four markers [60].

Scaling of the DRF

Scaling of a DRF has direct influence on the accuracy of the tracking system (Figure 2.3). When the 'optimal' DRF was scaled, the error was high with small-sized DRFs, optimal when the scale was 2 and increased again when the DRF was larger. A marker localization error in a small DRF has a larger influence on the rotational error in comparison with a large DRF. A relation between scale and error comparable to the findings was reported by Fitzpatrick et al., who discovered the following relation [66]: $TRE^2 = \frac{1}{s^2}$, with s being the scale factor. In the present study, this relationship was seen as well. However, the error did not converge but increased again after a scaling factor of 2. The explanation lies in the fact that a large DRF always has one or several markers with a large distance to the trackers' forward direction. It is known that tracking becomes more inaccurate as the distance to the tracker increases [52, 63]. The assumption is that this negative influence is larger than the positive effect of using a larger DRF.

Because of clinical relevance, it was decided to evaluate the design of DRFs with four markers. First of all, use of three markers is not possible with the used tracker as it only detects objects with four markers. Using the MCA, it was shown that the

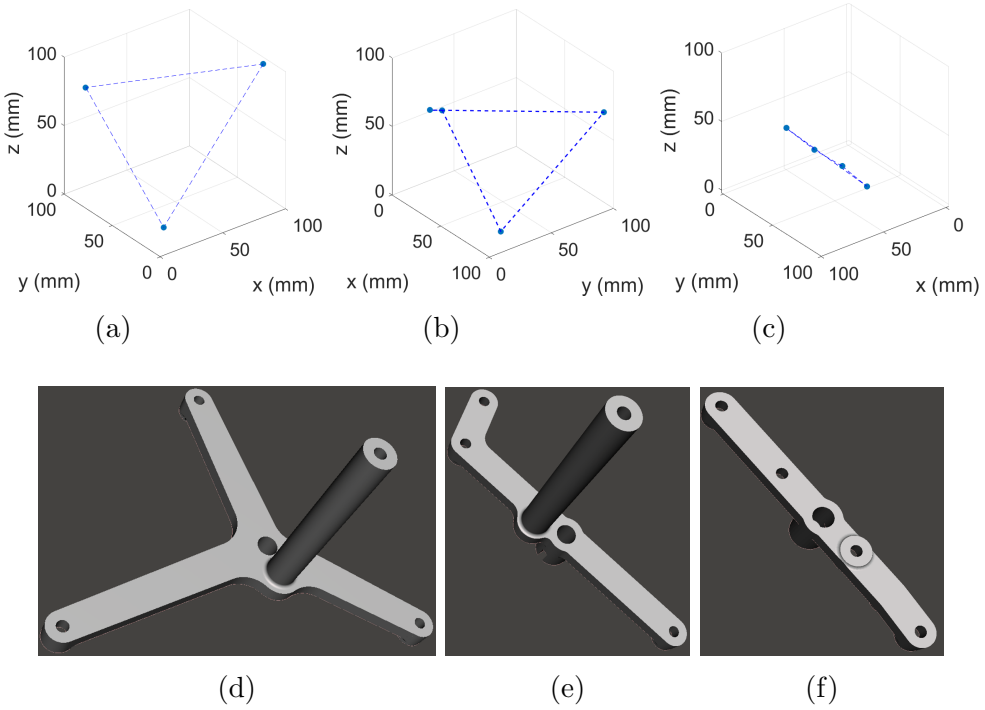

Figure 2.4: Different DRFs selected using the MCA. The selected DRFs are defined as 'optimal' (a,d), 'moderate' (b,e) and 'worst' (c,f). a-c) The location of the markers calculated using the MCA. d-f) The DRFs designed in SolidWorks. The four small cylinders in the frames can be used used to fixate the markers.

use of five markers improved performance with 11%. It was reasoned, however, that the use of one extra marker could introduce occlusion of markers during tracking. The optimal size for the optimal DRF was two times the original design, however, this seemed to be too large for clinical practice. Therefore, the 'optimal' DRF with four markers was rescaled to 75%, increasing the theoretical error from 0.8536 to 0.9892 mm.

In this study, a virtual world was created, consisting of a tracking system with two different cameras and a marker configuration at different locations. Using this simulation it was possible to reproduce the results in literature and to find an optimal DRF. A calibration method was used to calculate the intrinsic and extrinsic parameters of the optical tracker. The intrinsic parameters were slightly different than the parameters specified by the manufacturer in the calibration files. This difference can be explained by the fact that in the present study, calibration is limited because the checkerboard was not IR-reflecting.

The explained method is robust, repeatable and cheap. The simulation can be used to generate relevant information that aids in improving the performance of the system. The result can even be used to optimize conventionally used reference frames. Currently, instruments used in IGS often contain three or four markers, distributed in one plane. This is an unwanted condition since the performance can be optimized using a wider distribution. It is, however, possible that manufacturers produce the DRFs deliberately in one plane to limit the chance of markers occluding each other in the line-of-sight of the tracker.

The MCA can be extended by adding more restrictions, for example by assigning the marker locations in only one plane, or limit the orientation of the DRF with

respect to the cameras. It is also possible to investigate the effect of the marker placement on the probability of markers being occluded by each other. For this, the distance between the projected points on the 2D-camera images can be evaluated to assess whether two markers overlap.

Optimal marker configurations for three, four and five markers were investigated using a virtual DRF. For clinical use, it is assumed that four markers are more favorable than five markers. For optimal results, the optimal DRF would have dimensions of around 20 cm. This size, however, is unusable in clinical practice, hence the size of the DRF was reduced to around 7.5 cm. For clinical use, the advice is to use a DRF with a nonlinear configuration, at least four markers and with a size between 5 and 10 cm, depending on the clinical application. The 'optimal' DRF determined by the MCA satisfied these requirements and will therefore be used for evaluation of an object-oriented navigation system in the next sections.

Chapter 3

Different conditions and accuracy

Several conditions can influence the accuracy of an optical navigation system. It is important to identify these sources of errors such that this information can be incorporated in the development of clinical applications. A known source of error is the temperature of the tracker. Due to the warming of the electronic components, the intrinsic parameters of the cameras change, introducing a shift in marker localization [59, 97, 98]. Over time, a turned-on optical navigation system produces heat. In the tracker, infrared (IR) light is emitted to illuminate the retroreflective markers. This process and the power supply for electronic components add up to the heating of the device [97]. Deviations of up to 0.7 mm were seen between a cold and a warmed-up tracker [98]. Camera calibration, therefore, always needs to be done after the temperature of the device reached its equilibrium. This, however, can lead to inaccurate tracking in the first 15 to 30 minutes after the device is turned on.

Another potential error in optical tracking is introduced by filtering of the measured data. In the application programming interface (API) of the PST Base optical tracker, three filter settings can be adjusted to reduce jitter. Both position and orientation can be filtered using a slider bar ranging from 0 to 1. Application of these filters might improve the workability of the system, but it is unknown what the influence on accuracy is. Since the tracker will be used in the OON system, it is important to know the influence of the filters on the performance of the tracker. The manufacturer of the system advises to use a filter setting of 0.8.

A third error influencing the accuracy is introduced along the axis away from the tracker, the z-direction [63, 97–99]. This is, however, dependent on the design of the tracker. The angle and space between two cameras are important elements. A larger angle and more space between the cameras reduces the error in the z-direction [97, 98]. Furthermore, inaccuracies might increase near the limits of the field of view in x- and y-direction [63]. These errors can be related to radial distortion and errors in the calibration parameters [52].

Accuracy measurements are often analyzed after implementation of trackers in a clinical application, which is regarded as the target registration error [100–103]. Methods which determine the performance of the optical tracking system alone rely on comparison with a ground truth. Khadem et al. compared five different tracking machines by positioning a DRF on a linear testing apparatus (LTA) [52]. Wiles et al. used a coordinate measurement system (CMM) on which a DRF was mounted [63]. In these studies, the position measured by the tracking system was compared to the position of the LTA or CMM to determine the accuracy of the system.

Since optimal circumstances for the optical tracker will result in better overall

accuracy in a navigation system, it is important to investigate what these optimal circumstances are. Therefore, the influences of the described conditions on accuracy were evaluated in this chapter by comparing it with the ground truth, a milling machine. DRF locations measured by the tracker were compared with reference coordinates. The warming up effect, different filter settings and different locations of the dynamic reference frame (DRF) with respect to the tracker were evaluated. This research will answer the second sub-question: *What is the influence of different conditions on the accuracy of the tracker?*

3.1 Methods and Materials

3.1.1 Measurement setup

In the following experiments, the optimal DRF was mounted on a milling machine having an accuracy of 0.05 mm to compare measurements of the tracker with a preprogrammed path (Figure 3.1). For evaluating the warming up and different filter settings, the path was programmed within a motion volume of 20 x 10 x 20 cm. The machine stopped for 2 seconds at 27 locations, further denoted as the reference coordinates (Figure 3.1a). Every location in the path was visited three times. For evaluation of the influence of the location of the DRF in the trackers field of view (FOV), reference coordinates in a larger volume (50 x 10 x 50 cm) were used (Figure 3.1b). This time, the machine stopped at 272 positions and each location was visited twice.

In the experiments, the orientation used in Figure 3.1a and 3.1b was used to express the axis. Distance between tracker and the center of the motion volume was 90 cm (z-direction) and 19 cm (y-direction). The actual measurement setup is shown in Figure 3.2. In all experiments, the location of the DRFs was tracked using the optical tracker and data was saved with 120 Hz. No filtering was applied during the acquisition.

Measurement data was imported in Matlab and the measured locations of the DRF were obtained. For each location, 150 data samples were used to calculate the averaged position of the DRF.

3.1.2 Warming up of tracker

For comparing a cold and warmed-up optical tracker, measurements were first performed with a cold tracker. The measurement was finished after approximately 7.5 minutes. After warming-up time of 30 minutes was reached, the other experiment was performed. To determine a shift between both measurements, the measured coordinates before and after warming up were subtracted.

To determine a shift in marker location during warming-up time, two DRFs, further denoted as DRF1 and DRF2, were positioned in the center of the FOV of the tracker at a fixed distance of 50 cm. Tracker and DRFs were fixated and did not move during approximately 30 minutes of data acquisition to create a static environment. Data was saved and analyzed to determine whether the measured position of the DRFs shifts during warming up. For better representation of the data, the difference between coordinates of the two DRFs was standardized by:

$$p_s = p - \frac{\sum_{i=1}^{n} \mathbf{p}_i}{n}, \tag{3.1}$$

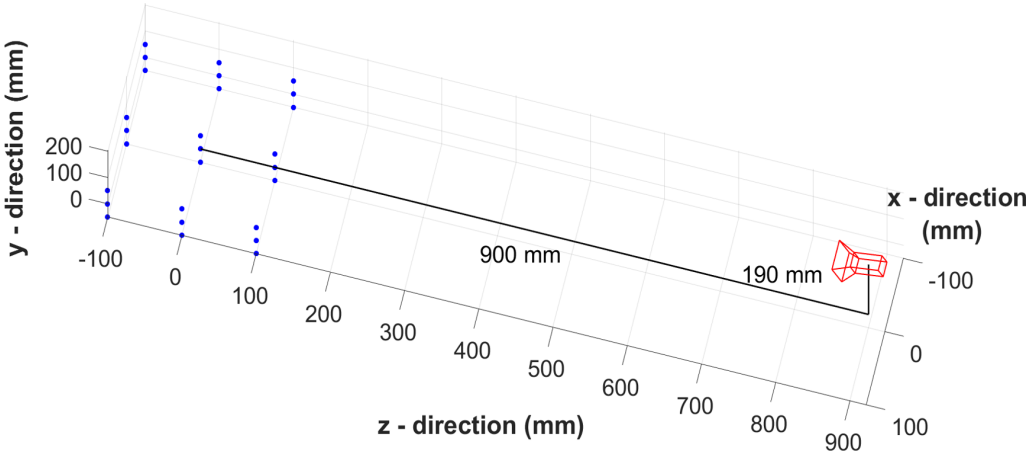

(a)

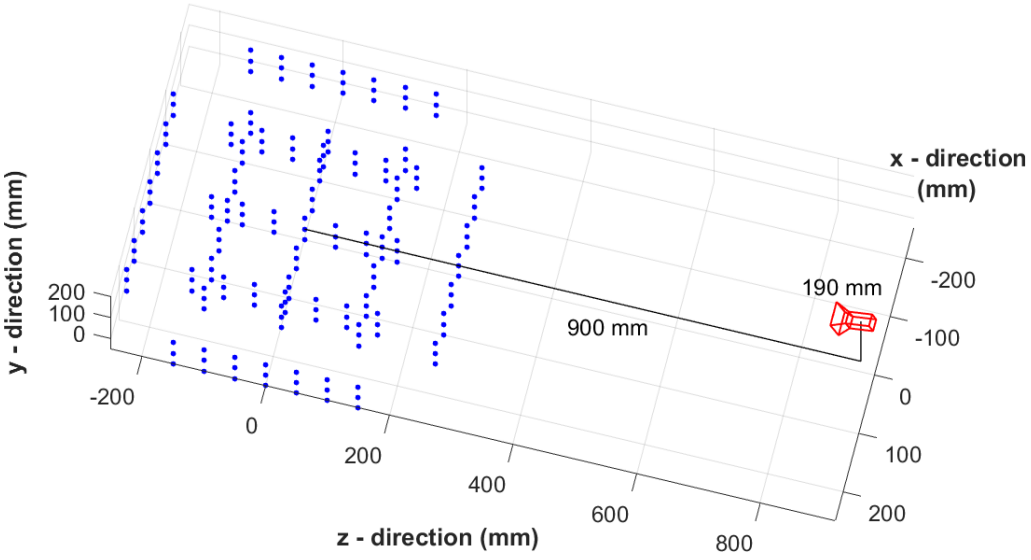

(b)

Figure 3.1: Measurement setup to test performance the with corresponding axis and dimensions. The optical tracker is shown in red, the reference locations / coordinates in the volume are shown as blue spheres. a) Setup used to investigate the influence on accuracy for warming up and different filter settings. b) Setup used to investigate the influence on accuracy for different DRF locations with respect to the tracker.

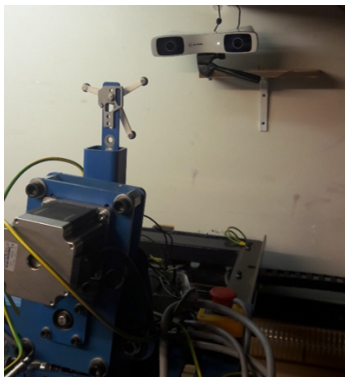

Figure 3.2: Optical tracker and milling machine. The DRF mounted on the milling machine followed a preprogrammed path as the optical tracker tracked the location of the DRF.

with p being the x-, y- or z-value to be standardized, p_s the standardized x-, y- or z-value and n the number of values in the data $\mathbf{p}$.

3.1.3 Filter settings

The influence of the built-in filters in the optical tracker was tested by performing the same measurements as described in Section 3.1.2, however, with different filtering settings. First, measurements were performed with all filters off. In the second and third condition, position and orientation filters were turned on with values of 0.8 and 1, respectively.

To evaluate the influence of the filters, the trackers' coordinate system was aligned with the milling machines' coordinate system using the Procrustes algorithm (Appendix B) [95, 96]. The input in this algorithm was the reference coordinates of the milling machine and the corresponding measurements of the optical tracker. Distance differences between aligned measured coordinates and the reference coordinates were calculated to evaluate the performance of the different conditions.

3.1.4 Location of DRF in the field of view

For analyzing the influence of the position of the optimal DRF in the FOV of the tracker, the extended path was used (Figure 3.1b). The distance difference between measured and reference coordinates was calculated as in Section 3.1.3.

Since the measurements were compared to the ground truth, the milling machine, this gave an indication about the trueness of the system. To evaluate the precision, the difference between two measurements at the same location was calculated by subtracting the measured coordinates measured in both rounds.

3.1.5 Statistical analysis

For the experiments with the different filter conditions, it was evaluated whether the measurements were significantly different. The Anderson-Darling test was used with a significance level of 0.05 [104]. If the hypothesis of this test was accepted, the Euclidean distance was assumed to be normally distributed and a paired t-test was used to compare the differences between the conditions [105]. If the hypothesis of the normal distribution for the data was rejected, the Wilcoxon signed rank tests was used to determine whether the found differences in the experiment where significant [106]. These tests were performed using a significance level of 0.05, to reject the hypothesis that the mean Euclidean distances between two experiments is not different.

3.2 Results

3.2.1 Warming up of tracker

The difference between the locations measured with a warmed-up and cold device is summarized in Table 3.1 and Appendix C (Figure C.3). The mean absolute error between marker locations in the x- and y-direction was 0.08 mm (sd = 0.0352) and 0.07 mm (sd = 0.0698), respectively. In the z-direction, away from the tracker, the mean absolute error was 0.32 mm (sd = 0.1182).

The results from the experiment in the static situation are visualized in Figure 3.3, showing the values of x-, y- and z-coordinates during warming up. The difference between the start and the end of the measurement in the x- and y-direction was 0.02 and 0.14 mm, respectively. The shift in z-direction was larger, with a magnitude of 0.34 mm. The location shift stopped after around 25 minutes. The graph in Figure 3.3a visualizes the jitter generated by the tracker. Jitter in x-, y- and z-direction was 0.01, 0.02 and 0.03 mm, respectively.

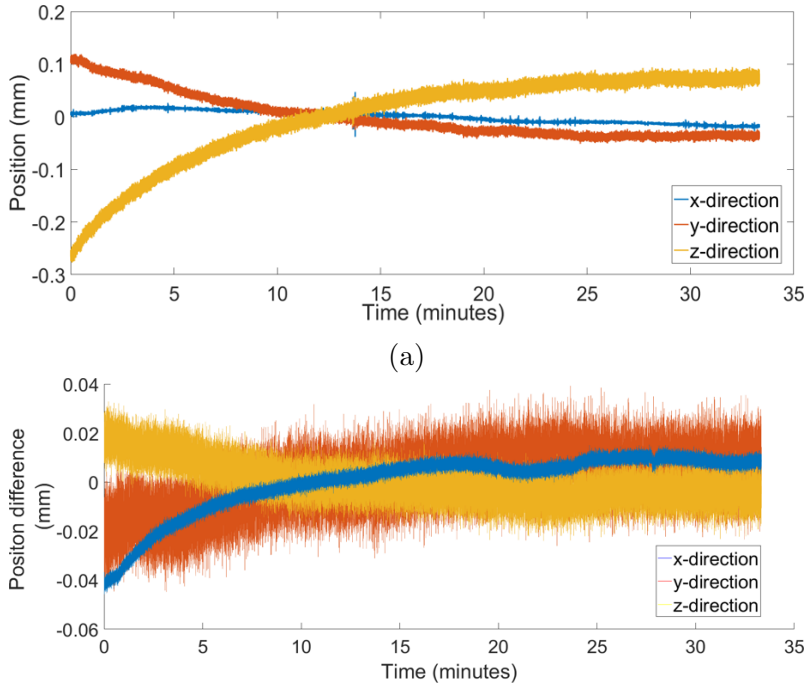

Figure 3.3: Influence of warming up on performance. a) Both tracker and DRFs were kept in a static position during warming up of the device. A shift of the standardized DRF position is seen in the x-, y- and z-direction. Bandwidth of the plots show the effect of the jitter. b) Standardized difference between location of DRF1 and DRF2 in all directions.

The shift of both DRFs relative to each other was determined by calculating the difference between the coordinates of both frames. The standardized difference is visualized for the different directions in Figure 3.3b. Shifts of the frames with respect to each other were seen, however, they all were below 0.05 mm.

Table 3.1: Influence of warming-up of the optical tracker on performance. Absolute difference between coordinates measured by a cold and warmed-up optical tracker are reported.

	Mean error ± sd (mm)	**Max. error (mm)**
X-direction	0.08 ± 0.0352	0.15
Y-direction	0.07 ± 0.0698	0.23
Z-direction	0.32 ± 0.1182	0.65

3.2.2 Filter settings

The results of the filter settings are visualized in Table 3.2 and Appendix C (Figure C.4). The mean Euclidean distance for the situation without filtering was 1.40 mm (sd = 0.66). A filter of 0.8 and 1 resulted in a mean error of 1.39 mm (sd = 0.65) and 1.98 mm (sd = 0.50), respectively.

The Wilcoxon signed rank tests was used as the Euclidean distances of the measurements in the experiments were tested to be not normally distributed. No significant differences were found between applying a filter of 0.8 or no filter ($p = 0.207$). Significant difference were found between the measurements with no filter or a filter of 0.8 and measurements with a filter of 1 ($p < 0.001$).

Table 3.2: Influence of different filter settings on tracker performance. Mean and maximal Euclidean distances between measured and reference coordinates are reported.

	Mean Euclidean distance ± sd (mm)	**Max. Euclidean distance (mm)**
Filter = 0	1.40 ± 0.66	2.35
Filter = 0.8	1.39 ± 0.65	2.38
Filter = 1	1.98 ± 0.50	2.93

3.2.3 Location of DRF in the field of view

To evaluate the trueness of the navigation system in different directions, the trackers' measurements were subtracted from the reference coordinates. The mean and highest values for the Euclidean distance and the absolute difference in x-, y- and z-direction are summarized in Table 3.3 and Appendix C (Figure C.5). Mean errors in x- and y-direction were 0.39 mm (sd = 0.30) and 0.39 mm (sd = 0.26), respectively, whereas the error in the z-direction was 5.18 mm (sd = 2.44). The maximal reported Euclidean distance was 8.94 mm. The errors seen in this experiment are mainly due to the large inaccuracy in the z-direction, clearly shown in Figure 3.4.

The precision of the system was calculated by subtracting the coordinates from the first and second measurements of all 272 locations (Table 3.3 and Appendix C (Figure C.6). Mean difference was 0.01 mm (sd = 0.01) in the x-direction, 0.02 mm (sd = 0.01) in the y-direction and 0.04 mm (sd = 0.03) in the z-direction. Mean Euclidean distance for the precision was 0.06 mm (sd = 0.03), with a maximal error of 0.32 mm.

3.3 Discussion

The performance of the tracker was investigated under different conditions. The evaluated conditions were the warming up of the tracker, different filter settings and the distance between DRF and tracker. The results of these experiments provided essential information that can be used to optimize the use of the tracker in a clinical setting.

Table 3.3: Trueness and precision of the optical tracker, expressed as mean and highest errors.

	Trueness		**Precision**	
	Mean error ± sd (mm)	**Max. error (mm)**	**Mean error ± sd (mm)**	**Max. error (mm)**
X-direction	0.39 ± 0.30	1.52	0.01 ± 0.01	0.08
Y-direction	0.39 ± 0.26	0.92	0.02 ± 0.01	0.04
Z-direction	5.18 ± 2.44	8.93	0.04 ± 0.03	0.32
Euclidean distance	5.26 ± 2.36	8.94	0.06 ± 0.03	0.32

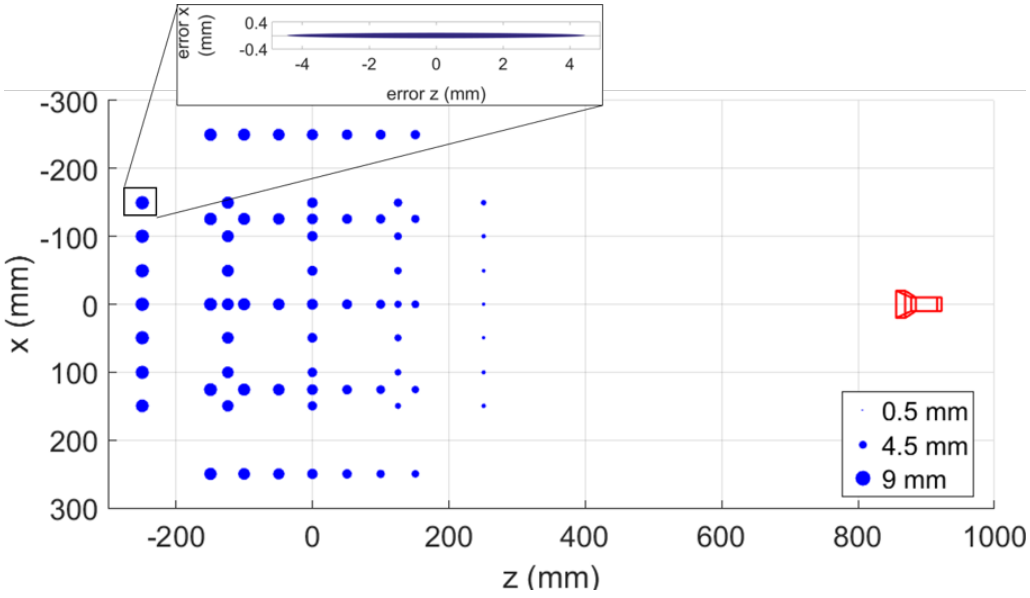

(a)

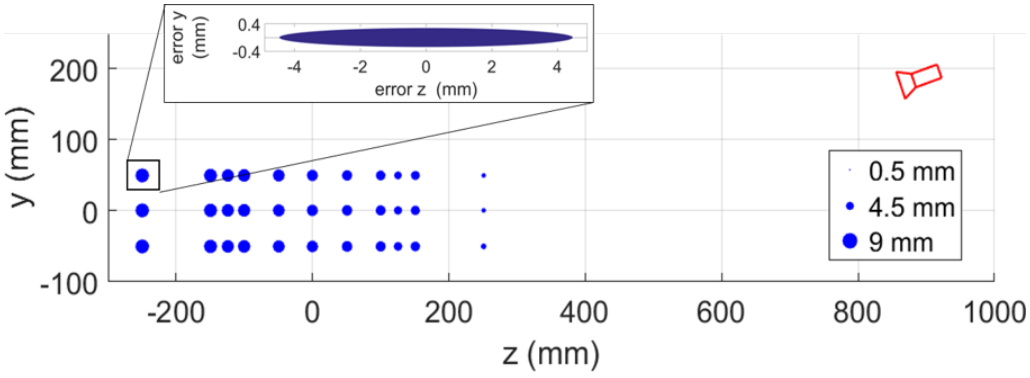

(b)

Figure 3.4: Influence of DRF location on performance. Distribution of the Euclidean distances in the measurement volume at the location of the DRF, indicated as blue circles. A larger circle represents a larger Euclidean distance. The close up shows the errors in the corresponding directions. a) Top view (x-z plane) b) Side view (y-z plane)

Warming up of optical tracker

Results of the first experiment showed a shift in DRF location during warming up of the device in the first 25 minutes. Measurements before and after warming up showed a positional drift of 0.32 mm for the z-direction. A DRF in a static position with respect to the tracker underwent a shift of the same magnitude in the z-direction (0.34 mm), during warming up of the tracker. These results are in accordance with literature. Trübswetter et al. reported a positional deviation of 0.7 mm during warming up, but noted a difference in shift between different trackers [98]. The shift between two different DRFs (< 0.05 mm) was small in relation with the jitter of approximately 0.03 mm.

For optimal performance, it is advised to wait at least 30 minutes after turning the tracking device on. The time causes the tracker to reach its thermal equilibrium. Afterwards, no large shifts due to temperature change are expected. The shift was almost equal for two different DRFs close to each other. Hence, the assumption can be made that warming up will not influence the relative tracking accuracy within the coordinate system of the tracking system.

Filter settings

Significant differences were seen in measurements when different filter settings were used. If the filters were maximal, the error was significantly higher than when no filter was applied. A filter value of 0.8 did not show a significant difference with applying no filter. These results show that it is possible to use the advised 0.8 filter value for tracking DRFs. This will improve the usability of the system as it reduces jitter. This will eventually improve the quality of the OON system as it is unpleasant when this jitter is seen during movement of the visualized objects. It is advised not to use the filter setting of 1 as this can yield to a significant reduction in performance.

DRF location

The results for the positioning of the DRF at different locations in a measurement volume of 50 x 50 x 10 cm showed errors up to 8.9 mm. These errors were mainly due to large inaccuracies in the z-direction. Whereas the mean absolute distance between the measured and programmed position in x- and y-direction was 0.39 mm, the error was 5.18 mm in the z-direction. The found error in the z-direction can cause dangerous situations if this error will propagate in clinical applications.

The accuracy dependency in the z-direction is described by literature [63]. However, errors of this magnitude were not reported as mean errors lower than 0.5 mm were found [52,63]. A RMS of 0.5 mm or lower was specified by the manufacturer of the optical tracker. Because of these facts, the large deviations in the current study were therefore not expected. It is difficult to explain what introduced this error, but testing more (different) trackers will provide information whether the findings are an exception.

The inaccuracy in the z-direction can be solved using different approaches. First, as the design of a tracker contributes for a large part to the error in the z-direction, it must be evaluated if trackers with more distance between both cameras are more accurate. Another solution is to use two combined tracking devices rotated 90° in the x-z plane. This setup can probably combine the high accuracy in the x- and y-direction of both trackers, resulting in a more reliable navigation environment.

Lastly, to compensate for the inaccuracy in the z-direction it must be investigated whether use of error correction improves results. Several error correction methods are described by Kindratenko et al. [107]. The correction is realized by comparing measurements with an accurate ground truth and compensating for the difference between both measurements [108].

Contrary to the low trueness, the precision of the optical tracker was high. Every location was measured twice, with a maximal deviation of 0.32 mm. The mean deviation between both measurements was below 0.05 mm in x-, y- and z-direction. This proves that the tracker is able to highly reproduce measurements.

It can be concluded that the performance of the tracker was influenced by the warming up of the device. Furthermore, errors were significantly higher when a filter of 1 were used, compared to 0.8 or 0. For optimal performance, a filter of 0.8 can be used. This filter reduces jitter but does not significantly affect performance. These considerations have to be taken into account when the tracker will be used for further evaluation.

Measured precision of the tracker was high, however, the trueness was low. The accuracy in clinical applications needs to be far below the maximal error of 9 mm found in this study. Therefore, it must be evaluated whether other, clinically implemented trackers show the same deviations. It must also be investigated how the low accuracy of the tracker will influence the accuracy of the OON system in potential clinical applications.

Chapter 4

Object-oriented navigation

Unstable pelvic fractures are generally treated by open reduction and internal fixation (Figure 1.3b) [26]. This surgical approach results in a direct view on the fracture site. In this way, the fracture site can be cleaned and the quality of reduction can be assessed during surgery. However, the approach is often accompanied by high blood loss [26]. To tackle this problem, surgical navigation has been introduced to stabilize pelvic fractures in a minimal invasive way [75, 109]. With this approach, percutaneous screws can be planned preoperatively and the specialist is guided intra-operatively to place the screws according to the surgical plan (Figure 1.3c). This method makes closed reduction and internal fixation possible, reducing blood loss and improving surgical outcome [33, 45]. In heavily displaced fractures, however, this method is limited as it does not guide the reduction of the fragments [33,75]. In both open reduction and in minimal invasive surgery, fluoroscopic images are used to deduce whether the desired reduction is achieved [75, 76, 109]. As the anatomy of an impaired pelvic ring is complex, it is difficult to adequately assess the quality of the reposition using these 2D images [36].

A possible solution to this problem is the use of object-oriented navigation (OON). This technique facilitates tracking of separate objects [76, 110]. The spatial relation of the objects is displayed using virtual 3D models of the physical objects. In this way, separate bone fragments can be monitored without making large surgical incisions [76]. Using the displayed 3D information, the reduction can be evaluated real-time [76]. As OON can facilitate minimal invasive surgery, it can potentially reduce blood loss, improve surgical outcome and provide improved intra-operative evaluation of the reduction [33, 45, 76, 110]. Furthermore, OON enables to translate the preoperative plan to the patient. This is another advantage as the only currently available method to translate the preoperative plan to the surgical site is the use of patient-specific prebended fixation plates [34, 39]. The plates guides the specialist in some extent, however, the guidance for fragment reduction in complex pelvic surgery is doubtful and the procedure requires open reduction [111].

Several implementations of OON for fracture reduction are described. Joskowic et al. used the technique to guide reduction of fractures in long bones [110]. Dagnino et al. combined OON with a robot system to guide the robot in reduction of articular fractures [76]. Chen et al applied the method for pelvic surgery, tracking a 3D printed implant to replace a resected iliac wing [45]. In their approach, tracking of both patient and implant made it possible to bring the implant to the resected part of the pelvis [45].

These examples showed the potential of OON. The OON technique can solve the shortcomings in the current pelvic fracture treatment and it must be investigated

whether it can be used to reduce unstable, displaced pelvic fractures. A correct implementation of OON will be an adequate guidance for the specialist in minimal invasive surgery. Eventually, it can lead to reduced blood loss and surgery time, improved patient outcome and better healthcare.

In the current chapter, the development of an OON system that can eventually be used to improve fracture repair is described. In addition, the accuracy of the system is evaluated under optimal conditions. The present study will provide an answer to the third sub-question: *What is the accuracy of object-oriented navigation?*

4.1 Methods and Materials

4.1.1 Object-oriented navigation system

The PST Base was used for object tracking in the 3D space. Using the device, it was possible to train / create new objects with four or more retroreflective markers. The locations of the markers in trained objects were exported and denoted as $\mathbf{p}_{tracker}$.

Unity (Unity Technologies, San Francisco, USA), a game engine was used for the visualization of 3D models of tracked objects. This software package enables scripting in C# and javascript and facilitates to build applications for virtual and augmented reality devices. Virtual 3D models of tracked objects were imported in Unity using the stereolithography format. The locations of the markers with respect to these 3D models were denoted as $\mathbf{p}_{UNITY}$. Using a custom made C# script, tracking data from the optical tracker was imported in the Unity game engine with 120 Hz.

Objects can be trained with the software of the optical tracker, giving the objects get their own position and orientation in the coordinate system of the tracker. To bring the objects in the right position and orientation in the Unity coordinate system (UCS), the imported 3D models were transformed to this UCS. The transformation was realized by using the Procrustes algorithm, finding the transformation matrix from the trackers' coordinate system to the UCS, ${}^{UNITY}\mathbf{T}_{tracker}$ (Appendix B) [95]. A C# script calculated ${}^{UNITY}\mathbf{T}_{tracker}$ for each object using $\mathbf{p}_{tracker}$ and $\mathbf{p}_{UNITY}$ and transformed the objects correctly in the UCS.

The position of the imported models relatively to each other was representing the planned situation. During tracking of objects, visual feedback was given by means of the color of the tracked virtual object. If the tracked object enclosed the planned position the color changed from red to green.

4.1.2 The tight-fit experiment

To evaluate the accuracy the object-oriented navigation system, an optimal situation was created: the 'tight-fit' experiment. This optimal situation consists of a polyhedral (cube with two attached triangles) and a board, which were both tracked. The polyhedral will be referred to as the cube. The cube fits tightly into 16 predefined positions on the board (Figure 4.1). A connection was designed on the cube to enable mounting of the optimal DRF as determined by the Monte Carlo analysis in Chapter 2 (Figure 4.1b). The cube and board were designed in SolidWorks with accurate dimensions and exactly known marker locations and 3D-printed at Oceanz (Oceanz, Ede, Netherlands), using the SLS printing technique.

The 3D models of cubes at the 16 tight-fitting positions in the board and the board itself were imported in Unity. The 16 virtual models of the cube at the correct

positions represented the planned position in the virtual world. The coordinates of the markers on both the cube and board, $\mathbf{p}_{UNITY}$, were used together with $\mathbf{p}_{tracker}$ to calculate the transformation ${}^{UNITY}\mathbf{T}_{tracker}$.

During tracking, the physical cube was positioned successively in the tracked board at the 16 planned positions. As the cube fitted tightly in the board at these locations, the physical cube was placed at the planned position (Figure 4.2). In the ideal situation with a perfect navigation system, this will position the virtual tracked object exactly at the planned location. In the real world, however, a discrepancy will arise due to imperfections of the setup. The magnitude of this discrepancy was calculated by subtracting the position and orientation of the tracked virtual cube from the position and orientation of the cube at the exact planned location. This error was a measure of the accuracy of the system.

For the evaluation of the trueness of the OON system, 10 measurements were performed for the cube at the 16 planned positions. Two rounds of measurements were performed, yielding a total of 320 measurements. The measurements were performed approximately 1 meter away from the tracker. The experiment will be further recognized as tight-fit, since the objects were placed in tight-fitting positions.

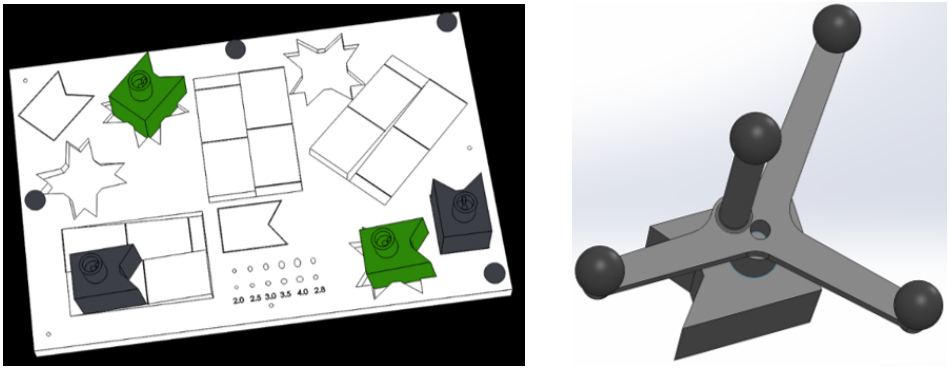

(a) Board with aligned cubes (b) Cube with DRF

Figure 4.1: 3D objects (board and cube) designed in SolidWorks for evaluating performance of the object-oriented navigation system. Dimensions of the board are 30 x 20 x 1 cm. The cubes with the attached triangles has outer dimensions of 4 x 3 x 3 cm. In SolidWorks, the cube was virtually aligned with specific locations on the board. In this figure, the cubes are shown at tight-fitting (green) and loose-fitting (gray) positions.

4.1.3 The loose-fit experiment

In addition to the tight-fit experiment, a loose-fit experiment was performed. The goal of the loose-fit experiment was to verify the accuracy of object placement including the error of manual (human) positioning of the cube on the board.

In this experiment, the cube was placed on 21 selected loose-fitting positions (Figure 4.1). Contrary to the tight-fit positions, the design of the board does not restrict movement of the cube at these locations. The cube was placed at the planned position relying on the information of the OON system displayed on the monitor, hence no visual or haptic feedback from the real world was used. The only restriction was that the cube had to be placed on the board, limiting freedom in the gravitational direction. The difference between the virtual tracked cube and the planned position was calculated as described in Section 4.1.2.

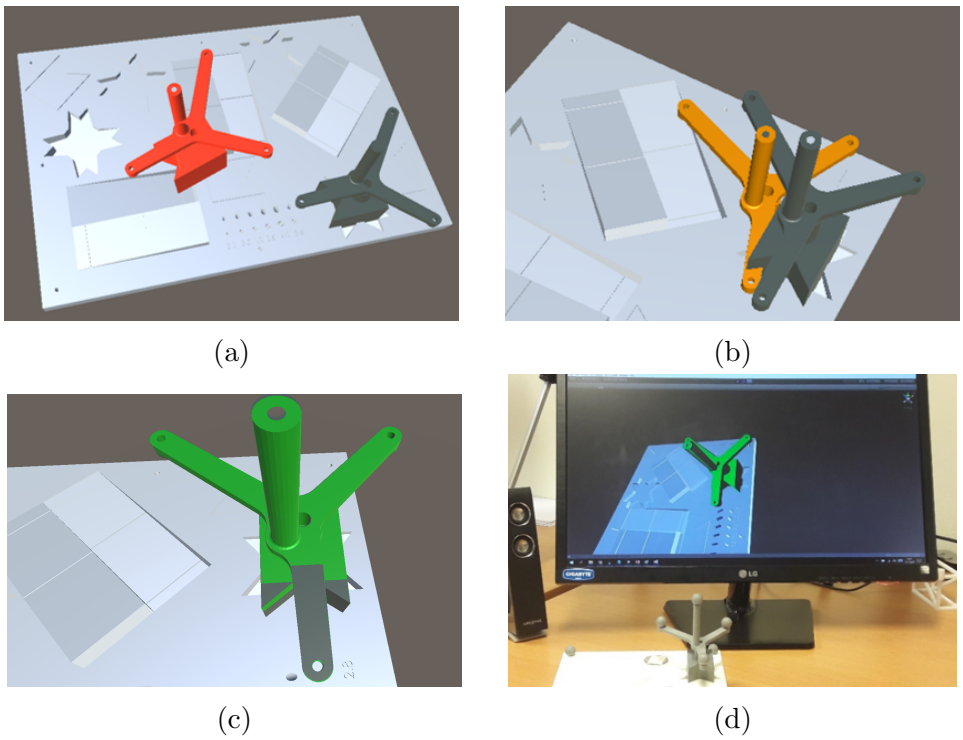

(a) (b)

(c) (d)

Figure 4.2: Example of Object-oriented navigation. The board and cube are tracked by the optical tracker using retroreflective markers. a-c) Unity environment with the virtual models of the board and cube. The gray cube represents the planned position (tight-fit) and moves along with the board. The tracked virtual cube is brought to the planned position and changes color as it moves to the planned position. d) Object-oriented navigation displayed on the monitor. The physical cube is positioned at the correct position, which is displayed by the green color of the virtual cube on the monitor.

Because human errors were evaluated in the current section, the measurements were performed by two different observers (2 rounds), observer 1 and observer 2. Both observers placed the cubes at the planned positions such that two rounds of measurements were performed, leading to a total 420 measurements. This experiment will be further recognized as loose-fitting, since the objects were placed with five degrees of freedom.

4.1.4 Statistical analysis

The deviations between tracked cube and the planned position were calculated for both experiments. To evaluate the difference between measurements of the two observers in the loose-fitting experiment, mean Euclidean distance for each position was reported. Using the same tests as in Chapter 3, it was evaluated whether measurements differed significantly. The Anderson-Darling test was used to evaluate the distribution and the paired t-test or the Wilcoxon signed rank tests were used to evaluate whether a difference between both rounds was significant [104–106].

4.2 Results

4.2.1 The tight-fit experiment

The results of the differences in rotation and position for the tight-fitting cubes in both rounds are reported in Table 4.1 and summarized in Appendix C (Figure C.7 and C.8). The results showed a maximal difference of 1 mm in the Euclidean distance. Mean deviations were 0.32, 0.38 and 0.21 mm for the x-, y- and z-direction, respectively and 0.6 mm for the Euclidean distance. Maximal deviation between the angles of tracked object and the planned object was 1.8°.

The mean Euclidean distances for the first and second round in this experiment were 0.61 mm (sd = 0.20) and 0.6 mm (sd = 0.12), respectively.

Table 4.1: Accuracy of object-oriented navigation. Absolute difference in position and rotation between tracked and planned cube in the tight-fit experiment.

	Mean error ± sd (mm)	**Max. error (mm)**
X-direction	0.32 ± 0.19	0.78
Y-direction	0.38 ± 0.22	0.84
Z-direction	0.21 ± 0.13	0.59
Euclidean distance	0.60 ± 0.16	0.98
	Mean error ± sd (deg)	**Max. error (deg)**
X-angle	0.64 ± 0.40	1.8
Y-angle	0.37 ± 0.31	1.2
Z-angle	0.61 ± 0.17	0.9

4.2.2 The loose-fit experiment

The results of placing objects at 21 loose-fitting positions using the object-oriented navigation environment are displayed in Table 4.2 and summarized in Appendix C (Figure C.9 and C.10). The results show a mean Euclidean distance between virtual tracked object and planned position of 0.70 mm (sd = 0.44). The maximal measured error was just below 2 mm (1.96 mm), the maximal angular deviation was 2.34°. The mean Euclidean distance for observer 1 was 0.71 mm and 0.68 mm for observer 2. The measured deviations did not show significant difference between both observers (p = 0.79).

4.3 Discussion

A newly developed object-oriented navigation system was explored in the present study. Object-oriented navigation techniques can be beneficial to the specialist in fracture reduction as the complex pelvic anatomy can be displayed in 3D. Compared to conventional 2D navigation, tracking and visualizing of 3D objects can potentially provide better monitoring in fracture reduction [21, 43, 75, 112, 113].

Table 4.2: Accuracy of object placement using OON. Absolute difference in position and rotation between tracked and planned cube in the loose-fit experiment.

	Mean error ± sd (mm)	**Max. error (mm)**
X-direction	0.34 ± 0.36	1.90
Y-direction	0.37 ± 0.27	1.18
Z-direction	0.34 ± 0.33	1.68
Euclidean distance	0.70 ± 0.44	1.96
	Mean error ± sd (deg)	**Max. error (deg)**
X-angle	0.36 ± 0.32	1.77
Y-angle	0.53 ± 0.41	2.34
Z-angle	0.40 ± 0.29	1.06

To realize OON for pelvic fracture reduction, a system was developed to track 3D objects. Tight and loose-fit experiments were performed to assess the accuracy of the system itself and the accuracy when it is used as guidance to place objects. The loose-fit experiment mimicked the use of OON to realize a preoperative plan in an optimal situation.

Tight-fit experiment

The result of the tight-fit experiment reported small deviations between position of the virtual tracked cube and the planned position when the cube was placed tightly in the board. The results proved that it was possible to bring two objects together according to a predefined plan with errors below 1 mm and a mean error of 0.60 mm.

The data of the first round in the tight-fit experiment was compared with the data of the second round. This enabled to assess the reproducibility of the object placement. The mean difference between the Euclidean distances of both rounds (0.60 and 0.61 mm) was small.

From the results it can be concluded that when an object is placed at the correct position, the navigation system will reproduce this position with a mean deviation of 0.60 mm. This information can be used to assume that when an object will be placed correctly according to the navigation system, the mean deviation from the actual planned position will also be approximately 0.60 mm.

Loose-fit experiment

The loose-fit experiment was performed to assess the usefulness of the OON system, as the system will be used to guide the user in placing two or more objects at a planned position. This experiment introduced a manual error of the user placing the cube using the virtually displayed content. Planned positions of the cube on the board and the tracked cube were virtually displayed and was used as the only guidance.

Even with the introduction of the human error, mean Euclidean distances between planned and tracked cube was 0.7 mm. This was only a small increase compared to the 0.6 mm measured in tight-fit experiment. Measured deviations did not differ significantly between two observers ($p = 0.79$). The results of the loose-fit experiment show that when the guidance of the OON system is used, objects can be placed at the correct position with high accuracy.

In the current study, the system was tested under optimal conditions. The only discrepancy between the virtual and the physical objects was the inaccuracy of the printing process. The manufacturer of the 3D-prints (Oceanz) verified that the deviation for a product of 150 mm was around 0.15 mm. This is in accordance with the accuracy described in literature, with accuracies ranging from 0.1 to 0.3 mm [114]. The objects were placed tightly at the deepened positions, making this error negligible.

In a clinical setting, however, 3D models will be generated using patient data introducing additional errors to the OON system. Errors will also be introduced by the detection of markers in the patient data. Therefore, to reach high accuracy in a clinical setting, high quality scans, good registration methods and correctly fixated DRFs are required.

The PST base tracker has been utilized before in a study under less optimal circumstances. The aim of that study was in vitro implant placement in dental models using image guidance. The position of the implants after placement was compared with a planned position, and mean deviations of 0.82 mm were found. Mean angular deviation of the implants was 1.67° [115]. These errors are slightly larger than the results found in the current study which can be explained by the fact that the burring introduced a larger human error and CBCT scans were incorporated in the study.

The discrepancy between the high accuracy found in this chapter and the low accuracy seen by comparing it with the milling machine raises questions. It was expected that the inaccuracy of the tracker in the z-direction influences the accuracy in the tight and loose-fit experiments. The high accuracy in this chapter can be explained by the fact that the board and cube were placed at approximately the same distance with respect to the tracker (in the same x-y plane of the tracker). This was necessary, as occlusion of markers occurred when the board was placed in the x-z or y-z plane. Another explanation for the high accuracy in these experiments is the high precision of the tracker as investigated in Chapter 3. Relative positions of objects close to each other can therefore be determined accurately. These considerations can explain the discrepancy between the errors in the experiment with the milling machine and the errors in the tight and loose-fit experiments.

At some positions of the cube on the board, occlusion of the retroreflective markers from the cube and / or board was seen on one or both of the camera images (Figure 4.3). This led to improper or interrupted tracking. To solve this, the board was rotated to eliminate the occlusion. The error introduced by occlusion was also reported by Gundle et al. [99]. For further development of the navigation system, it is wise to take the occlusion of markers into account. A possible solution can be to place DRFs with appropriate distance between each other or request the number of visible markers from the optical tracker during runtime. If the number is smaller than the used number of markers, the user must be warned such that the tracker position can be adjusted.

It can be concluded that the developed software platform can be used to accurately

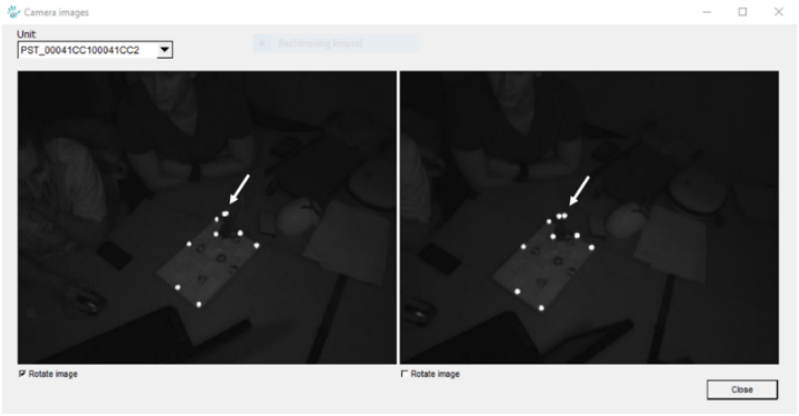

Figure 4.3: Occlusion of markers. Two markers mounted on the cube (white arrow) are occluded in the left image.

bring two objects to each other according to a predefined plan. Using the guidance on the monitor, objects were placed with a mean deviation of 0.7 mm from the planned position. The maximal error was below the required accuracy of 2 mm needed in pelvic fracture reduction, however, the system was tested under optimal conditions. The results are encouraging to use the OON system in preclinical situations mimicking the situation in pelvic fracture treatment. Using a more clinical setup, for example by the use of sawbone models, animal studies or human remains, the OON system can be further evaluated. After fracture reduction and fixation is realized in these models, the end result can be assessed by comparing the situation in the postoperative CT scan with the surgical plan. This will provide more information on the applicability of OON in pelvic fracture reduction.

Chapter 5

Object-oriented navigation using AR

Conventional image-guided surgery (IGS) uses a physical monitor to display the spatial information of tracked instruments in relation to the patient image data [79]. This display method diverts the focus of the surgeon from the surgical field to the monitor which can potentially cause dangerous situations. Furthermore, the necessary hand-eye coordination requires a steep learning curve [79]. In the ideal situation, both the patient and the information of the navigation system are merged. This removes the need for switching between the patient and the monitor, which can have a positive impact on the surgical results [116]. Embedding augmented reality (AR) in image-guided surgery can be the solution for the described problem [117]. Using AR the information of the navigation system can be projected on the patient. Several applications that combine AR and surgical navigation are described [71, 79, 81, 82, 118–120]. Differences in visualization, registration algorithms and projection methods for AR are reported to overcome a variety of clinical problems [47]. Different devices to achieve the projection include; virtual microscope, light field display, tablet display and video projectors [47]. However, head mounted devices (HMD) are most preferred since they render the virtual object with depth information [116].

Consequently, the use of HMDs is widely described for realization of a mixed reality setting for IGS [74, 78, 81, 101, 111, 121, 122]. A HMD allows the surgeon to move freely with respect to the patient and still see the information of the navigation system projected on the patient [81]. To determine the position of the user wearing the HMD with respect to the patient, the HMD must be tracked. Different methods are described to track the HMD, but optical trackers are generally used [47].

A promising HMD is the recently introduced Microsoft HoloLens as it combines several unique properties. First, the device renders high quality holograms in a stereoscopic way using optical see-through displays [123]. Second, the build-in processors facilitate the device to work untethered. Lastly, the device can be instructed by voice commands and hand gestures enabling the specialist to intuitively adjust, add or remove displayed information. This can solve the sterility problems present in controlling conventional navigation systems [124].

Since the device is released in 2016, only a few medical applications actually use the HoloLens. Hanna et al. used the HMD to correlate pathological images with corresponding MR or CT data [125]. Slices from the medical image data were projected over the resected tissue to determine the tumor location. Use of the HoloLens proved to be beneficial and reduced procedure time. Morley et al. and

Syed et al. used the HoloLens to render holograms of patient-specific anatomy and reported that this 3D technique is going to be extensively used in both therapeutic and diagnostic settings [83, 84]. To the best of the authors knowledge, literature does not describe the combination of the HoloLens and IGS.

On the contrary, the HoloLens has been designated as a potential device to combine IGS with augmented reality by several authors [126,127]. Literature states that from the current available HMDs, the HoloLens is the best choice for implementing AR in surgical interventions [128].

In the current study, the OON system was combined with the HoloLens to facilitate projection of the virtual objects on the optically tracked physical objects (mixed reality). This combination will provide a tool that can translate the preoperative surgical plan and the real-time data of the IGS system to the patient. The study in this chapter describes how the OON system is combined with the HoloLens to realize an optimal mixed reality setting. The accuracy of the OON in this AR setting and the performance of the overlay is assessed to answer the fourth sub-question: *What is the accuracy of object-oriented navigation in an augmented reality setting and what is the error in merging virtual and real objects?*

5.1 Methods and Materials

The HoloLens displays holograms with a frame rate of 60 Hz and is processed by the Microsoft Holographic Processing Unit (HPU 1.0) and an Intel 32 bit processor [123]. The 580 gram weighting device has a 64 GB Flash and 2 GB RAM memory. The battery life of the device is about 2.5 to 3 hours. Together with the high quality display of the holograms and handsfree controlling, spatial awareness using IR technology is implemented in the HoloLens.

To combine the OON system with AR, the Unity platform was used to develop and build applications on the HoloLens. The 'Holograpic Remoting Player' (HRP) application in Unity was used for the development of a HoloLens application. The HRP application enables to stream content from a PC to the HoloLens in real-time. During runtime, information from the OON system was transferred from the PC to the HoloLens and the 3D models were rendered on the device in 3D. However, since the HoloLens defines its own coordinate system, the virtual objects and the real objects tracked in the coordinate system of the tracker were positioned at different locations. Hence, a method was used to link both coordinate systems.

5.1.1 Linking coordinate systems of tracker and HoloLens

To determine the relation between the optical tracker and the HoloLens, the HoloLens had to be tracked by the optical tracker. Therefore, a frame was designed that fits on the HoloLens and enables mounting of DRFs with retroreflective markers (Figure 5.1). This frame was optically tracked to define the location of the HoloLens in the coordinate system of the optical tracker.

To combine the OON system with AR, two different coordinate systems needed to be into spatial alignment, the *trackers'* and *HoloLens'* coordinate system. This was realized by finding ${}^{HoloLens}\mathbf{T}_{tracker}$, the transformation from the *trackers'* to the *HoloLens'* coordinate system. To realize this, two transformations were calculated by making use of an additional intermediate coordinate system, the *frames'* coordinate system (Figure 5.2a). The first transformation was realized by a built-in

function in the API of the tracker, calculating ${}^{frame}\mathbf{T}_{tracker}$ using the spatial relation of the frame in the *trackers'* coordinate system. This coordinate system has the same origin and orientation as the tracked frame object. ${}^{frame}\mathbf{T}_{tracker}$ was applied to the tracked objects to express them in the *frames'* coordinate system (Figure 5.2b,c).

The second transformation corrected for the discrepancy in spatial relation between the frame and the HoloLens. This transformation from the *frames'* coordinate system to the *HoloLens'* coordinate system, ${}^{HoloLens}\mathbf{T}_{frame}$, was determined by interactively finding the best overlay of the virtual objects with the physical objects. This transformation was applied to all tracked objects, which are then expressed in the *HoloLens'* coordinate system (Figure 5.2d).

In this way, the two transformations were applied to the tracked objects. This resulted in the same transformation compared to applying the single transformation, ${}^{HoloLens}\mathbf{T}_{tracker}$, because:

$$ {}^{HoloLens}\mathbf{T}_{tracker} = {}^{HoloLens}\mathbf{T}_{frame} \; {}^{frame}\mathbf{T}_{tracker} \tag{5.1} $$

Since the frame was attached to the HoloLens, finding the optimal overlay of the virtual and physical objects manually can be applied once. The transformation, ${}^{frame}\mathbf{T}_{tracker}$, was dynamic and was therefore updated every frame.

Figure 5.1: The frame used to track the HoloLens. Using the retroreflective markers attached to the frame, the position of the HoloLens was tracked by the optical tracker.

5.1.2 The tight-fit experiment in the AR setting

To evaluate the accuracy of the OON system in an augmented reality setting, the experiment described in Section 4.1.2 was repeated. The only modification in this experiment was that the OON system was combined with the HoloLens as described in Section 5.1.1 The cube was placed in the board at the 16 specified tight-fitting locations and the difference between the tracked virtual cube and the planned position was determined. A total of 320 measurements were performed, distributed over two rounds of measurements.

5.1.3 The loose-fit experiment in the AR setting

An experiment comparable to the one described in Section 4.1.3 was performed to test the accuracy of object placement at the 21 planned loose-fitting positions. However, in this experiment the user relied only on the information displayed by the HoloLens. Both the board and cube were tracked using the OON system, but only a hologram of the cube at the planned position with respect to the board was rendered

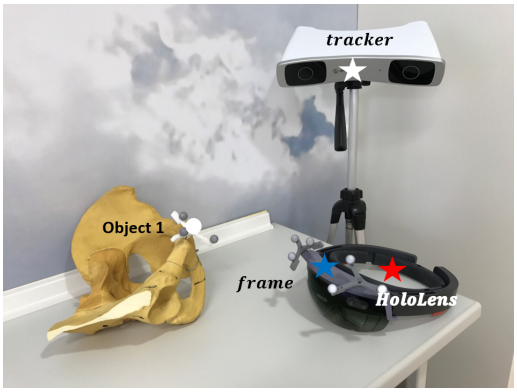

(a) Coordinate systems of the tracker (white), frame (blue) and HoloLens (red).

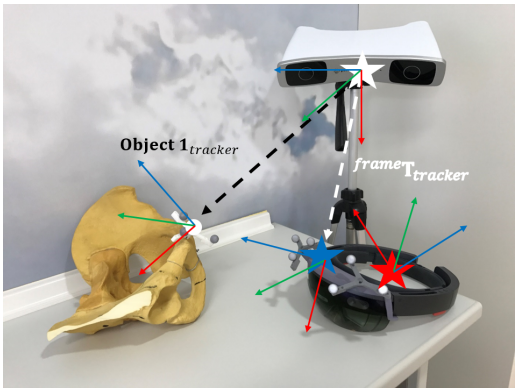

(b) Object 1 is expressed in the *trackers'* coordinate system (black arrow). The transformation, ${}^{frame}\mathbf{T}_{tracker}$ (white arrow) is calculated using the spatial relation of the tracked frame.

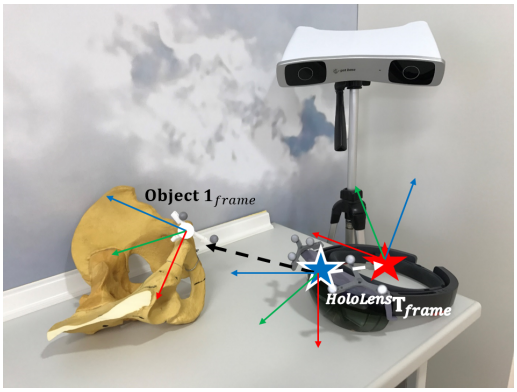

(c) Transformation ${}^{frame}\mathbf{T}_{tracker}$ is applied to object 1 (black arrow), which is now expressed in the *frames'* coordinate system. ${}^{HoloLens}\mathbf{T}_{frame}$, transforms objects from *frames'* to *HoloLens'* coordinate system (white arrow).

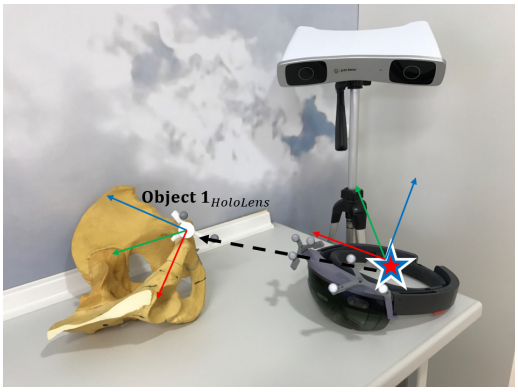

(d) Transformation ${}^{HoloLens}\mathbf{T}_{frame}$ (obtained by manually overlaying virtual with physical object) is applied to object 1, which is now expressed in the *trackers'* coordinate system (black arrow).

Figure 5.2: Transformation of objects between coordinate systems.

by the HoloLens. The task was to place the real cube at the planned loose-fitting position displayed by the hologram (Figure 5.3). Visual and haptic feedback were limited, as described in Section 4.1.3. The spatial difference between the virtual planned and the tracked cube was calculated to determine the accuracy of object placement using augmented reality.

This experiment evaluated the inaccuracy introduced by the user to place the object at the planned position. Therefore, the experiment was repeated two times (two rounds) by two different observers, observer 1 and observer 2. The Euclidean distances between tracked cube and its planned position for both observers were calculated and compared.

5.1.4 Statistical analysis

The results were analyzed using the methods described in Section 4.1.2 and 4.1.3. Furthermore, the difference in accuracy between OON with and without augmented reality was evaluated by comparing the data with the results from Chapter 4. It was

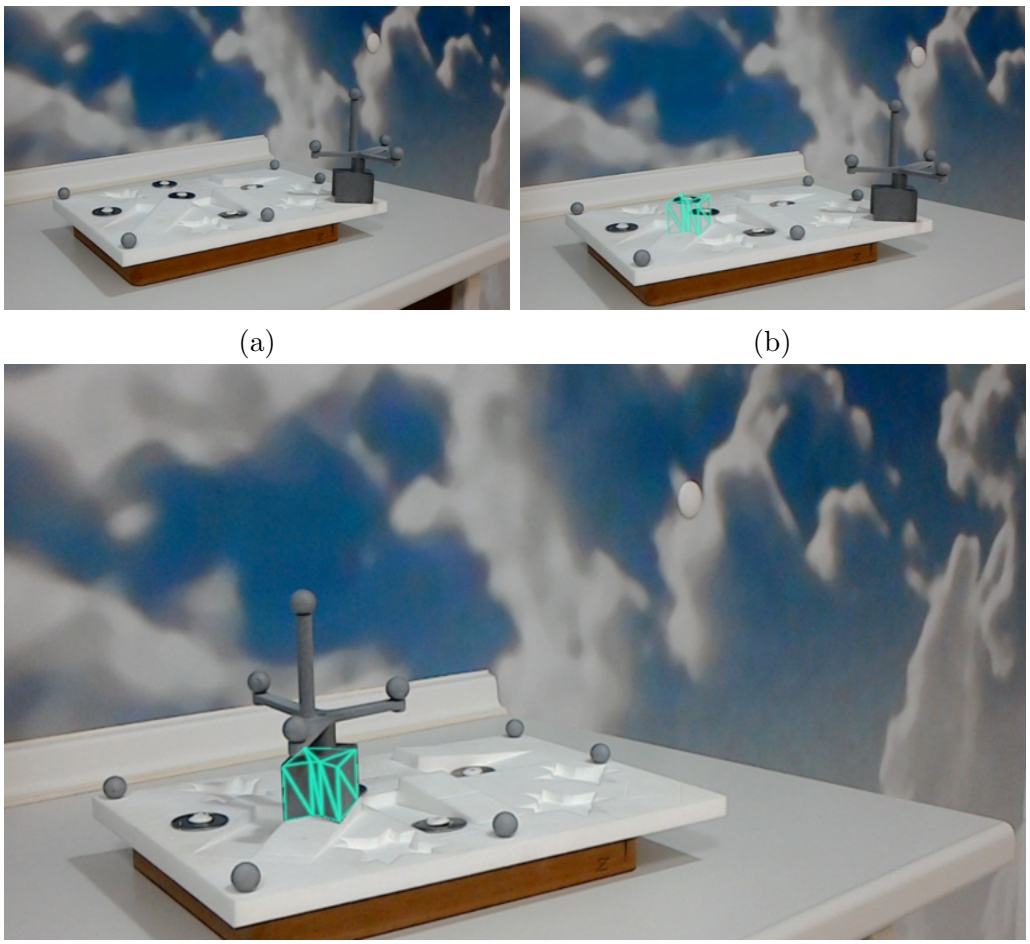

(a) (b)

(c)

Figure 5.3: Object-oriented navigation in the augmented reality setting used as guidance to place objects. a) Tracked board and tracked cube. b) The planned position of a cube is displayed by a hologram of the mesh of the cube (green outline). c) The cube is placed at the planned position by merging the virtual and physical object using the displayed hologram .

tested whether the differences between the measurements in the loose- and tight-fitting experiments were significant by comparing the averaged Euclidean distance for each measured location, using the tests described in Chapter 3.

5.2 Results

5.2.1 The tight-fit experiment in the AR setting

The difference between position and orientation of the tracked virtual cube and the planned position in the 16 tight-fitting positions for both rounds are summarized in Appendix C (Figure C.11 and C.12). The relevant mean and maximal values are reported in Table 5.1. The mean Euclidean distance was 0.71 mm (sd = 0.24), with a maximal error of 1.40 mm. Maximal rotational error was 2.5°. Comparison of the results for the two different rounds showed comparable mean Euclidean distances (0.63 mm (sd = 0.17) and 0.79 mm (sd = 0.27), respectively).

Table 5.1: Accuracy of OON in the AR setting. Absolute difference in position and rotation between tracked and planned cube in the tight-fit experiment.

	Mean error ± sd (mm)	**Max. error (mm)**
X-direction	0.31 ± 0.24	1.02
Y-direction	0.46 ± 0.25	1.15
Z-direction	0.33 ± 0.18	0.79
Euclidean distance	0.71 ± 0.24	1.40
	Mean error ± sd (deg)	**Max. error (deg)**
X-angle	0.48 ± 0.35	1.8
Y-angle	0.62 ± 0.56	2.5
Z-angle	0.64 ± 0.33	1.5

5.2.2 The loose-fit experiment in the AR setting

The results for object placement in the loose-fitting experiment using the guidance from the HoloLens are summarized in Appendix C (Figure C.13 and C.14). The relevant deviations are reported in Table 5.2. The mean Euclidean distance between the position of the tracked cube and the planned position was 1.81 mm (sd = 0.68). The maximal positional and angular deviation was 3.94 mm and 2.82°.

Comparing the data of both observers, an overall mean Euclidean distance of 1.79 mm for observer 1 and 1.83 mm for observer 2 was seen. There was no significant difference for object placement between both observers proven by the Wilcoxon signed rank tests (p = 0.54).

Table 5.2: Accuracy of object placement using OON in the AR setting. Absolute difference in position and rotation between tracked and planned cube in the loose-fit experiment.

	Mean error ± sd (mm)	**Max. error (mm)**
X-direction	0.84 ± 0.68	2.89
Y-direction	0.88 ± 0.29	1.66
Z-direction	1.08 ± 0.74	3.44
Euclidean distance	1.81 ± 0.68	3.94
	Mean error ± sd (deg)	**Max. error (deg)**
X-angle	0.42 ± 0.30	1.26
Y-angle	0.77 ± 0.63	2.30
Z-angle	1.08 ± 0.64	2.82

5.2.3 Comparison of results between experiments with and without AR

The overall mean deviation between tracked cube and the planned position reported in the tight-fit experiment without AR was 0.60 mm (Table 4.1), whereas the average difference in the experiment with AR was 0.71 mm (Table 5.1). The average Euclidean distance for all measured positions in both experiments were not significantly different, proven with the Wilcoxon signed rank test ($p = 0.10$).

This comparison was repeated for the loose-fit experiments. Mean Euclidean distance in placing objects using the OON system without AR was 0.70 mm (Table 4.2), whereas the use of OON with AR resulted in a mean Euclidean distance of 1.81 mm (Table 5.2). The difference was tested to be significantly different using the Wilcoxon signed rank test ($p < 0.001$). This showed that objects were placed significantly better in a setting without AR.

5.3 Discussion

Correct implementation of augmented reality in image guided surgery can improve the guidance as it enables the user to keep focus on the surgical setting [116]. In the current study, an OON system was combined with the HoloLens to create a fundamental basis for this implementation. The combination with the HoloLens realized guidance using OON in a mixed reality setting. The developed system combined the high accuracy of the OON system with the advantage of the 3D models being projected on the patient. The use of the HoloLens enabled a high quality rendering by see-through displays and allowed intuitive sterile controlling. The only addition for using the device in combination with OON was the use of a frame. These advantages makes the HoloLens superior to the HMDs described in other applications [45, 47, 74, 79, 122, 128, 129].

The tight-fit experiment

The results showed that when an object was placed according to the plan in the tight-fit experiment, the navigation system reported a mean deviation of 0.71 mm. The results of the experiment in the AR setting showed an increase in error of 0.11 mm (from 0.6 to 0.71 mm (Table 4.1 and 5.1)) compared to the experiment without AR.

This result showed that the navigation system was still able to accurately detect the spatial relation of two objects when the OON system was combined with the HoloLens. This is important since this spatial information was not used in this evaluation but can be easily incorporated as additional guidance. In the next chapter, this is realized by using a color indication based on the calculated difference between measured position and planned position. This additional information can improve the guidance. As described in Chapter 4, the setup was under ideal circumstances and it is thus expected that the clinical application error will increase due to introduction of new errors.

The loose-fit experiment

In the loose-fit experiment, the guidance using the HoloLens resulted in deviations up to 4 mm, with a mean Euclidean distance of 1.81 mm between actual and planned

position (Table 5.2).

These errors were significantly higher compared to the loose-fit experiment without the use augmented reality. This result was expected, as the calculated misplacement was an addition of different errors which were not present in the situation without AR.

The first error in the experiments with the guidance using AR is introduced by finding the optimal overlay of virtual and physical objects to determine ${}^{HoloLens}\mathbf{T}_{frame}$. Secondly, an error was introduced by the occlusion of markers as described in Chapter 4. A third error was introduced by jitter of the hologram adding up to the overall error. Lastly, the large inaccuracy (8.9 mm over a distance of 50 cm) in the z-direction of the tracker can influence the results. The distance between the frame on the HoloLens and the board and cube was at least 20 cm. The inaccuracy of the tracker can cause the holograms to be positioned incorrectly, impeding the accuracy of the loose-fit experiment.

By improving the OON system combined with AR, the influence of the errors can be reduced. To improve the system, it must be investigated whether more dedicated techniques can be implemented to find ${}^{HoloLens}\mathbf{T}_{frame}$. One possible method is the use of stereo camera calibration at the start of a session [91]. By capturing a checkerboard with the available camera in the HoloLens and the cameras in the optical tracker, a transformation between both devices can be calculated. Another possible method is the single point active alignment method [130]. This method correlates coordinate systems by aligning a cursor in the HMD with a point in the real world. This is repeated for a certain number of points at locations which are known in the coordinate system of the tracker. This information is sufficient to align the coordinate system of the tracker with the HMD [130].

The jitter of the holograms was introduced by the fact that the application ran using the HRP application. This disabled the dedicated motion filtering which is a key feature in the HoloLens. The problem will be solved when the application is run from the HoloLens itself. This will activate the motion filtering and lead to a stabilization of the holograms, improving the quality of the 3D rendering. The improvement can be realized by directly streaming the data of the tracker to the HoloLens.

The solutions for solving the marker occlusion problems were addressed in Chapter 4. The inaccuracy in the z-direction and the potential solutions has been discussed in Chapter 3.

Another optimization can be realized by improving the visualization of the holograms. In the OON system, the HoloLens displayed the wireframe of the virtual cube. Literature describes different visualization methods for the 3D objects, and it must be evaluated whether other display methods result in better performance [47].

Although the AR visualization can be improved, the mean error of 1.81 mm found for the placement of objects is proven to be similar to errors found in literature. Projection errors of the augmented data were reported ranging from 0.8 to 5 mm [71, 81, 82, 129, 131].

It can be concluded that the presented method for OON in an augmented reality setting can produce accurate results (mean error = 0.71 mm). The accuracy of the system did not show a significant difference between a setup with or without AR. However, object placement using AR guidance showed a significantly reduction in performance compared to OON without using AR. Errors up to 4 mm were seen, making the current guidance unusable in clinical practice. On the contrary, an

advantage of the AR implementation was that the hand-eye coordination was not impaired, which is the main reason a mixed reality setting is desired.

As the accuracy of the system was below the clinical relevant accuracy, the guidance using the holograms should be improved before the step to a preclinical setting can be made.

Chapter 6

Embedding OON in the clinical workflow

In the previous chapters, the design and the performance of the OON system is described. To implement object-oriented navigation (OON) in clinical practice, changes to the current clinical workflow are required. For a safe implementation of the developed system, different simulations and tests should be performed. In this chapter, a possible workflow is described to prove that it is technically possible to use the developed OON system in clinical-like situations. A sawbone model was used to simulate a patient and a preoperative surgical plan was translated to the sawbone model. An overview of the proposed clinical workflow is summarized in Figure 6.1.

In this chapter, an overview is given to indicate what tools are already available in the *current* clinical setting or in literature. Furthermore, it is explored which additional steps are *proposed* to bring OON into clinical practice. The steps are supported with a *simulation* using a sawbone model of the pelvic ring.

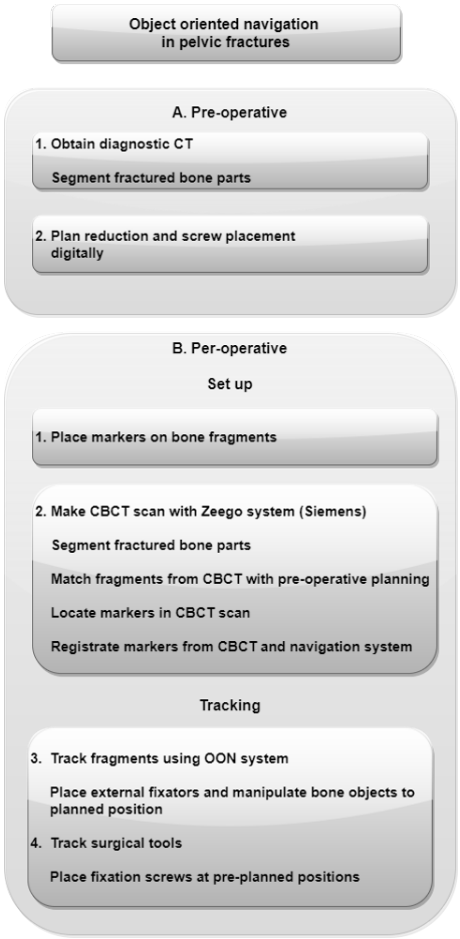

Figure 6.1: Overview of the *proposed* clinical workflow for pelvic fracture reduction using object-oriented navigation.

6.1 Preoperative workflow

In the *current* workflow at Radboudumc, a diagnostic CT scan is acquired in patient with a suspected pelvic fracture. This scan is used to evaluate the fracture pattern and determine the treatment.

In the *simulation* with the pelvic sawbone model, a Duverney type fracture was created by sawing the left iliac wing of the model (Figure 6.2) [132]. The model was then scanned using the Siemens Artis Q ZeeGo CT scan (Siemens Healthcare GmbH, Erlangen, Germany), available at the high-tech

operation room (OR) at Radboudumc (Figure 6.3). This cone-beam CT (CBCT) scanner has a high-end robot-assisted positioning capability. The obtained scan imitated the diagnostic scan acquired in the *current* workflow.

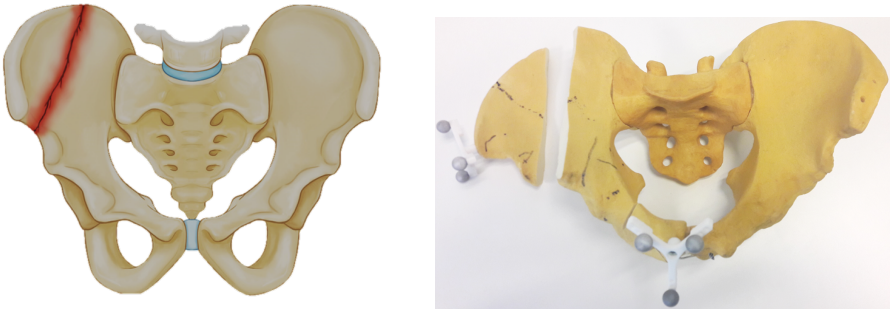

(a) (b)

Figure 6.2: a) Duverney fracture of the iliac wing [133] b) Duverney fracture in the sawbone model, after placement of DRFs on the right iliac wing and right pubic tubercle.

In the *proposed* clinical workflow a virtual plan is required. Different methods for virtual reduction are described in literature, however, the optimal method varies between fracture types [15, 34, 36, 40–42].

To achieve a virtual plan in the *simulation* with the sawbone model, a CBCT scan of the full, nonpathologic sawbone model was obtained. The reconstruction from the 'prefracture' CBCT scan served as a template for the preoperative plan.

The virtual plan was created by placing the 3D reconstructions of the separate fragments in the diagnostic CBCT scan over the template. This was realized by using a surface based matching method: the iterative closest point (ICP) algorithm [134]. First an initial rough alignment of two different 3D models was required. Second, this alignment was refined by the ICP algorithm, which finds the transformation with the smallest distance between points in both models. This transformation, ${}^{UNITY}\mathbf{T}_{Diagnostic\ CBCT}$, transformed the 3D model of the diagnostic scan to the planned situation (in the Unity coordinate system). The reconstruction of the 3D models and the registration were performed using Maxilim (Medicim NV, Mechelen, Belgium). The obtained preoperative plan was used as a guide to achieve an anatomical reduction (Figure 6.4).

Figure 6.3: The Siemens Artis Q ZeeGo CBCT scanner at the Radboudumc scanning the pelvic sawbone model after placement of DRFs.

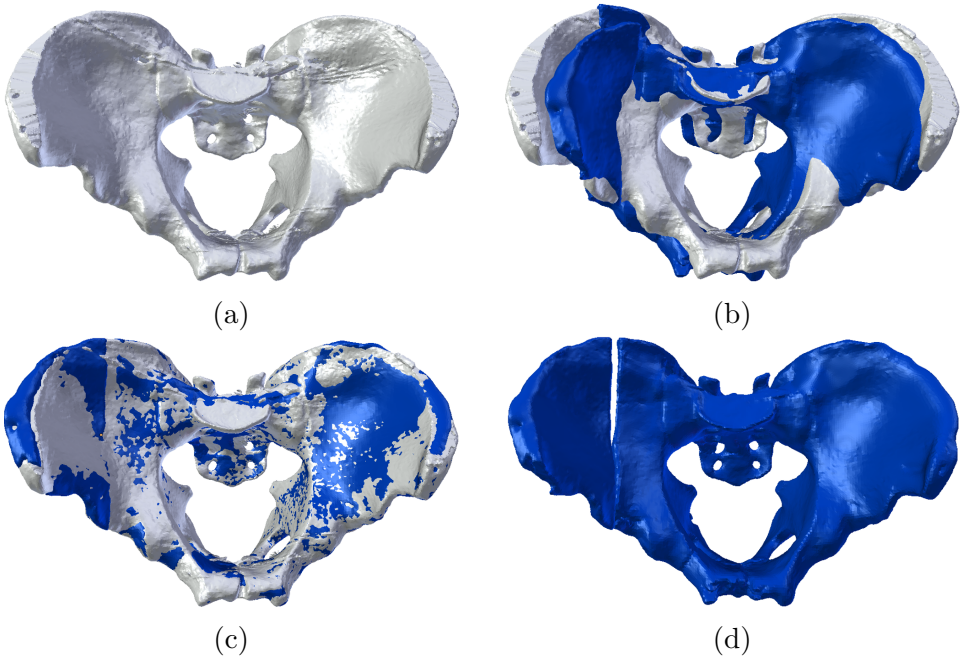

Figure 6.4: Surface based matching for the preoperative surgical plan. a) 3D reconstruction of nonpathological pelvic ring from the prefracture CBCT scan. b) Reconstruction of pathological situation (blue) in coordinate system of nonpathological situation (white). Note the misalignment of the objects. c) Fragments in pathological situation matched on nonpathological reconstruction after applying surface-based matching. d) Result of virtual surgical plan in a Duverney fracture.

6.2 Intraoperative workflow

In the *proposed* clinical workflow, a small incision is required to fixate the reference frames (DRF) for each fragment. This procedure should be realized at the OR with the patient in a sedated condition. The dynamic DRF must be positioned rigidly and may not hinder the surgeon. Therefore, the best positions for placement are on the pubic bone, iliac crest or sacral region since here the bone is superficial [135]. The actual optimal DRF position depends on the fracture type, number of fragments and location of fragments. Furthermore, the markers have to be visible for the optical tracker. Caution must be used when fixating the DRFs, because small positional or rotational changes will introduce errors [135]. The fixation of the DRFs is also necessary in the *current* procedure for conventional navigation and will therefore not lead to difficulties for implementation [43, 75, 113].

In the *proposed* clinical workflow, a CBCT scan must be reconstructed intraoperatively to relate the position of the markers with respect to the fragments after placement of the DRFs. In the *simulation* with the sawbone model, a DRF was mounted on both fragments of the sawbone model. The DRFs were placed on the anterior superior iliac spine of the iliac wing fragment and on the ipsilateral pubic tubercle (Figure 6.2). An 'intraoperative' CBCT scan was created using the ZeeGo scanner with the DRFs mounted on both fragments. This CBCT scan is an addition to the *current* protocol and might be regarded as replacement for the fluoroscopic images that are needed to register the patient in conventional navigation.

To enable OON, the data from the intraoperative CBCT scan must be processed using four steps:

1. Segmentation and 3D-reconstruction of fragments

2. Transformation of fragments from intraoperative scan to preoperative plan

3. Detection of marker locations in intraoperative scan

4. Registration of markers from intraoperative scan and markers from tracking system

Both the CBCT scan and the processing of this scan are additional to the *current* protocol, however, the ZeeGo scanner and the tools for processing are available.

Segmentation and 3D-reconstruction of fractured fragments

The bone fragments in the CBCT scan must be reconstructed to obtain virtual 3D models of the fragments. The Digital Imaging and Communications in Medicine (DICOM) data must be exported to a software platform which can realize this segmentation. An adequate software program and a dedicated processor is required for this intraoperative processing since this segmentation needs to be fast.

Transformation of fragments from intraoperative scan to preoperative plan

The next crucial step in the *proposed* clinical workflow is registering every single fragment in the CBCT scan with the corresponding fragment in the preoperative plan. A possible method to achieve this registration is the surface based matching method, described in Figure 6.4.

Using this method, the transformation for each fragment from the intraoperative CBCT to the diagnostic CBCT, ${}^{Diagnostic\ CBCT}\mathbf{T}_{Introperative\ CBCT}$, must be calculated. With this transformation and ${}^{UNITY}\mathbf{T}_{Diagnostic\ CBCT}$, the separate objects must be transformed to the planned position. The transformed 3D objects must be loaded into Unity.

In the *simulation* with the sawbone model, the 3D reconstructed models of the fragments in the 'intraoperative' CBCT were matched on the 'diagnostic' CBCT using the same method as described in Figure 6.4.

Detection of marker locations in intraoperative scan

Markers in the CBCT scan must be correlated with markers in the navigation system to register the patient with the navigation system. To detect the spheres in the intraoperative CBCT scan, the spherical Hough transform algorithm, made available in Matlab by Xie [136] can be used. By adjusting parameters such as diameter of the spheres, concentricity and Hounsfield units, the center of the spherical markers can be calculated automatically (Figure 6.5). The position of the spheres in the set can be conversed to metric coordinates, $\mathbf{p}_{intraoperative\ CBCT}$, using the geometrical data that is incorporated in the DICOM information.

The Hough transform algorithm was used to determine the location of the markers in the 'intraoperative' CBCT scan of the pelvic sawbone model.

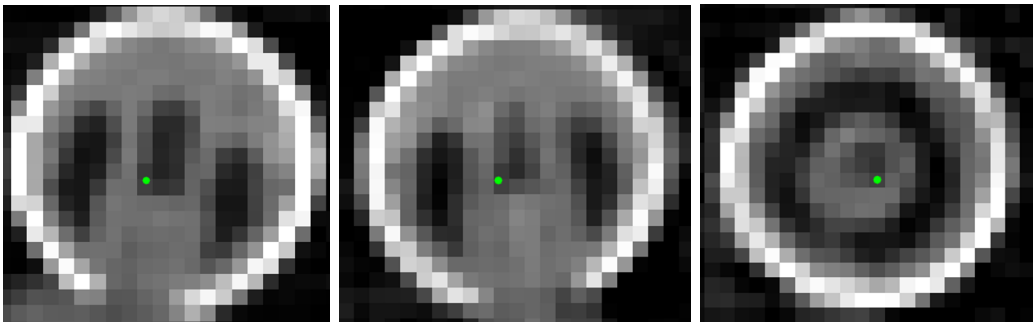

(a) (b) (c)

Figure 6.5: Sphere detection using the spherical Hough transform algorithm. The green dot represents the center of a retroreflective marker with a radius of 7.5 mm. a) Sagittal CBCT slice b) Coronal CBCT slice c) Axial CBCT slice.

Registration of markers in the intraoperative scan and markers from the tracking system

In the *proposed* clinical workflow, the markers detected in the intraoperative CBCT scan must be transformed to the preoperative plan. This transformation can be realized by using ${}^{UNITY}\mathbf{T}_{Diagnostic\ CBCT}$ and ${}^{Diagnostic\ CBCT}\mathbf{T}_{Intraoperative\ CBCT}$. The transformed coordinates, $\mathbf{p}_{UNITY}$, correspond with the markers in the 3D models at the planned position in Unity. $\mathbf{p}_{tracker}$, the corresponding trained coordinates from the navigation system and $\mathbf{p}_{UNITY}$ have to be imported in Unity to calculate ${}^{UNITY}\mathbf{T}_{tracker}$ (Section 4.1.1). This transformation must be used to transform the imported 3D models correctly into the navigation environment. If these steps are realized for all fragments, the models are correctly aligned in the same coordinate system. In this way, the planned position and the actual position are incorporated in the OON system and the system can guide the specialist during surgery.

These steps were realized in the *simulation* with the sawbone model. An example of the transformation of the preoperatively planned 3D models in Unity is visualized in Figure 6.6.

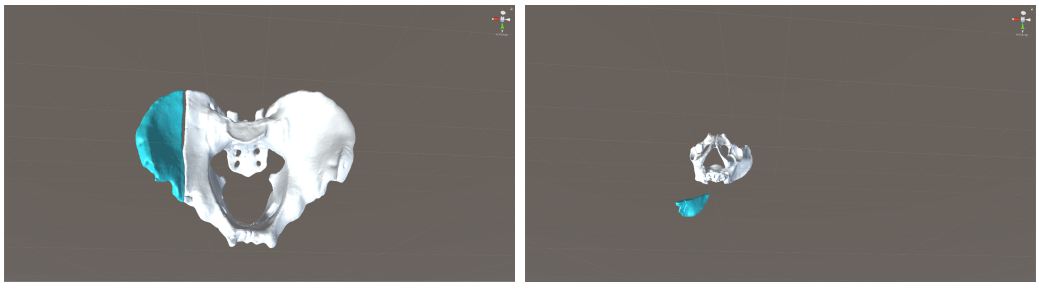

(a) (b)

Figure 6.6: Transformation of objects in Unity using ${}^{UNITY}\mathbf{T}_{tracker}$. a) Unity environment with the position of the fragments according to the preoperative plan. b) ${}^{UNITY}\mathbf{T}_{tracker}$ was calculated for each object and applied to the 3D models in the Unity scene.

6.3 Object-oriented navigation

In the *proposed* clinical workflow, the use of OON can be applied in two different approaches; the minimal invasive approach and the open reduction. For the minimal invasive pathway, the surgeon can insert external fixation pins in the bone. These pins provide the specialist with tools for manipulating the separate fragments. The navigation system provides the surgeon with the necessary information.

In the case of open reduction, the specialist can create the surgical entry windows and clear out the debris at the fracture site. In this situation, the navigation will act as guidance, giving additional information about the quality of the reduction of the fracture.

In the *simulation* with the pelvic sawbone model, a setting with and without the HoloLens was created. The reduction could therefore be seen by watching the monitor or through the HMD (Figure 6.7 and 6.8). By bringing the tracked iliac wing fragment to the pelvic ring, the virtual 3D models were closing in on each other (Figure 6.7).

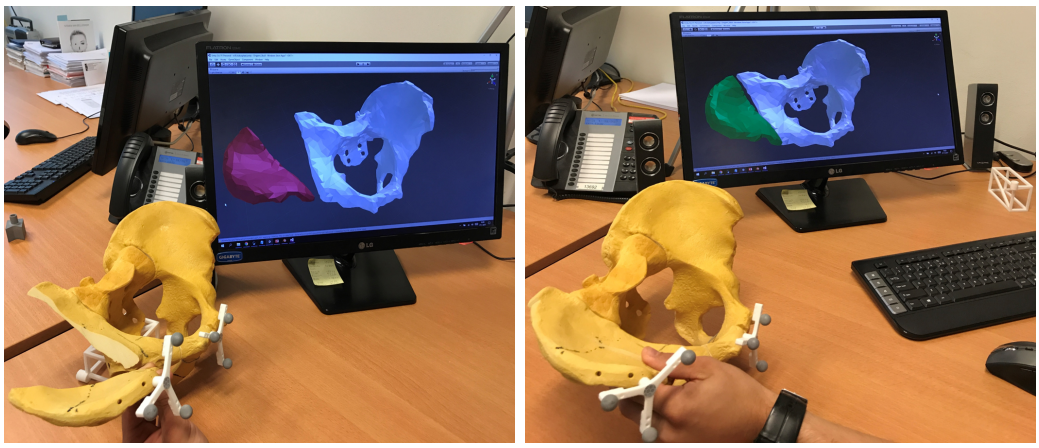

(a) (b)

Figure 6.7: The use of object-oriented navigation for reducing a pelvic fracture simulated in a sawbone model. a) Both the pelvic ring and the iliac wing are tracked by the optical tracker. Distance between the actual location of the wing and the planned location is large (red). b) The iliac wing is correctly repositioned according to the preoperative plan. Hence, the color of the iliac wing is green.

As the virtual models were merged with the physical objects, a mixed reality setting was created (Figure 6.8). This implies that when the view of the user on the real sawbone model was obstructed, the virtual 3D model was still visible. This situation mimicked the setting in closed reduction, where the real objects are also obstructed by the skin. Using the information seen through the HMD, the results of the manipulation using the external fixation pins can be monitored.

6.4 Discussion

The simulation of the clinical workflow using the sawbone model proves that it is technically possible to implement OON in the clinical practice. Different methods can be used in the workflow and it has to be investigated which method provides

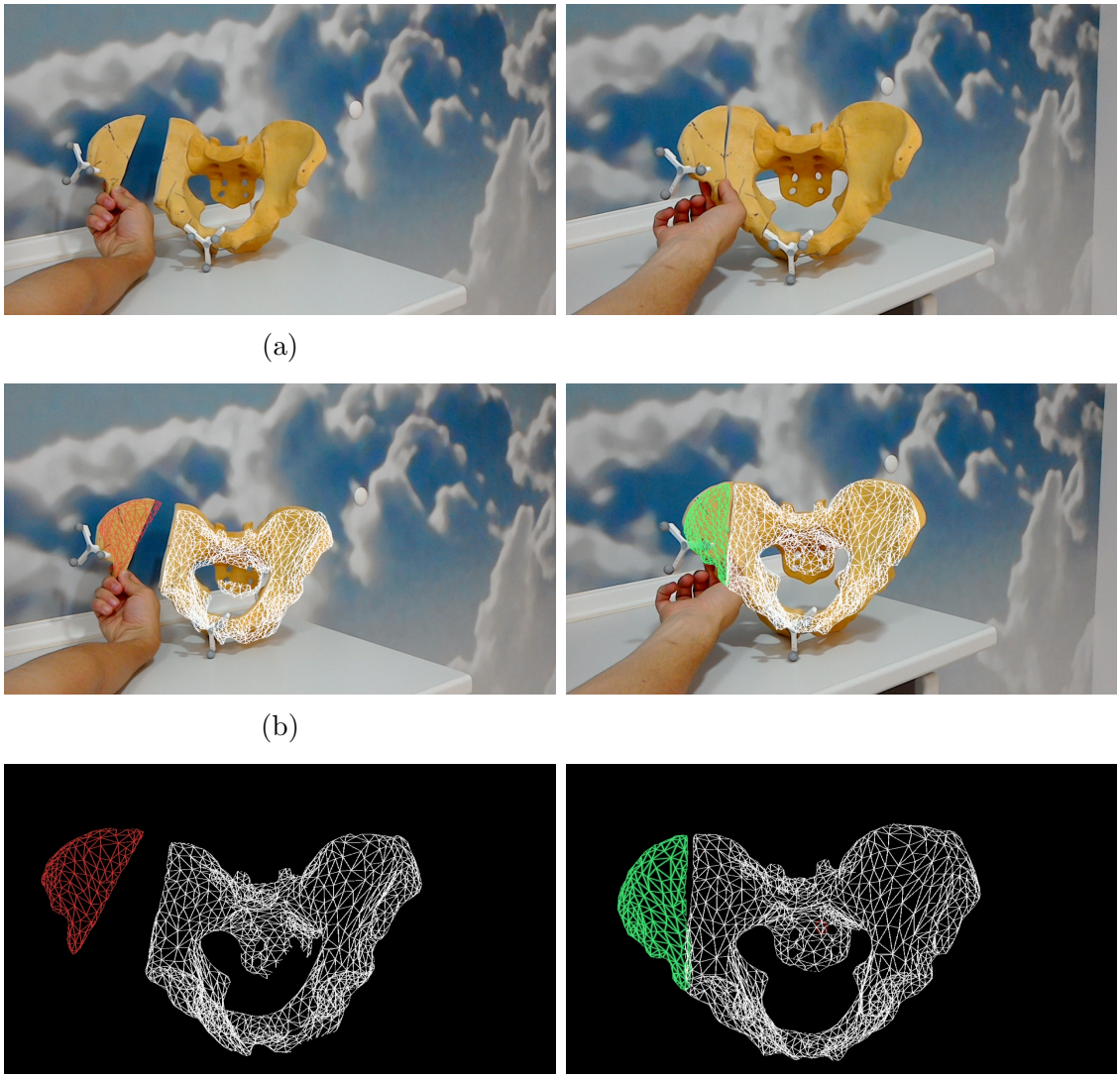

Figure 6.8: The use of object-oriented navigation combined with mixed reality for reducing a pelvic fracture simulated in a sawbone model. a) Displaced tracked iliac wing and pelvic ring were repositioned according to a preoperative plan. b) The virtual models were merged with the physical sawbone models, creating a mixed reality setting. As the fragments enclosed each other, the mesh turns from red green. The green color indicated that a reduction according to the preoperative plan was realized. c) If the view of the user was obstructed, the mesh was still visible. This proves that the surgeon can monitor the relation of the fragments without having direct vision on the physical fragments.

the best results and is applicable in clinical practice. OON in an augmented reality setting is a new field in image guided surgery and can improve the guidance in clinical applications [78, 80]. Implementation of OON combined with AR makes it possible to translate the virtual preoperatively plan to the patient. Furthermore, it gives a better 3D perception of the patients anatomy and enables to visualize the reduction in minimal invasive surgery.

Therefore, the potential use of an accurate and intuitive OON system can have a significant impact on health care. It improves the ergonomics for the surgeon, enables the surgeon to assess his work during surgery and makes it possible to improve surgical outcome. The main advantage of introducing OON in an augmented reality setting is the fact that unstable, displaced fractures can probably be repositioned in a minimal invasive way. This will possibly result in less blood loss, smaller wounds, less iatrogenic damage and shorter hospital stay [20]. Eventually this results in a reduction of the health care costs [137]. All these advantages show that correct implementation of OON is a solution to a clinical relevant problem.

However, it must be further investigated whether a sufficient reduction can be achieved by manipulation using external fixation pins alone. Necrotic material, periosteum or muscle might pervade the cavity between two fragments, troubling the manipulation. Muscles attached to the pelvis might further impede movement. On the contrary, a minimal invasive method potentially reduces blood loss. This will shorten the recovery time needed between trauma and surgery, enabling early intervention [19, 138]. An early intervention will improve reduction, since fragments are more mobile in the first five days after trauma as less tissue fibrosis is formed [139].

In the *simulation* with the sawbone model, metal artifacts in the CBCT scan led to an impaired reconstruction [140]. In the image data, scattering caused streak artifacts around the screws used to mount the DRF (Figure 6.9). These artifacts can be prevented by using carbon screws for fixation of the DRF. De Jong et al. proved that carbon-fiber-reinforced poly-ether-ether-ketone (CFR-PEEK) screws can be safely used for surgery and that this material reduces the streak artifacts seen with metal screws [141, 142].

The *proposed* procedure requires an additional intraoperative CBCT scan, increasing the radiation burden to the patient. However, if the use of OON is robust and leads to the preoperatively planned situation, it will reduce the needed of fluoroscopic images and the postoperative CT scan [75]. This will result in a reduced radiation dose for the patient [75]. Furthermore, it has been investigated that the use of a CBCT scan can reduce radiation harm to the specialist compared to using fluoroscopic images [109].

In the *simulation* with the pelvic sawbone model, a discrepancy of around 3 mm between the virtual models and the real sawbone model was seen. This was introduced by several factors already mentioned in Chapter 5. On top of this, the used registration and reconstructions of CBCT data introduced additional errors. The performance of the system, as well as the registration and calibration can be optimized to achieve a better overlay of virtual and real objects.

In conclusion, OON applied to the pelvic sawbone model proved that it is technically possible to implement OON navigation in an augmented reality setting in clinical practice. However, no data about the accuracy of the system using patient image data was achieved. Therefore, accuracy of the system with the use of CBCT scans and sphere detection should be further evaluated. For example, case studies

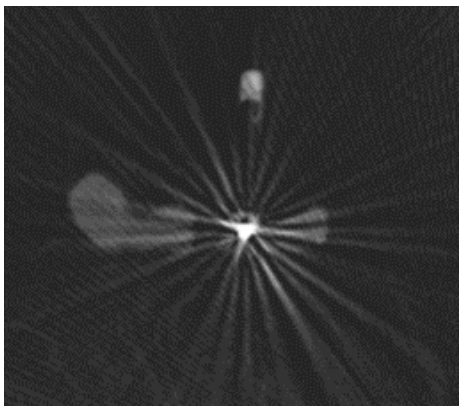

Figure 6.9: Streak artifacts in the CBCT scan due to the metal screw in the pubic bone of the sawbone model.

using animals or human remains can simulate the actual clinical setting. In such studies, the complete workflow can be evaluated and bone fragments can actually be reduced by using plates or screws. After fixation, a CT scan can be used to evaluate the quality of the reduction by comparing the surgical results with the preoperative plan. This will provide information needed to evaluate the clinical relevance of object-oriented navigation.

Chapter 7

Conclusions and future prospects

7.1 Conclusions

Pelvic fracture treatment demands appropriate treatment since adequate reconstructions can prevent early total hip implantation [19]. Currently, preoperative surgical planning of fracture reduction moves more and more towards the implementation of 3D information of patient specific anatomy [28]. 3D printing technology and virtual fracture reduction using 3D reconstructions improves surgical outcomes, however, no adequate tool to bring the virtual plan to the patient is currently available [34, 36].

Therefore, the aim of the current thesis was to develop and evaluate an object-oriented navigation (OON) system that can be used to translate a virtual surgical plan to the patient in the operation room. This tool can guide the medical specialist to the desired preoperatively determined surgical outcome, potentially improving healthcare by reducing blood loss, surgery time and postoperative hospital stay. In the recent years, mixed reality has been used to project the information of OON directly on the patient [74, 78, 121]. The main advantage of combining OON and mixed reality is that the user can keep its focus on the real world and experience the 3D perception of the fragments [116]. As the implementation of augmented reality (AR) in OON systems can improve patient outcome [116], the developed OON software in this study was combined with the Microsoft HoloLens.

During the graduation project, four studies were performed and combined to optimize and evaluate the developed OON system; (i) A method was described to find the optimal marker configuration for a specific optical tracking system by creation of a virtual optical tracking system; (ii) The performance of an optical tracker under varying circumstances was evaluated to determine the optimal conditions; (iii) An OON system was developed and its accuracy was assessed; (iv) The OON system was combined with the HoloLens to facilitate projection of the OON data on the patient. The accuracy of the enhanced OON system was evaluated and compared with the results of study (iii). In this thesis, the used optical tracker was the PST base infrared-based dual camera optical tracker.

(i). This study was performed to answer the first sub-question: *What is the optimal marker configuration for object-tracking using the optical tracker?* The camera-specific properties were acquired and used to create a virtual version of the optical tracker. Using a Monte Carlo analysis, different marker configurations with three, four or five markers were analyzed to evaluate the performance in a virtual setup. The outcome of the analysis showed that the optimal configuration must meet the following requirements; it must consist of five markers, have a nonlinear

distribution and the markers must be placed in a volume of approximately 20 x 20 x 20 cm. The results were in correspondence with literature. Based on these results and taking into account the clinical relevance, an optimal dynamic reference frame (DRF) was designed which was used in the next studies.

(ii). Using the optimal DRF designed in the study (i), different parameters that can influence the performance of an optical tracking system were evaluated to answer the second sub-question: *What is the influence of different conditions on the accuracy of the tracker?* The investigated conditions were the warming of the tracker, filter settings and the location of a DRF with respect to the tracker. A milling machine was used to translate a DRF according to a specified path. This path served as the ground truth for comparison of the measurements of the optical tracker. Measured locations of the DRF shifted 0.34 mm during warming up of the tracker and high filter settings significantly reduced the performance of the optical tracking system.

Assessment of the trueness of the tracker by evaluating different locations of the DRF in the field of view showed errors up to 8.9 mm in the z-direction, the direction away from the tracker. In the other directions, the mean error was 0.39 mm. The high error must be taken into account in developing clinical applications, since this error might lead to dangerous situations. Whereas the trueness of the system was cumbersome, the precision was high (mean error < 0.05 mm).

(iii). An OON system was developed and tested by placing a tracked objects at planned positions using the system as guidance. The mean difference between the measured location and the actual location was 0.6 mm and stayed below 1 mm. To evaluate the usability, objects were placed on planned positions using only the information displayed on the monitor. Mean displacement measured by the navigation system was 0.70 mm. The reported error was below the clinical required accuracy of 2 mm. These results gave answer to the third sub-question: *What is the accuracy of object-oriented navigation system?*

(iv). The OON system was combined with augmented reality by using the Microsoft HoloLens as HMD to display holograms of the objects at planned positions. Same experiments as in study (iii) were repeated, however, now the performance of the OON system linked with the HoloLens was tested. The measured deviation was 0.71 mm and did not show significant difference with the measured deviation of 0.6 mm found in the study (iii).

Using holograms as guidance, objects were placed at planned position and the deviation between the planned and placed objects were evaluated. The mean positioning error was 1.81 mm, with a maximal deviation of 3.94 mm. Errors larger than the clinical relevant accuracy of 2 mm were measured, so it can be concluded that the guidance using AR should be improved. These results answered the last sub-question: *What is the accuracy of object-oriented navigation in an augmented reality setting and what is the error in merging virtual and real objects?*

The answers to the sub-questions gave answer to the main research question: *What is the performance of the object-oriented surgical navigation system using an optical tracker?* It can be concluded that an optimal marker configuration was found using a simulation. Using the optimal configuration, the performance of the optical tracker was evaluated. The tracker performed well in x- and y-direction but showed large deviations from the ground truth in the z-direction. On the contrary, the precision of the system was high. Both the OON system with and without the combination of augmented reality reported errors below the clinical relevant accuracy. Using the

guidance of the system to place objects, mean deviations of 0.70 mm for the system without AR were seen. The combination with AR showed a mean error of 1.81 mm. The largest error seen in the tight-fit experiment without the use of AR was 1.40 mm, which is below the clinical relevant error of 2 mm. On the other hand, the presented guidance using the AR system showed a maximal error of 3.94 mm. This result indicates that improvements of the system are necessary before guidance using AR can be translated to clinical practice.

Several potential improvements were mentioned that will result in a higher accuracy of the AR guidance. On the contrary, use in clinical applications will probably reduce the accuracy. Therefore, it must be further investigated what the actual clinical relevant accuracy of the system will be. With an example using a sawbone model, it was shown that it is technically possible to use the system with clinical available data. A mixed reality setting was created by merging a virtual 3D model of the sawbone model with the physical sawbone model. However, there is much work to be done and inadequacies have to be addressed before the developed system will be implemented in clinical practice. Even then, further investigation must point out whether OON can improve the reduction of pelvic fracture.

7.2 Future prospects

As concluded, the developed system must be further improved before it can be implemented in the clinical setting. The main goal of improving AR guidance should be to stabilize the holograms displayed by the HoloLens. To achieve this, a data stream from the optical tracker to the HoloLens must be realized. This enables applications to run on the HoloLens itself, enabling the use of dedicated stabilization algorithms in the device.

Furthermore, the visualization must be improved, by investigating what information is needed and how the holograms are most beneficial for the user. Examples of improvements can be the adjustment of the mesh density or using a semi-transparent model. In mixed reality settings, less is more since an overload of data can confuse the user and distract his attention [143]. Furthermore, the 3D surface on the backside of a model was also rendered by the HoloLens and disturbed the 3D perception. It must be investigated whether the gaze direction of the user can be used to turn off the rendering of the backside of the 3D model. This will eventually create a better mixed reality as it mimics occlusion present in the real world.

An intuitive user interface can aid to switch between several different visualizations and add or remove guidance. Also, the color of the models indicated the distance between planned and tracked object helped the user in determining whether objects were placed correctly. Furthermore, retroreflective spheres can be projected over the physical markers, giving an additional indication about the fusion of virtual and real objects. Furthermore, the process of reconstructing the 3D models and the registration have to be performed automatically, reducing the time to setup the navigation system during surgery. In addition to displaying the 3D reconstructions of bones, rendering of vital structures such as the iliac vessels or the sciatic nerve might increase the value of the OON system [79].

Regarding accuracy, the errors up to 9 mm in the z-direction must be further investigated. It is necessary to evaluate if this error is present in clinically certified optical trackers. As the software can be combined with other optical trackers, a switch to trackers of other brands must be considered. Furthermore, the designed

DRFs must be manufactured using a more accurate fabrication process. The material of these manufactured DRFs must be shape-retaining, easy to sterilize and must not introduce artifacts in the image data. Use of carbon materials can be the solution as it satisfies these requirements [141,142]. Furthermore, a rigid system must be designed to attach the DRFs to the bone fragments without tolerating movement.

In this study, the OON system is applied for use in pelvic fracture treatment, however the system can potentially be used in other clinical situations. At the department of oral and maxillofacial surgery, the OON system can be used as guidance in the treatment of patients with craniosynostosis [144]. Another application that can benefit from the guidance of the OON system is the implantation of a click-prosthesis after leg amputations [145].

It must also be investigated whether a combination of optical and electromagnetic tracking (EM) systems or an EM tracker alone can be used in the OON system. This will solve the line-of-sight problem present in the optical tracking systems. The main drawbacks of EM trackers are the low accuracy and the fact that most currently used markers are active. A few types of passive markers are reported in literature but they are not yet used in clinical applications [48, 49]. If this technology improves and small passive EM markers can be used with high accuracy, EM tracking will eventually replace the optical trackers in the medical field.

OON can be used to improve the guidance in robotic operation systems. Dedicated robots such as the Da Vinci robot assist in complex surgery, but are currently guided by the specialist [146]. A system that uses a virtual plan and real time tracking input to guide a robot will improve surgery. With this technique, accurate tracking is combined with accurate controlled motion. This will eliminate the error introduced by human intervention [76, 147].

The 3D Lab at Radboudumc is aiming to have an impact on four main stages in patient-specific healthcare (Figure 7.1). Currently, only the first stage, the diagnosis of pelvic fractures, is supported by the use of 3D technology in the treatment of pelvic fractures. With the implementation of the described workflow in Chapter 6, two additional stages can be added since a patient-specific surgical plan and the translation of this plan to the simulated patient was realized. A future aspect to complement the philosophy of the 3D Lab is to evaluate the surgical outcome by comparing the postoperative situation with the preoperative plan. Correct implementation of these four stages will eventually result in a significant impact on healthcare.

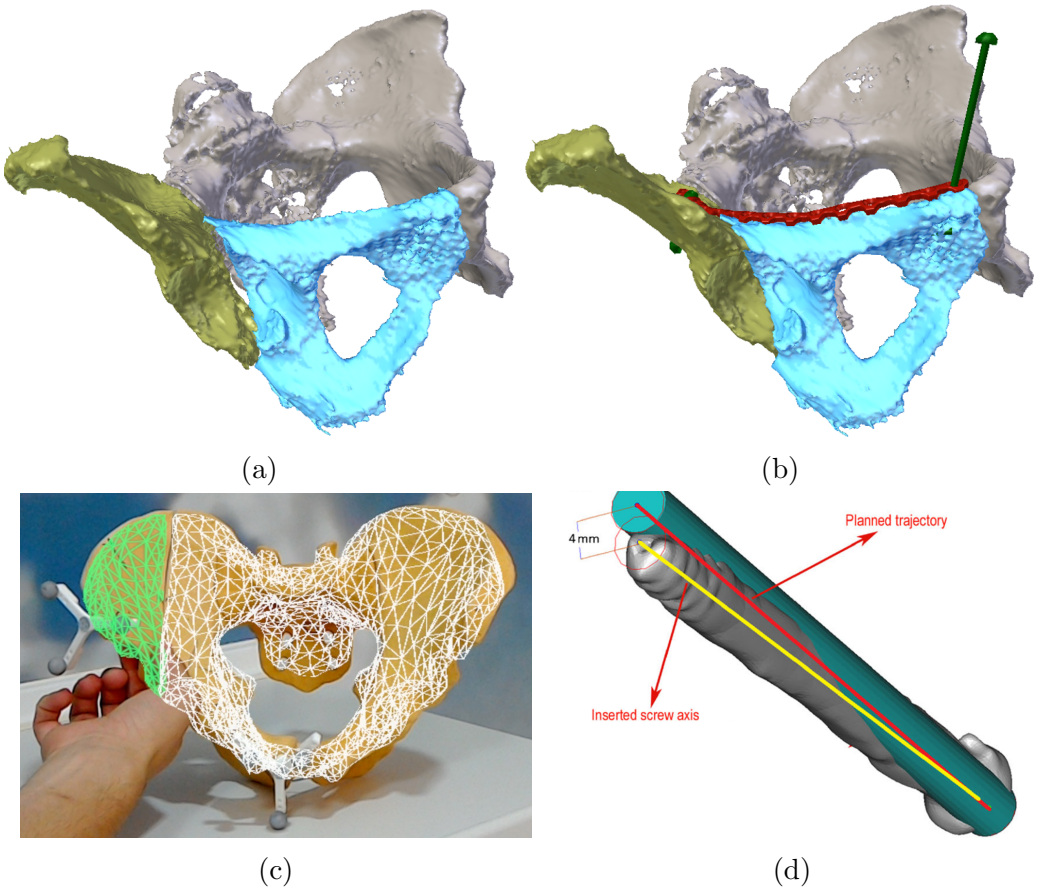

Figure 7.1: Future role of 3D techniques in pelvic fracture treatment specified by four stages. a) First stage: 3D reconstructions can aid in diagnosing pelvic fractures. b) Second stage: 3D surgical plan prepares the specialist for surgery. c) Third stage: Translation of surgical plan to the surgical setting to achieve results as planned d) Fourth stage: Postoperative evaluation of surgical outcome to compare surgical result with planned situation [79].

Bibliography

[1] Gray H. Anatomy of the human body. Lea and Febiger; 1918.

[2] Moore K, Dalley A, Agur A. Clinically oriented anatomy. Lippincott Williams & Wilkins; 2013.

[3] Walheim G, Olerud S, Ribbe T. *Mobility of the pubic symphysis: measurements by an electromechanical method.* Acta orthopaedica Scandinavica. 1984;**55**(2):203–208.

[4] Solonen KA. *The sacroiliac joint in the light of anatomical, roentgenological and clinical studies.* Acta orthopaedica Scandinavica. 1957;**27**:3–127.

[5] Vleeming A, Schuenke MD, Masi AT, et al. *The sacroiliac joint: an overview of its anatomy, function and potential clinical implications.* Journal of anatomy. 2012 dec;**221**(6):537–567.

[6] Levin S. *A different approach to the mechanics of the human pelvis: tensegrity.* In: Vleeming, editor. Movement, stability & low back pain. Chirchill Livingstone; 1997. p. 157–167.

[7] Dunet B, Tournier C, Billaud A, et al. *Acetabular fracture: Long-term follow-up and factors associated with secondary implantation of total hip arthroplasty.* Orthopaedics & Traumatology: Surgery & Research. 2013 may;**99**(3):281–290.

[8] Flint L, Cryer HG. *Pelvic Fracture: The Last 50 Years.* Journal of Trauma and Acute Care Surgery. 2010;**69**(3):483–488.

[9] Pohlemann T, Gänsslen A, Schellwald O, et al. *Outcome after pelvic ring injuries.* Injury. 1996;**27**:31–38.

[10] Zhou KH, Luo CF, Chen N, et al. *Minimally invasive surgery under fluoro-navigation for anterior pelvic ring fractures.* Indian journal of orthopaedics. 2016;**50**(3):250–255.

[11] Wong JML, Bucknill A. *Fractures of the pelvic ring.* Injury. 2017 apr;**48**(4):795–802.

[12] Culemann U, Scola A, Tosounidis G, et al. *Concept for treatment of pelvic ring injuries in elderly patients. A challenge.* Der Unfallchirurg. 2010 apr;**113**(4):258–271.

[13] Rollmann MF, Herath SC, Kirchhoff F, et al. *Pelvic ring fractures in the elderly now and then - a pelvic registry study.* Archives of Gerontology and Geriatrics. 2017;**71**:83–88.

[14] Alton TB, Gee AO. *Classifications in brief: young and burgess classification of pelvic ring injuries.* Clinical orthopaedics and related research. 2014 aug;**472**(8):2338–2342.

[15] Fornaro J, Keel M, Harders M, et al. *An interactive surgical planning tool for acetabular fractures: initial results.* Journal of Orthopaedic Surgery and Research. 2010;**5**(1):50.

[16] Simonian P, Routt M. *Biomechanics of pelvic fixation.* Orthopedic Clinics. 1997;**28**(3):351–367.

[17] Henderson RC. *The long-term results of nonoperatively treated major pelvic disruptions.* Journal of orthopaedic trauma. 1989;**3**(1):41–47.

[18] Papakostidis C, Kanakaris NK, Kontakis G, et al. *Pelvic ring disruptions: treatment modalities and analysis of outcomes.* International Orthopaedics. 2009 apr;**33**(2):329–338.

[19] Gary JL, Lefaivre KA, Gerold F, et al. *Survivorship of the native hip joint after percutaneous repair of acetabular fractures in the elderly.* Injury. 2011 oct;**42**(10):1144–1151.

[20] Evans AR, Pape HC. *Percutaneous Fixation of Geriatric Acetabular Fractures.* Operative Techniques in Orthopaedics. 2011 dec;**21**(4):265–271.

[21] Halawi MJ. *Pelvic ring injuries: Surgical management and long-term outcomes.* Journal of Clinical Orthopaedics and Trauma. 2015;**7**(1):1–6.

[22] Routt MLC, Kregor PJ, Simonian PT, et al. *Early Results of Percutaneous Iliosacral Screws Placed with the Patient in the Supine Position.* Journal of Orthopaedic Trauma. 1995;**9**(3):207–214.

[23] Kim JJ, Kim JW, Oh HK. *The submuscular sliding plate technique for acetabular posterior wall fractures extending to the acetabular roof.* Orthopaedics and Traumatology: Surgery and Research. 2014;**100**(8):967–970.

[24] Gay B, Goitz HT, Kahler A. *Percutaneous CT Guidance: Screw Fixation of Acetabular Fractures Preliminary Results of a New Technique.* American Journal of roentgenology. 1992;**158**(4):819–822.

[25] Matta J. *Operative Treatment of Acetabular Fractures Through the Ilioinguinal Approach A 10-Year Perspective.* Clinical orthopaedics and related research. 1994;**305**:10–19.

[26] Mardanpour K, Rahbar M. *The outcome of surgically treated traumatic unstable pelvic fractures by open reduction and internal fixation.* Journal of injury & violence research. 2013 jul;**5**(2):77–83.

[27] Lindahl J, Hirvensalo E, Böstman O, et al. *Failure of reduction with an external fixator in the management of pelvic ring injuries.* The Bone & Joint Journal. 1999 nov;**81**(6):955–962.

[28] Burk DL, Mears DC, Kennedy WH, et al. *Three-dimensional computed tomography of acetabular fractures.* Radiology. 1985 apr;**155**(1):183–186.

[29] Falchi M, Rollandi GA. *CT of pelvic fractures.* European Journal of Radiology. 2004 apr;**50**(1):96–105.

[30] Hutten R, Lomasney LM, Vasilopoulos V, et al. *Practicality of exchanging transparent 3D CT for radiography for pelvic fractures.* Clinical Imaging. 2017;**44**:70–73.

[31] Scheinfeld MH, Dym AA, Spektor M, et al. *Acetabular Fractures: What Radiologists Should Know and How 3D CT Can Aid Classification.* Radiographics. 2015 mar;**35**(2):555–577.

[32] Mosheiff R, Khoury A, Weil Y, et al. *First generation computerized fluoroscopic navigation in percutaneous pelvic surgery.* Journal of orthopaedic trauma. 2004 feb;**18**(2):106–111.

[33] Lin YC, Chen CH, Huang HT, et al. *Percutaneous antegrade screwing for anterior column fracture of acetabulum with fluoroscopic-based computerized navigation.* Archives of Orthopaedic and Trauma Surgery. 2008 feb;**128**(2):223–226.

[34] Wu XB, Wang JQ, Zhao CP, et al. *Printed three-dimensional anatomic templates for virtual preoperative planning before reconstruction of old pelvic injuries: initial results.* Chinese medical journal. 2015 feb;**128**(4):477–482.

[35] Zeng C, Xiao J, Wu Z, et al. *Evaluation of three-dimensional printing for internal fixation of unstable pelvic fracture from minimal invasive para-rectus abdominis approach: a preliminary report.* International journal of clinical and experimental medicine. 2015;**8**(8):13039–13044.

[36] Lee PY, Lai JY, Yu SA, et al. *Computer-assisted Fracture Reduction and Fixation Simulation for Pelvic Fractures.* Journal of Medical and Biological Engineering. 2014;**34**(4):368–376.

[37] Lei J, Zhang Y, Wu G, et al. *The Influence of Pelvic Ramus Fracture on the Stability of Fixed Pelvic Complex Fracture.* Computational and Mathematical Methods in Medicine. 2015 oct;p. 1–11.

[38] Wang D, Wang Y, Wu S, et al. *Customized a Ti6Al4V Bone Plate for Complex Pelvic Fracture by Selective Laser Melting.* Materials. 2017 jan;**10**(1):14–23.

[39] Upex P, Jouffroy P, Riouallon G. *Application of 3D printing for treating fractures of both columns of the acetabulum: Benefit of pre-contouring plates on the mirrored healthy pelvis.* Orthopaedics & Traumatology: Surgery & Research. 2017;**103**(3):331–334.

[40] Cimerman M, Kristan A. *Preoperative planning in pelvic and acetabular surgery: The value of advanced computerised planning modules.* Injury. 2007 apr;**38**(4):442–449.

[41] Boudissa M, Chabanas M, Oliveri H, et al. *Virtual fracture reduction of the acetabulum using a rigid body biomechanical model.* Revue de Chirurgie Orthopédique et Traumatologique. 2015 nov;**101**(7):s187.

[42] Hu Y, Li H, Qiao G, et al. *Computer-assisted virtual surgical procedure for acetabular fractures based on real CT data.* Injury. 2011;**42**(10):1121–1124.

[43] Scolaro JA, Firoozabadi R, Routt ML. *Treatment of Pediatric and Adolescent Pelvic Ring Injuries With Percutaneous Screw Placement.* Journal of pediatric orthopedics. 2017;p. 1–5.

[44] Chen X, Yuan J, Wang C, et al. *Modular preoperative planning software for computer-aided oral implantology and the application of a novel stereolithographic template: a pilot study.* Clinical implant dentistry and related research. 2010 sep;**12**(3):181–193.

[45] Chen X, Xu L, Wang Y, et al. *Image-guided installation of 3D-printed patient-specific implant and its application in pelvic tumor resection and reconstruction surgery.* Computer Methods and Programs in Biomedicine. 2016 mar;**125**:66–78.

[46] Birkfellner W, Hummel J, Wilson E, et al. *Tracking Devices.* In: Peters T, Cleary K, editors. Image-Guided Interventions. Boston, MA: Springer US; 2008. p. 23–44.

[47] Meola A, Cutolo F, Carbone M, et al. *Augmented reality in neurosurgery: a systematic review.* Neurosurgical Review. 2016;p. 1–12.

[48] Willoughby TR, Kupelian PA, Pouliot J, et al. *Target localization and real-time tracking using the Calypso 4D localization system in patients with localized prostate cancer.* International Journal of Radiation Oncology*Biology*Physics. 2006 jun;**65**(2):528–534.

[49] Huang J, Mori T, Takashima K, et al. *IM6D: Magnetic tracking system with 6-DOF passive markers for dexterous 3D interaction and motion.* ACM Transactions on Graphics. 2015;**34**(6):217.

[50] Mirota DJ, Ishii M, Hager GD. *Vision-Based Navigation in Image-Guided Interventions.* Annual Review of Biomedical Engineering. 2011 aug;**13**(1):297–319.

[51] Menditto A, Patriarca M, Magnusson B. *Understanding the meaning of accuracy, trueness and precision.* Accreditation and Quality Assurance. 2007 jan;**12**(1):45–47.

[52] Khadem R, Yeh CC, Sadeghi-Tehrani M, et al. *Comparative Tracking Error Analysis of Five Different Optical Tracking Systems.* Computer Aided Surgery. 2000;**5**(2):98–107.

[53] Maes F, Collignon A, Vandermeulen D, et al. *Multimodality image registration by maximization of mutual information.* IEEE Transactions on Medical Imaging. 1997 apr;**16**(2):187–198.

[54] Maurer CR, Fitzpatrick JM, Wang MY, et al. *Registration of head volume images using implantable fiducial markers.* IEEE Transactions on Medical Imaging. 1997;**16**(4):447–462.

[55] Bale RJ, Laimer I, Martin A, et al. *Frameless Stereotactic Cannulation of the Foramen Ovale for Ablative Treatment of Trigeminal Neuralgia.* Operative Neurosurgery. 2006 oct;**59**(4):394–402.

[56] Bucholz RD, Ho HW, Rubin JP. *Variables affecting the accuracy of stereotactic localization using computerized tomography.* Journal of Neurosurgery. 1993;**79**(5):667–673.

[57] Galloway RL, Maciunas RJ, Latimer JW. *The accuracies of four stereotactic frame systems: an independent assessment.* Biomedical instrumentation & technology. 1991;**25**(6):457–460.

[58] Loubele M, Van Assche N, Carpentier K, et al. *Comparative localized linear accuracy of small-field cone-beam CT and multislice CT for alveolar bone measurements.* Oral Surgery, Oral Medicine, Oral Pathology, Oral Radiology, and Endodontology. 2008 apr;**105**(4):512–518.

[59] Widmann G, Stoffner R, Bale R. *Errors and error management in image-guided craniomaxillofacial surgery.* Oral Surgery, Oral Medicine, Oral Pathology, Oral Radiology and Endodontology. 2009;**107**(5):701–715.

[60] West JB, Maurer CR. *Designing optically tracked instruments for image-guided surgery.* IEEE Transactions on Medical Imaging. 2004;**23**(5):533–545.

[61] Luebbers HT, Messmer P, Obwegeser JA, et al. *Comparison of different registration methods for surgical navigation in cranio-maxillofacial surgery.* Journal of Cranio-Maxillofacial Surgery. 2008;**36**(2):109–116.

[62] West JB, Fitzpatrick JM, Toms SA, et al. *Fiducial point placement and the accuracy of point-based, rigid body registration.* Neurosurgery. 2001;**48**(4):810–817.

[63] Wiles AD, Thompson DG, Frantz DD. *Accuracy assessment and interpretation for optical tracking systems.* In: Proceedings of SPIE. Vol. 5367; 2004. p. 421–432.

[64] Wenbo Liu, Hui Ding, Hongyan Han, et al. *The study of fiducial localization error of image in point-based registration.* In: 2009 Annual International Conference of the IEEE Engineering in Medicine and Biology Society. IEEE; 2009. p. 5088–5091.

[65] Moghari MH, Abolmaesumi P. *Understanding the Effect of Bias in Fiducial Localization Error on Point-Based Rigid-Body Registration.* IEEE Transactions on Medical Imaging. 2010 oct;**29**(10):1730–1738.

[66] Fitzpatrick JM, West JB, Maurer CR. *Predicting error in rigid-body point-based registration.* IEEE Transactions on Medical Imaging. 1998;**17**(5):694–702.

[67] Malloy KM, Milling LS. *The effectiveness of virtual reality distraction for pain reduction: A systematic review.* Clinical Psychology Review. 2010 dec;**30**(8):1011–1018.

[68] Moro C, Štromberga Z, Raikos A, et al. *The effectiveness of virtual and augmented reality in health sciences and medical anatomy.* Anatomical Sciences Education. 2017 apr;p. 1–1.

[69] Kamphuis C, Barsom E, Schijven M, et al. *Augmented reality in medical education?* Perspectives on medical education. 2014 sep;**3**(4):300–311.

[70] Pelargos PE, Nagasawa DT, Lagman C, et al. *Utilizing virtual and augmented reality for educational and clinical enhancements in neurosurgery.* Journal of Clinical Neuroscience. 2017;**35**:1–4.

[71] Zhang X, Chen G, Liao H. *High Quality See-Through Surgical Guidance System Using Enhanced 3D Autostereoscopic Augmented Reality.* IEEE Transactions on Biomedical Engineering. 2017;**64**(8):1815–1825.

[72] Baum Z, Ungi T, Lasso A, et al. *Usability of a real-time tracked augmented reality display system in musculoskeletal injections.* In: Proc. SPIE 10135, Medical Imaging 2017: Image-Guided Procedures, Robotic Interventions, and Modeling, 101352T; 2017. p. 101352T–1 – 101352T–8.

[73] Nicolau S, Soler L, Mutter D, et al. *Augmented reality in laparoscopic surgical oncology.* Surgical Oncology. 2011 sep;**20**(3):189–201.

[74] Birkfellner W, Figl M, Huber K, et al. *A head-mounted operating binocular for augmented reality visualization in medicine - design and initial evaluation.* IEEE Transactions on Medical Imaging. 2002 aug;**21**(8):991–997.

[75] Stöckle U, Schaser K, König B. *Image guidance in pelvic and acetabular surgery-expectations, success and limitations.* Injury. 2007;**38**(4):450–462.

[76] Dagnino G, Georgilas I, Köhler P, et al. *Navigation system for robot-assisted intra-articular lower-limb fracture surgery.* International Journal of Computer Assisted Radiology and Surgery. 2016;**11**(10):1831–1843.

[77] Chen X, Xu L, Sun Y, et al. *A review of computer-aided oral and maxillofacial surgery: planning, simulation and navigation.* Expert Review of Medical Devices. 2016 nov;**13**(11):1043–1051.

[78] Chen X, Xu L, Wang Y, et al. *Development of a surgical navigation system based on augmented reality using an optical see-through head-mounted display.* Journal of Biomedical Informatics. 2015 jun;**55**:124–131.

[79] Wang H, Wang F, Leong APY, et al. *Precision insertion of percutaneous sacroiliac screws using a novel augmented reality-based navigation system: a pilot study.* International Orthopaedics. 2016 sep;**40**(9):1941–1947.

[80] Badiali G, Ferrari V, Cutolo F, et al. *Augmented reality as an aid in maxillofacial surgery: Validation of a wearable system allowing maxillary repositioning.* Journal of Cranio-Maxillofacial Surgery. 2014 dec;**42**(8):1970–1976.

[81] Vigh B, Müller S, Ristow O, et al. *The use of a head-mounted display in oral implantology: a feasibility study.* International Journal of Computer Assisted Radiology and Surgery. 2014 jan;**9**(1):71–78.

[82] Mahmoud N, Grasa OG, Nicolau SA, et al. *On-patient see-through augmented reality based on visual SLAM.* International Journal of Computer Assisted Radiology and Surgery. 2017 jan;**12**(1):1–11.

[83] Morley C, Choudhry O, Kelly S, et al.. *SIIM 2017 Scientific Session Posters & Demonstrations Mixed Reality Visualization of Medical Imaging Data*; 2017. Available from: https://siim.org/page/17s_posters_demos.

[84] Syed AZ, Zakaria A, Lozanoff S. *Dark room to augmented reality: Application of HoloLens technology for oral radiological diagnosis.* Oral Surgery, Oral Medicine, Oral Pathology and Oral Radiology. 2017 jul;**124**(1):33.

[85] Jones D, Christopherson DA, Washington JT, et al. *A Frameless Method for Stereotaxic Radiotherapy.* British Journal of Radiology. 1993;**66**(792):1142–1150.

[86] Peters T, Davey B, Munger P, et al. *Three-dimensional multimodal image-guidance for neurosurgery.* IEEE Transactions on Medical Imaging. 1996;**15**(2):121–128.

[87] Fitzpatrick JM, West JB. *The distribution of target registration error in rigid-body point-based registration.* IEEE Transactions on Medical Imaging. 2001;**20**(9):917–927.

[88] Maurer, Jr CR, McCrory JJ, Fitzpatrick JM. *Estimation of accuracy in localizing externally attached markers in multimodal volume head images.* In: Medical Imaging 1993: Image Processing. Volume 1898; 1993. p. 43–54.

[89] Metropolis N, Ulam S. *The Monte Carlo Method.* Journal of the American Statistical Association. 1949 sep;**44**(247):335–341.

[90] Sorenson HW. *Least-squares estimation: from Gauss to Kalman.* IEEE Spectrum. 1970 jul;**7**(7):63–68.

[91] Zhang Z. *A Flexible New Technique for Camera Calibration.* IEEE Transactions on Pattern Analysis and Machine Intelligence. 2000;**22**(11):1330–1334.

[92] Henrichsen A. 3D Reconstruction and Camera Calibration from 2D Images [Thesis]. University of Cape Town; 2000.

[93] Kalman RE. *A New Approach to Linear Filtering and Prediction Problems.* Journal of Basic Engineering. 1960;**82**(1):35–45.

[94] Van der Heijden F. *Visual navigation: 3D Computer Vision for Medical Applications.* University of Twente - RAM; 2016.

[95] Kabsch W. *A solution for the best rotation to relate two sets of vectors.* Acta Crystallographica Section A: Crystal Physics, Diffraction, Theoretical and General Crystallography. 1976 sep;**32**(5):922–923.

[96] Gower JC. *Generalized procrustes analysis.* Psychometrika. 1975 mar;**40**(1):33–51.

[97] Bauer M, Schlegel M, Pustka D, et al. *Predicting and estimating the accuracy of n-occular optical tracking systems.* In: 2006 IEEE/ACM International Symposium on Mixed and Augmented Reality. IEEE; 2006. p. 43–51.

[98] Trübswetter C. Analyzing and Monitoring Tracking Accuracy of an A.R.T System [Thesis]. Technical University of Munich; 2003.

[99] Gundle KR, White JK, Conrad EU, et al. *Accuracy and Precision of a Surgical Navigation System: Effect of Camera and Patient Tracker Position and Number of Active Markers.* The Open Orthopaedics Journal. 2017 may;**11**(1):493–501.

[100] Wagner A, Wanschitz F, Birkfellner W, et al. *Computer-aided placement of endosseous oral implants in patients after ablative tumour surgery: assessment of accuracy.* Clinical Oral Implants Research. 2003 may;**14**(3):340–348.

[101] Wanschitz F, Birkfellner W, Figl M, et al. *Computer-enhanced stereoscopic vision in a head- mounted display for oral implant surgery.* Clinical Oral Implants Research. 2002;**13**(6):610–616.

[102] Cartiaux O, Banse X, Paul L, et al. *Computer-assisted planning and navigation improves cutting accuracy during simulated bone tumor surgery of the pelvis.* Computer Aided Surgery. 2013 jan;**18**(1-2):19–26.

[103] Jolles BM, Genoud P, Hoffmeyer P. *Computer-assisted Cup Placement Techniques in Total Hip Arthroplasty Improve Accuracy of Placement.* Clinical Orthopaedics and Related Research. 2004 sep;**426**:174–179.

[104] Anderson TWW, Darling DA. *Asymptotic theory of certain "goodness of fit" criteria based on stochastic processes.* The annals of mathematical statistics. 1952;**23**(2):193–212.

[105] Student. *The probable error of a mean.* Biometrika. 1908;**6**(1):1–25.

[106] Wilcoxon F. *Individual Comparisons by Ranking Methods.* Biometrics Bulletin. 1945 dec;**1**(6):80–83.

[107] Kindratenko VV. *A survey of electromagnetic position tracker calibration techniques.* Virtual Reality. 2000 sep;**5**(3):169–182.

[108] Much J. Error Classification and Propagation for Electromagnetic Tracking [Thesis]. Technical University of Munich; 2008.

[109] Smith HE, Welsch MD, Sasso RC, et al. *Comparison of radiation exposure in lumbar pedicle screw placement with fluoroscopy vs computer-assisted image guidance with intraoperative three-dimensional imaging.* The journal of spinal cord medicine. 2008;**31**(5):532–537.

[110] Joskowicz L, Milgrom C, Simkin A, et al. *FRACAS: a System for Computer-Aided Image-Guided Long Bone Fracture Surgery.* Computer Aided Surgery. 1998 jan;**3**(6):271–288.

[111] Shen F, Chen B, Guo Q, et al. *Augmented reality patient-specific reconstruction plate design for pelvic and acetabular fracture surgery.* International Journal of Computer Assisted Radiology and Surgery. 2013;**8**(2):169–179.

[112] Drazin D, Bhamb N, Al-Khouja LT, et al. *Image-guided resection of aggressive sacral tumors.* Neurosurgical Focus. 2017 jan;**42**(1):E15.

[113] Wu K, Webber NP, Ward RA, et al. *Intraoperative navigation for minimally invasive resection of periarticular and pelvic tumors.* Orthopedics. 2011 may;**34**(5):370–376.

[114] Yan C, Shi Y, Yang J, et al. *Investigation into the selective laser sintering of styrene-acrylonitrile copolymer and postprocessing.* The International Journal of Advanced Manufacturing Technology. 2010 dec;**51**(9):973–982.

[115] Gols Linthorst FAJ. De ontwikkeling en in vitro validatie van een prototype voor computergenavigeerde plaatsing van tandwortelimplantaten [Thesis]. Radboud University Nijmegen; 2016.

[116] Zhang X, Fan Z, Wang J, et al. *3D Augmented Reality Based Orthopaedic Interventions.* In: Zheng G, Li S, editors. Lecture Notes in Computational Vision and Biomechanics. Springer, Cham; 2016. p. 71–90.

[117] Sielhorst T, Feuerstein M, Navab N. *Advanced Medical Displays: A Literature Review of Augmented Reality.* Journal of Display Technology. 2008 dec;**4**(4):451–467.

[118] Okamoto T, Onda S, Yanaga K, et al. *Clinical application of navigation surgery using augmented reality in the abdominal field.* Surgery Today. 2015 apr;**45**(4):397–406.

[119] Lin YK, Yau HT, Wang IC, et al. *A Novel Dental Implant Guided Surgery Based on Integration of Surgical Template and Augmented Reality.* Clinical Implant Dentistry and Related Research. 2015 jun;**17**(3):543–553.

[120] Maurer CR, Sauer F, Hu B, et al. *Augmented reality visualization of brain structures with stereo and kinetic depth cues: System description and initial evaluation with head phantom.* In: Proc. SPIE 4319, Medical Imaging 2001: Visualization, Display, and Image-Guided Procedures, 445; 2001. p. 445–456.

[121] Kersten-Oertel M, Gerard I, Drouin S, et al. *Augmented reality in neurovascular surgery: feasibility and first uses in the operating room.* International Journal of Computer Assisted Radiology and Surgery. 2015 nov;**10**(11):1823–1836.

[122] Cutolo F, Carbone M, Parchi PD, et al. *Application of a New Wearable Augmented Reality Video See-Through Display to Aid Percutaneous Procedures in Spine Surgery.* In: De Paolis L, Mongelli A, editors. Augmented Reality, Virtual Reality, and Computer Graphics. AVR 2016. Lecture Notes in Computer Science, vol 9769. Springer; 2016. p. 43–54.

[123] Zielke MA, Zakhidov D, Hardee G, et al. *Developing Virtual Patients with VR/AR for a natural user interface in medical teaching.* In: 2017 IEEE 5th International Conference on Serious Games and Applications for Health (SeGAH). IEEE; 2017. p. 1–8.

[124] Ebert LC, Hatch G, Ampanozi G, et al. *You can't touch this: touch-free navigation through radiological images.* Surgical Innovation. 2012 sep;**19**(3):301–307.

[125] Hanna MG. *SIIM 2017 Scientific Session Posters & Demonstrations Pathology Specimen Radiograph Co-Registration Using the HoloLens Improves Physician Assistant Workflow*; 2017. Available from: https://siim.org/page/17s_posters_demos.

[126] Golab MR, Breedon PJ, Vloeberghs M. *A wearable headset for monitoring electromyography responses within spinal surgery.* European Spine Journal. 2016 oct;**25**(10):3214–3219.

[127] Venkataram A, Ellur S, Kujur AR, et al. *Smart apps for the smart plastic surgeon.* Indian journal of plastic surgery: official publication of the Association of Plastic Surgeons of India. 2015;**48**(1):66–74.

[128] Qian L, Barthel A, Johnson A, et al. *Comparison of optical see-through head-mounted displays for surgical interventions with object-anchored 2D-display.* International Journal of Computer Assisted Radiology and Surgery. 2017 jun;**12**(6):901–910.

[129] Katić D, Spengler P, Bodenstedt S, et al. *A system for context-aware intraoperative augmented reality in dental implant surgery.* International Journal of Computer Assisted Radiology and Surgery. 2015 jan;**10**(1):101–108.

[130] Tuceryan M, Navab N. *Single-Point active alignment method (SPAAM) for optical see-through HMD calibration for augmented reality.* Presence: Teleoperators and Virtual Environments. 2002;**11**(3):259–276.

[131] Besharati Tabrizi L, Mahvash M. *Augmented reality-guided neurosurgery: accuracy and intraoperative application of an image projection technique.* Journal of Neurosurgery. 2015 jul;**123**(1):206–211.

[132] Abrassart S, Stern R, Peter R. *Morbidity Associated With Isolated Iliac Wing Fractures.* Journal of Trauma and Acute Care Surgery. 2009 jan;**66**(1):200–203.

[133] Available from: http://orthoinfo.aaos.org/menus/hip.cfm;. Cited: 03-07-2017.

[134] Besl PJ, McKay HD. *A method for registration of 3-D shapes.* IEEE Transactions on Pattern Analysis and Machine Intelligence. 1992;**14**(2):239–256.

[135] Mitchell J, Labadie RF, Fitzpatrick JM. *Design of a Novel Device to Provide Assured Seating of Bone Implanted Fiducial Markers.* Journal of Medical Devices. 2010;**4**(2):025002–025002–4.

[136] Xie L. *Spherical hough transform for 3D images*;. Cited: 21-06-2017. Available from: https://nl.mathworks.com/matlabcentral/fileexchange/48219-spherical-hough-transform-for-3d-images.

[137] Lawrence TM, White CT, Wenn R, et al. *The current hospital costs of treating hip fractures.* Injury. 2005 jan;**36**(1):88–91.

[138] Tile M, Helfet D, Kellam J. Fractures of the pelvis and acetabulum. Lippincott Williams & Wilkins; 2003.

[139] Giannoudis PV, Tzioupis CC, Pape HC, et al. *Percutaneous fixation of the pelvic ring.* Bone & Joint Journal. 2007;**89**(2):145–154.

[140] Schulze R, Heil U, Gross D, et al. *Artefacts in CBCT: a review.* Dentomaxillofacial radiology. 2011 jul;**40**(5):265–273.

[141] de Jong JJA, Lataster A, van Rietbergen B, et al. *Distal radius plate of CFR-PEEK has minimal effect compared to titanium plates on bone parameters in high-resolution peripheral quantitative computed tomography: a pilot study.* BMC medical imaging. 2017 feb;**17**(1):18.

[142] Nevelsky A, Borzov E, Daniel S, et al. *Perturbation effects of the carbon fiber-PEEK screws on radiotherapy dose distribution.* Journal of Applied Clinical Medical Physics. 2017 mar;**18**(2):62–68.

[143] Dixon BJ, Daly MJ, Chan H, et al. *Surgeons blinded by enhanced navigation: the effect of augmented reality on attention.* Surgical Endoscopy. 2013 feb;**27**(2):454–461.

[144] Chim H, Wetjen N, Mardini S. *Virtual surgical planning in craniofacial surgery.* Seminars in plastic surgery. 2014 aug;**28**(3):150–158.

[145] Frölke JPM, Leijendekkers RA, van de Meent H. *Osseointegrated prosthesis for patients with an amputation: Multidisciplinary team approach in the Netherlands.* Der Unfallchirurg. 2017 apr;**120**(4):293–299.

[146] Freschi C, Ferrari V, Melfi F, et al. *Technical review of the da Vinci surgical telemanipulator.* The International Journal of Medical Robotics and Computer Assisted Surgery. 2013 dec;**9**(4):396–406.

[147] Kong X, Duan X, Wang Y. *An integrated system for planning, navigation and robotic assistance for mandible reconstruction surgery.* Intelligent Service Robotics. 2016 apr;**9**(2):113–121.

Appendix A

Additional activities

In this appendix, scientific and clinical activities that I worked on during the internship besides the described studies are summarized.

Development of a method to investigate the displacement of the acetabular dome after surgery of acetabular fractures	Fracture reduction in acetabular fractures is currently assessed by evaluation of 'steps and gaps' in the articular surface of the acetabulum. A new method was developed to compare the pathological acetabulum with the non-impared ipsilateral acetabulum. A pilot study was performed to evaluate the symmetry of the left and right acetabular dome in healthy individuals using surface based matching. Preliminary results showed high symmetry between both domes which encourages to extend the investigation to surgically reconstructed acetabula.
Assisting in a grant application for improvement of diagnosis and intraoperative comparison in children with bilateral Wilms tumors	Image data of children with bilateral Wilms tumors was used to generate 3D models of kidney and associate organs in real-size dimensions. An animation of the models was created and loaded on the HoloLens. This method will be used to improve the perception of patient specific anatomy and for comparison with the intraoperative situation. The study comprises a comparison between conventional image modalities, 3D printing and the use of augmented reality in anatomical perception.
Developing of a semi-automatic resuscitation algorithm in an augmented reality environment	At the department of neonatology, the compliance of the specialists to the resuscitation algorithm during resuscitation of the premature newborn remains a difficult but lifesaving task. To aid the neonatologist, a tool is developed on the HoloLens that guides the user through the algorithm and displays the data from several sensors such as temperature and heart rate.

Assisting with introducing the concept of pre-bending osteosynthesis plates for the fixation of pelvic fractures	CT scans of patients with pelvic ring fractures were used to reconstruct and 3D print the impaired pelvis. Besides informing the patient with these 3D models, this technology was used to contour the fixation plates pre-operatively. After bending, plates were sterilized and used during surgery. All plates showed a good fit and no additional bending was required.
Introducing 3D reconstructions in the weekly patient discussion	To improve the perception of pelvic fractures, 3D reconstructions of every patient with complex pelvic ring fractures were created. During the weekly patient discussion, these reconstructions were presented to the medical staff.
Minor work for the 3D lab at the departments of Oral and Maxillofacial surgery, trauma surgery and ear, nose and throat surgery at the Radboud UMC	During the internship, several clinical activities were performed such as; creation of 3D stereophotographs, creation of 3D reconstructions, planning screw trajectories for 3D navigation in pelvic ring fractures, comparing pre- and postoperative image data and realizing the fusion of MR and CT images for image-guided surgery.

Appendix B

Procrustes algorithm

The Procrustes algorithm is an easy method to align two sets of coordinates / points (Figure B.1). The two sets of points required as input must be equal in size and the order of the points in both sets must be the same. The data sets can be described by corresponding points $\mathbf{x}_n$ and $\mathbf{y}_n$ in 3xN matrices $\mathbf{X}$ and $\mathbf{Y}$. The output is a linear transformation with rotation ($\mathbf{R}$), scale (S), translation ($\mathbf{t}$) and reflection components [95, 96]. These parameters can be used to transform coordinates in $\mathbf{Y}$ to $\mathbf{X}$ using the linear transformation: $\mathbf{x}_n = S\mathbf{R}\mathbf{y}_n + \mathbf{t}$.

The following steps are necessary to calculate the linear transformation:

1. Normalization of $\mathbf{X}$ and $\mathbf{Y}$ with respect to the centroids:

   - Calculate centroids of datasets:

$$\bar{\mathbf{x}} = \frac{1}{N}\sum_{n=1}^{N}\mathbf{x}_n \tag{B.1}$$

$$\bar{\mathbf{y}} = \frac{1}{N}\sum_{n=1}^{N}\mathbf{y}_n \tag{B.2}$$

   - Normalize for each n:

$$\tilde{\mathbf{x}}_n = \mathbf{x}_n - \bar{\mathbf{x}} \tag{B.3}$$

$$\tilde{\mathbf{y}}_n = \mathbf{y}_n - \bar{\mathbf{y}} \tag{B.4}$$

2. Calculation and neutralization the scale S:

   - Calculate the scale:

$$\hat{S} = \frac{\sum_{n=1}^{N}\|\mathbf{x}_n\|}{\sum_{n=1}^{N}\|\mathbf{y}_n\|} \tag{B.5}$$

   - Rescale $\tilde{\mathbf{x}}_n$:

$$\tilde{\mathbf{x}}_n = \frac{1}{S}\tilde{\mathbf{x}}_n \tag{B.6}$$

3. Calculation of the rotation matrix $\mathbf{R}$ using the Kabsch algorithm [95]:

   - Apply singular value decomposition to calculate $\mathbf{U}$,$\mathbf{S}$,$\mathbf{V}$, such that:

$$\mathbf{U}\mathbf{S}\mathbf{V}^T = \tilde{\mathbf{X}}\tilde{\mathbf{Y}}^T \tag{B.7}$$

- Calculate the rotation matrix $\mathbf{R}$:

$$\hat{\mathbf{R}} = \mathbf{U}\mathbf{W}\mathbf{V}^T \tag{B.8}$$

- Compensate for reflection (if present and unwanted):

$$\hat{\mathbf{R}} = \mathbf{U}\begin{bmatrix} 1 & 0 & 0 \\ 0 & 1 & 0 \\ 0 & 0 & det(\mathbf{U}\mathbf{V}^T) \end{bmatrix}\mathbf{V}^T \tag{B.9}$$

4. Calculation of the translation vector:

$$\hat{\mathbf{t}} = \bar{\mathbf{x}} - \hat{S}\hat{\mathbf{R}}\bar{\mathbf{y}} \tag{B.10}$$

Now, the coordinates in $\mathbf{Y}$ can be transformed to $\mathbf{X}$ using the following formula:

$$\mathbf{y}'_n = S\mathbf{R}\mathbf{y}_n + \mathbf{t} \tag{B.11}$$

Here, $\mathbf{y}'_n$ are the coordinates in $\mathbf{X}$ transformed to the coordinates in $\mathbf{Y}$. Reflection can be allowed by ignoring equation B.9. Scaling can be ignored by applying $S = 1$ or leaving S out of formula B.11.

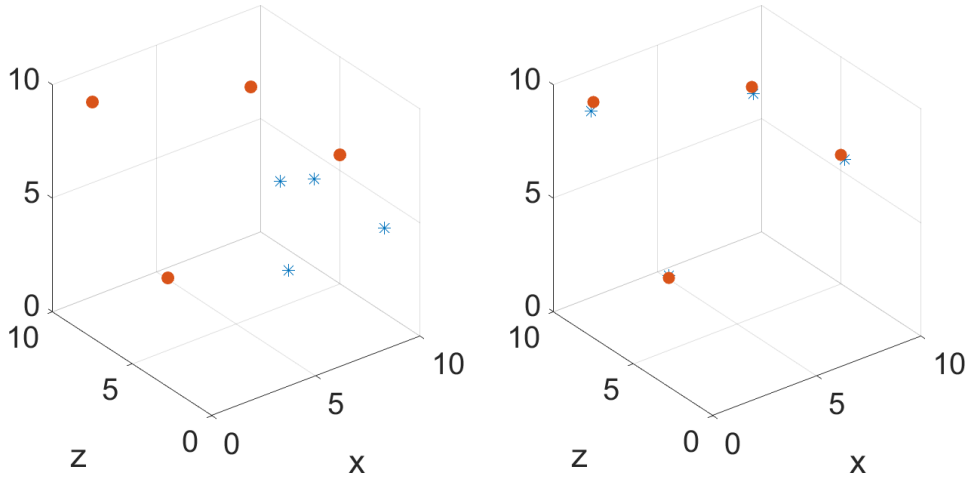

Figure B.1: Example of the Procrustes algorithm used to calculate the optimal transformation to transform points in dataset $\mathbf{Y}$ (blue asterisks) to the corresponding points in dataset $\mathbf{X}$ (red circles).

Appendix C

Box-and-whisker plots of results

The box-and-whisker plots show the errors for the simulated and measured data of Chapter 2-5. The edges of the box are the 25^{th} and 75^{th} percentiles, whereas the whiskers extend to the most extreme data points that are not considered as outliers. The outliers are defined as data points being larger than $Q1 - 1.5(Q3 - Q1)$ and $Q3 + 1.5(Q3 - Q1)$, where $Q1$ and $Q3$ represent the first and third quartile (25^{th} and 75^{th} percentile), respectively. Outliers are plotted individually.

Box-and-whisker plots for Chapter 2

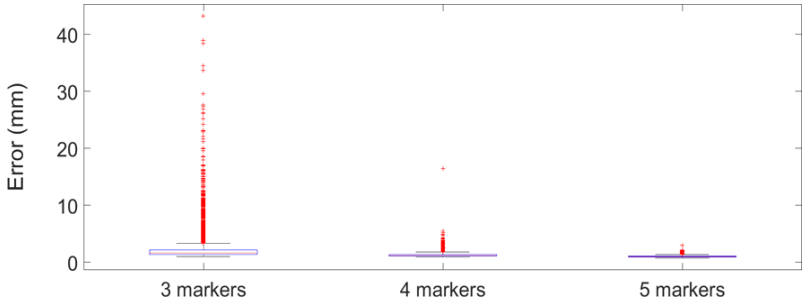

Figure C.1: Errors from MCA for 10000 random DRFs. Box-and-whisker plots of the absolute errors calculated in the MCA for DRFs with three, four and five markers. Note the decrease in error when number of markers is increased.

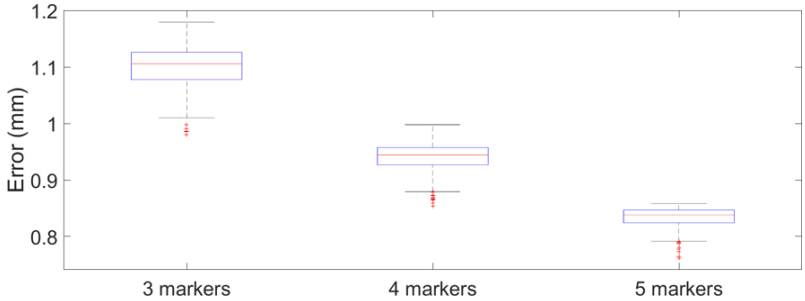

Figure C.2: Errors from MCA for 500 optimal DRFs. Box-and-whisker plots of the absolute errors calculated in the MCA for DRFs with three, four and five markers. Note the decrease in error when number of markers is increased.

Box-and-whisker plots for Chapter 3

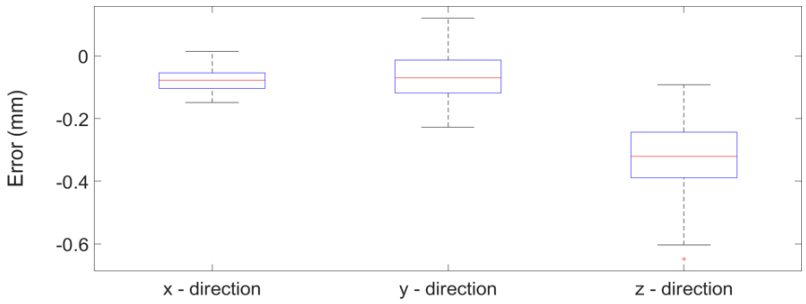

Figure C.3: Influence of warming up of the optical tracker. Box-and-whisker plots show the shift in measured location of DRF between a cold and a warmed-up tracking system. Measurements were obtained by using the milling machine.

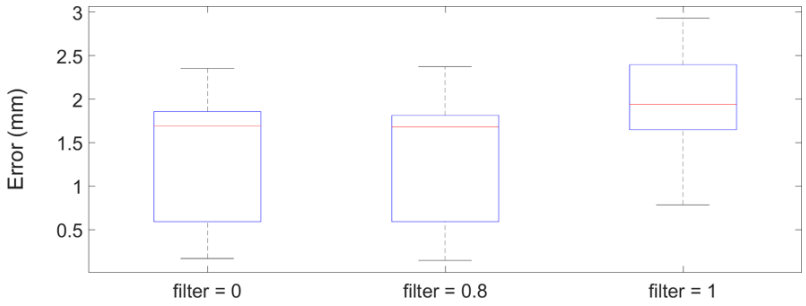

Figure C.4: Influence of filter settings on tracking performance. Box-and-whisker plots show error measured with different filter settings are shown. Errors are defined as the Euclidean distance calculated by comparing the measured coordinates with the references coordinates of the milling machine. Measurements with a filter of 0 or 0.8 were significantly lower than with a filter of 1 ($p < 0.001$).

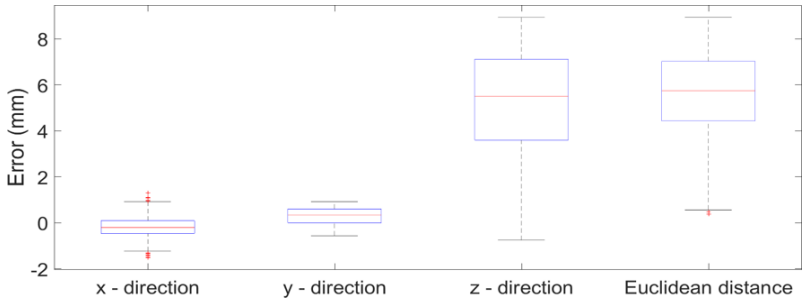

Figure C.5: Trueness of the optical tracker as compared to the reference coordinates of the milling machine. Deviations from the reference coordinates are visualized in box-and-whisker plots. Note the large error in the z-direction.

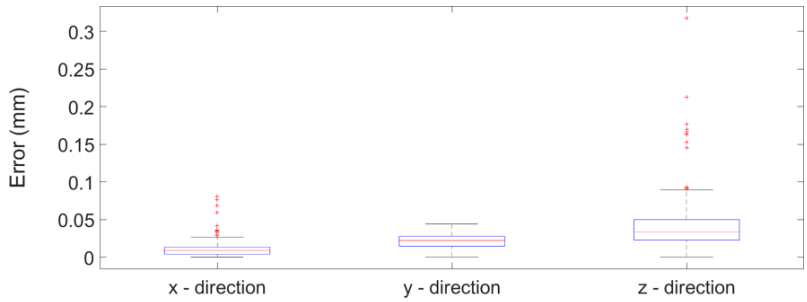

Figure C.6: Precision of the optical tracker. Error is expressed as the absolute difference between two consecutive measurements of the tracker in the measurement volume of the milling machine

Box-and-whisker plots for Chapter 4

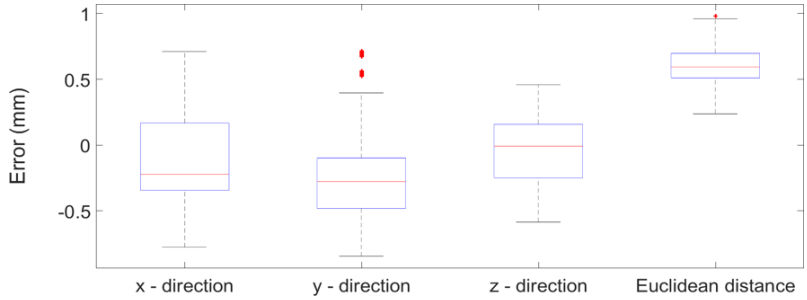

Figure C.7: Positional accuracy of OON **without** AR (tight-fit experiment). Box-and-whisker plots show the positional deviations between the tracked virtual cube and the planned virtual cube.

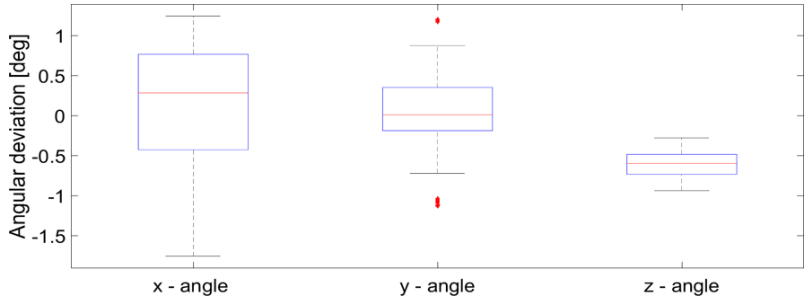

Figure C.8: Rotational accuracy of OON **without** AR (tight-fit experiment). Box-and-whisker plots show the angular deviation between the tracked virtual cube and the planned virtual cube.

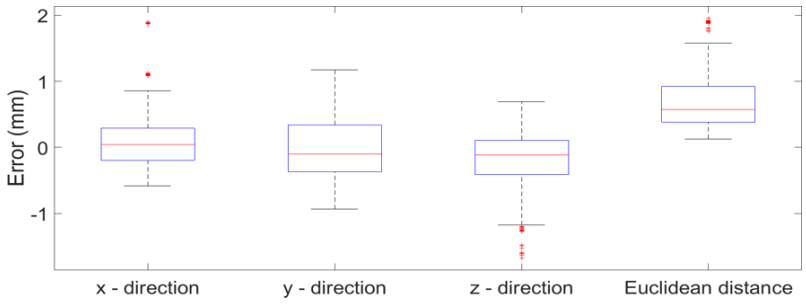

Figure C.9: Positional accuracy of object placement using OON **without** AR (loose-fit experiment). Box-and-whisker plots show positional deviations between virtual planned and virtual tracked cube after placement of the real cube at planned positions. The OON system was used as the only guidance.

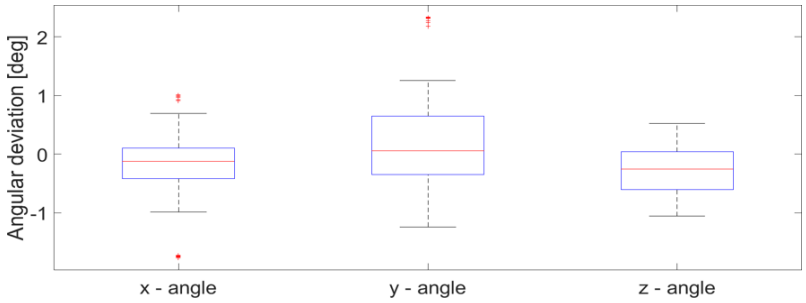

Figure C.10: Rotational accuracy of object placement using OON **without** AR (loose-fit experiment). Box-and-whisker plots show angular deviations between virtual planned and virtual tracked cube after placement of the real cube at planned positions. The OON system was used as the only guidance.

Box-and-whisker plots for Chapter 5

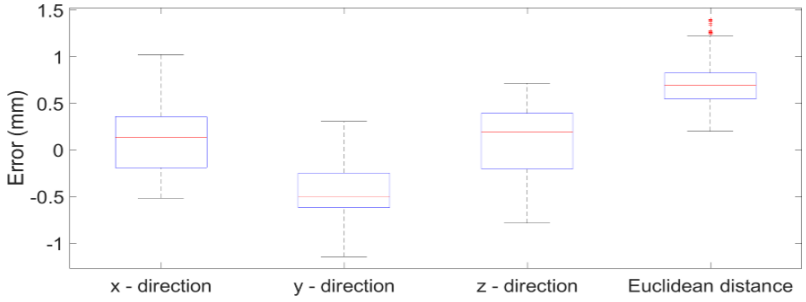

Figure C.11: Positional accuracy of OON **with** AR (tight-fit experiment). Box-and-whisker plots show the positional deviations between the tracked virtual cube and the planned virtual cube.

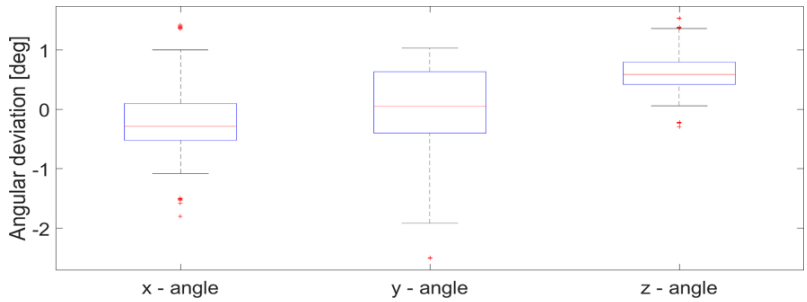

Figure C.12: Rotational accuracy of OON **with** AR (tight-fit experiment). Box-and-whisker plots show the angular deviation between the tracked virtual cube and the planned virtual cube.

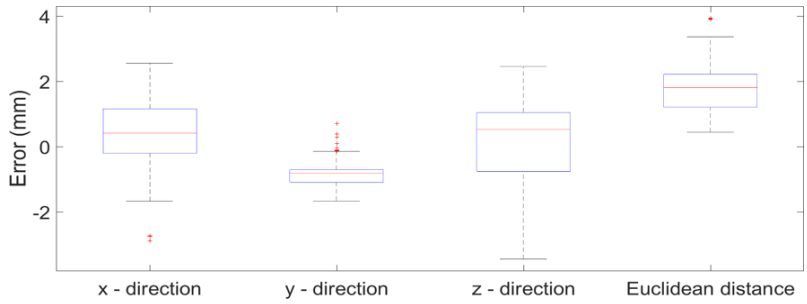

Figure C.13: Positional accuracy of object placement using OON **with** AR (loose-fit experiment). Box-and-whisker plots show positional deviations between virtual planned and virtual tracked cube after placement of the real cube at planned positions. Holograms of the cube at planned positions were used as guidance.

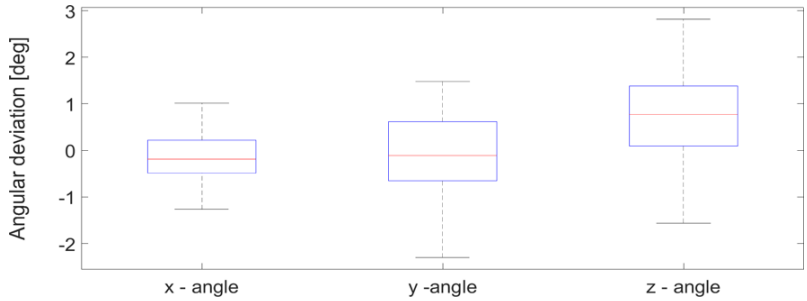

Figure C.14: Rotational accuracy of object placement using OON **with** AR (loose-fit experiment). Box-and-whisker plots show angular deviations between virtual planned and virtual tracked cube after placement of the real cube at planned positions. Holograms of the cube at planned positions were used as guidance.